Charge degrees of freedom on frustrated lattices

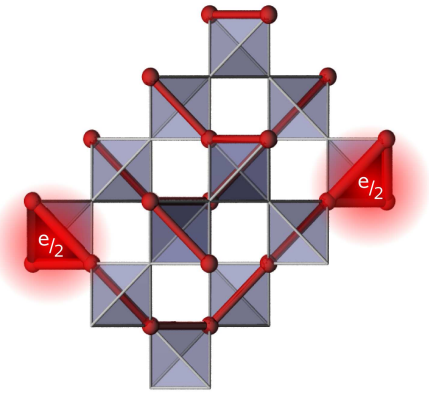

Dissertation zur Erlangung des akademischen Grades

Doctor rerum naturalium (Dr. rer. nat.)

vorgelegt der

Fakultät für Mathematik und Naturwissenschaften

der Technischen Universität Ilmenau

von Dipl. Phys. Frank Pollmann

1. Gutachter: Prof. Dr. Erich Runge (Technische Universität Ilmenau)
2. Gutachter: Prof. Dr. Peter. Fulde (Max–Planck–Institut für Physik komplexer Systeme)
3. Gutachter: Dr. Joseph Betouras (University of St. Andrews)

Tag der Einreichung:	11. August 2006
Tag der wissenschaftlichen Aussprache:	23. Oktober 2006

urn:nbn:de:gbv:ilm1-2006000140

Charge degrees of freedom on frustrated lattices

(Ladungsfreiheitsgrade auf frustrierten Gittern)

Zusammenfassung

Elektronische Korrelationen spielen in der Physik der kondensierten Materie eine wichtige Rolle, sie führen zu Phänomenen wie Magnetismus oder dem Mott–Hubbard Metall–Isolator–Übergang. In dieser Arbeit wird eine neuartige Klasse von Modellen stark korrelierter Elektronen betrachtet [Fuld 02]. Diese ermöglicht aufgrund des Wechselspiels zwischen starken Korrelationen und geometrischer Frustration das Auftreten fraktional geladener Teilchen in zwei Dimensionen (2D) und drei Dimensionen (3D). Geometrisch frustrierte Systeme sind durch eine hohe Dichte niedrig liegender Anregungen gekennzeichnet welche zu einer großen Suszeptibilität und somit zu interessanten physikalischen Effekten führen kann. Diese Arbeit enthält eine systematische Untersuchung von stark korrelierten spinlosen Fermionen auf bestimmten frustrierten Gittern. Insbesondere wird der interessante Grenzfall untersucht, in dem eine Wechselwirkung V zwischen benachbarten Plätzen groß gegenüber dem Hüpfmatrixelement $|t|$ ist. In diesem Fall können fraktionale Ladungen $\pm e/2$ realisiert werden. Im klassischen Grenzfall ($t = 0$) führt die geometrische Frustration zu einer makroskopischen Entartung und alle Grundzustände können, abhängig vom Füllfaktor, auf Schleifen– beziehungsweise Dimer– Konfigurationen auf Gittern abgebildet werden. Zum Beispiel können die klassischen Grundzustände des halb gefüllten Checkerboard–Gitters auf dicht gepackte Schleifen–Konfigurationen auf dem Quadrat–Gitter abgebildet werden. Die Korrelationsfunktionen zwischen zwei Defekten (zwei fraktionalen Ladungen) werden jeweils für Schleifen– und Dimer–Modelle auf unterschiedlichen Gittern analytisch und numerisch berechnet. Die Ergebnisse zeigen eine algebraische Abnahme mit der Entfernung auf 2D bipartiten Gittern und eine exponentielle auf dem 2D Dreiecks–Gitter, welches nicht bipartit ist. Die Korrelationen auf dem 3D bipartiten Diamant–Gitter fallen exponentiell mit dem inversen Abstand ab. Die makroskopische Entartung des Grundzustandes im klassischen Grenzfall wird bei endlichem t durch Quantenfluktuationen aufgehoben. Wir berechnen mit Hilfe der numerischen Diagonalisierung den quantenmechanischen Grundzustand sowie die niedrig liegenden Anregungen auf kleinen Checkerboard–Clustern. Für den Fall $|t| \ll V$ ist ein effektiver Hamilton–Operator in niedrigster Ordnung durch Ringaustausch um Hexagone ($\sim t^3/V^2$) gegeben [Rung 04]. Eine Eichtransformation ermöglicht es, das fermionische Vorzeichenproblem für den Grundzustand und die niedrig liegenden Anregungen zu eliminieren. Folglich kann das System bezüglich dieser Anregungen durch ein äquivalentes bosonisches System beschrieben werden. Der quantenmechanische Grundzustand zeigt eine langreichweitige Ordnung. Zwei statische fraktionale Ladungen erfahren eine gegenseitige anziehende Kraft, welche unabhängig vom Abstand ist. Diese resultiert aus einer Reduktion der Quantenfluktuationen und der Polarisation des Vakuums entlang einer Linie, welche die beiden fraktionalen Ladungen miteinander verbindet. Die berechneten

Spektralfunktionen zeigen im niedrig energetischen Bereich eine breite Struktur, welche durch die Dynamik der fraktional geladenen Anregungen entsteht. In den Spektralfunktionen zeigen sich Signaturen von Landau'schen Quasiteilchen mit großer räumlicher Ausdehnung (gebundene Paare von zwei fraktional geladenen Teilchen). Berechnungen der optischen Leitfähigkeit zeigen, wie fraktionale Ladungen zur elektrischen Leitfähigkeit beitragen. Durch eine geeignete Erweiterung unseres Modells kann man erreichen, dass es für einen Punkt im Parameterraum exakt lösbar wird. Dieser Punkt hat große Ähnlichkeit mit dem Rokhsar–Kivelson Punkt des Quanten–Dimer Modells [Rokh 88]. An diesem Punkt sind die fraktionalen Ladungen ungebunden. Für ein tieferes Verständins des betrachteten Modells auf dem Checkerboard–Gitter führen wir eine Abbildung auf eine $U(1)$ Gitter–Eichtheorie ein. Diese stellt einen Bezug zwischen fraktionalen Ladungen auf frustrierten Gittern und der kompakten Quantenelektrodynamik in 2+1 Dimensionen her. Des weiteren können wir mit Hilfe einer Dualitätstransformation unser Modell auf das Höhenmodell abbilden. Für eine erste Untersuchung eines 3D Systems mit fraktionalen Ladungen leiten wir einen effektiven Hamilton–Operator für das halb gefüllte Pyrochlor–Gitter her. Mit Hilfe von numerischen Diagonalisierungen berechnen wir den Grundzustand von kleinen Pyrochlor–Gittern. Qualitative Unterschiede und Ähnlichkeiten zum Grundzustand des oben beschriebenen Checkerboard–Gitters werden diskutiert.

Charge degrees of freedom on frustrated lattices

Abstract

Electronic correlations play an important role in condensed matter physics, resulting in phenomena such as magnetism or Mott–Hubbard metal–insulator transitions. In this thesis, a novel class of models of strongly correlated electrons is considered. It exhibits fractionally charged excitations in two dimensions (2D) and three dimensions (3D), arising from the interplay of strong correlations and the geometrical frustration of the underlying lattice [Fuld 02]. Geometrically frustrated systems are generally characterized by a high density of low–lying excitations which leads to large susceptibilities and thus to interesting physical effects. The thesis comprises a systematic study of strongly correlated spinless fermions on certain geometrically frustrated lattices. Particular emphasis is placed on the case where a nearest–neighbor repulsion V is large compared with inter–site hopping $|t|$. In that case, the model supports fractional charges $\pm e/2$. In the classical limit, $t = 0$, frustration leads to a macroscopic ground–state degeneracy and all ground states can be mapped to fully–packed dimer or loop coverings of lattices, depending on the filling factor. For example, the classical ground states of a half–filled checkerboard lattice are mapped on fully–packed loop coverings on a square lattice. Defect–defect correlation functions for different lattices and coverings are studied analytically and numerically. The results show correlations which decay algebraically with distance on 2D bipartite lattices and exponentially on 2D non–bipartite lattices. The correlations on a 3D bipartite diamond lattice fall off exponentially with the inverse distance. The classical macroscopic ground–state degeneracy is lifted by quantum fluctuations. We calculate the quantum mechanical ground states as well as low–lying excitations of finite checkerboard lattices by means of numerical diagonalization. For the limit $|t| \ll V$, an effective Hamiltonian is given to lowest non–vanishing order by ring exchange $\sim t^3/V^2$ [Rung 04]. A gauge transformation is used to remove the fermionic sign problem and the low–energy excitations can therefore equivalently be described by hard–core bosons. The quantum–mechanical ground state is degenerate and shows long–range order. Static fractional charges are linearly confined. The confinement results from a reduction of vacuum fluctuations and a polarization of the vacuum in the vicinity of a connecting string. The spectral functions show broad low–energy excitations. They are due to the dynamics of fractionally charged excitations. Signatures for quasiparticles with large spatial extent are found (bound pairs of two fractionally charged particles). Calculations of the optical conductivity show how fractional charges contribute to the electrical current density. Using a suitable extension of our model, we can fine–tune the model to a point in parameter space where it is exactly solvable. This point is similar to the so–called Rokhsar–Kivelson point [Rokh 88] and fractional charges are deconfined here. For a deeper understanding of the low–energy physics, a mapping to a confining $U(1)$ lattice gauge theory is presented. This mapping relates the problem of fractional charges to the compact quantum electrodynamics in $2+1$ dimensions. Furthermore, a duality transformation of our model

yields a height model. As a step toward true 3D systems, an effective Hamiltonian for the half–filled pyrochlore lattice in the limit $|t| \ll V$ is derived and studied numerically. We calculate the ground state of small pyrochlore clusters by means of numerical diagonalization. Qualitative differences and similarities to the ground state of a checkerboard lattice are discussed.

Contents

Chapter 1

Introduction

Quantization of charge is a very basic feature in the description of the physical world. Therefore, the discovery of fractionally charged excitations came as a surprise to physicists. An early investigation by Su, Schrieffer, and Heeger [Su 79] dates back to 1979 and deals with the chain molecule trans–polyacetylene $(\mathrm{CH})_\mathrm{n}$. Su et al. showed that a model of undoped polyacetylene supports excitations with spin–charge separation, but no excitations with fractional charge yet. This changes when the model is considered at different electron densities (corresponding to extremely high doping). It turns out that at certain doping concentrations of either particles or holes there are not only excitations with charge and spin separated, but their charge is a fraction ν of the electronic charge e only [Su 81]. In the simplest case $\nu = \pm 1/3$ and $\nu = \pm 2/3$. It should be mentioned that this phenomenon does not require direct interactions between electrons. However, it involves indirect interactions via lattice degrees of freedom though, since a double $\mathrm{C} = \mathrm{C}$ bond has a different length than a single $\mathrm{C} - \mathrm{C}$ bond. Doped trans–polyacetylene serves as an example of a one–dimensional system with fractional charges.

Fractional charges are also found in 2D in the much celebrated fractional quantum Hall effect (FQHE). It was Laughlin [Laug 83] who introduced this concept here. He explained with it the behavior of electrons in high–quality $\mathrm{GaAs}/\mathrm{AlGaAs}$ heterostructures in an applied magnetic field B normal to the planes. When the field deviates slightly from $B = nhc/e\nu$, where n is the density of the electrons and ν is a rational fraction with odd denominator, excitations with charge $\pm\nu e$ occur. The excitations with fractional charge νe are based on a new type of correlated ground state called the Laughlin state. It has also been demonstrated that the excitations fulfill fractional statistics, i.e., when two of them are exchanged, the phase changes by $e^{i\nu\pi}$. In distinction to the previously considered trans–polyacetylene, direct electron–electron interactions are crucial here. Note that correlations become strong in an applied magnetic field since the kinetic energy of the electrons is quenched.

The question was left open whether or not fractionally charged excitations exist in 2D or 3D systems without a magnetic field. In [Fuld 02] it was suggested that in a pyrochlore lattice, a prototype of a 3D structure with geometrical frustration, excitations with charge $\pm e/2$ do exist. The pyrochlore structure is found, for example, in the transition metal

compound LiV_2O_4. In that compound, vanadium has a half integer valency and electronic correlations are strong as indicated by a large γ coefficient in the low temperature specific heat $C = \gamma T$ [Kond 97]. Although LiV_2O_4 has motivated work of the kind presented here, we do not claim that the theory of fractional charges applies to that specific material [Fuld 01]. Generally, prerequisites for fractional charges in the considered model are strong short–range correlations and certain band fillings.

In order to study frustrated systems with charge degrees of freedom, several 2D and 3D lattice models are considered. In the following, we mainly focus on a checkerboard lattice, which can be thought of as a projection of the pyrochlore lattice onto a plane. Although there are differences in the physics of the two systems due to the different dimensions, one can learn much from the simpler two–dimensional system. Numerous studies of spin systems on the pyrochlore and checkerboard lattice were done and reported in [Misg 03, Diep 05, Herm 04, Lauc 04, Shan 04]. We want to study the charge degrees of freedom on these lattices systematically and consider a model of strongly correlated spinless fermions. As a first step, quantum fluctuations are neglected, i.e., the classical limit is considered. We calculate correlations on large lattices consisting of several thousand sites and conclude about the existence of deconfined fractionally charged particles at high temperatures. Quantum mechanical calculations provide the ground state and excited states of the considered model at zero temperature. Numerical diagonalization of an effective Hamiltonian allows to make statements about confinement of fractionally charged particles. Furthermore, certain similarities to confinement of quarks in quantum chromodynamics can be seen. The advantage of studying the model of fractional charges on frustrated lattices is that it enables us to describe in detail the microscopic origin of the constant confining force. By using an additional parameter, we fine–tune the system to a special point at which fractional charges are deconfined—the so–called Rokhsar–Kivelson point [Rokh 88]. This particular point is studied in detail to check whether a deconfined phase may form in its vicinity.

The question has not been posed yet how one would be able to detect experimentally experimentally signatures of our exotic excitations with fractional charges. Here, spectral functions and optical conductivity of fully spin polarized or, equivalently, spinless fermions on a checkerboard lattice might shed some light on that topic. It is demonstrated that the fractionalization of charge leads to characteristic features which are absent when fractionalization is forbidden. Perhaps the investigation may sharpen the attention of experimentalists when doing photoemission experiments on, e.g., systems with spinel structure at certain valencies, i.e., when the filling factors are right. Also experimental progress in the generation of optical lattices should be noted. Recently it has been reported that 3D optical lattices can be generated and filled with either bosons or fermions to simulate relevant Hamiltonians, e.g., in [Hofs 02] and citations therein. For a deeper understanding of the low–energy excitation in our model, we present a mapping into a lattice gauge theory [Kogu 79, Frad 91]. It relates the problem at hand to the well studied compact electrodynamics in 2+1 dimensions [Poly 77] and the height model [Henl 97, Henl 04]. Furthermore, as a first step toward quantum mechanical 3D systems, we calculate the ground state of small pyrochlore clusters and compare it with the results obtained for checkerboard lattices.

The thesis is organized as follows. We begin with a brief review of the two earlier mentioned models which exhibit fractionally charged excitations, namely the polyacetylene chain molecule and the fractional quantum Hall effect. Then we derive the concept of fractional charge in a model of spinless fermions on the half–filled checkerboard lattice. In Chapter 3, we generalize the model to other filling factors and consider different frustrated lattice structures. We present a mapping of the original lattice models in the strongly correlated limit to fully–packed hard–core dimer and loop models. For the latter, we calculate analytically and numerically defect–defect correlation functions [Poll 06b]. Chapter 4 shows results of a quantum mechanical investigation of spinless fermions on a checkerboard lattice with strong nearest–neighbor repulsion. An effective Hamiltonian for the limit $|t| \ll V$ is derived which includes the lowest non–vanishing order of ring exchange. It is shown that the effective fermionic system can equivalently be described by hard–core bosons [Poll 06d]. The quantum mechanical ground state as well as low–lying excitations of small checkerboard lattices are studied numerically by means of exact diagonalization. From the quantum mechanical ground state, we conclude about long–range order and confinement of fractionally charged particles [Poll 06e]. We extend the model by an additional parameter to allow for fine–tuning of the system to a deconfined point and exclude the possibility that this point extends to a phase. The spectral function and optical conductivity of our model are calculated in order to make conclusions about dynamical properties of the fractionally charged excitations [Poll 06a]. In Chapter 5, we map the model to a $U(1)$ lattice gauge theory. Within the gauge–theoretic description of the effective model, we discuss similarities to the quantum electrodynamics in $2+1$ dimensions and the height model [Poll 06c]. First numerical results for the quantum mechanical ground state of spinless fermions on the 3D pyrochlore lattice are given in Chapter 6. Similarities and differences to the 2D checkerboard lattice are discussed. The last chapter summarizes the results and gives an outlook.

Chapter 2

Fractionalization in 1D, 2D, and 3D systems

We begin with a brief review of some historical ideas of fractionalization in condensed matter physics. Particular attention is paid to fractionalization of charge. Two prominent examples are solitons in polyacetylene [Su 79] and the fractional quantum Hall effect [Tsui 82, Laug 83]. Detailed reviews can be found in, e.g., [Girv 99, Wilc 02, Bone 02, Kive 01, Laug 99]. Along the discussion of these examples of fractionalization, we find certain similarities and differences to the class of models considered in this thesis. We will then discuss the concept of fractional charges on frustrated lattices in detail. In particular, we will show how fractionally charged excitations arise in a model of strongly correlated spinless fermions on a checkerboard lattice.

2.1 Brief history of fractionalization

A convincing and historically important model that exhibits spin–charge separation is given in a paper by Su, Schrieffer, and Heeger [Su 79] on excitations in a polyacetylene

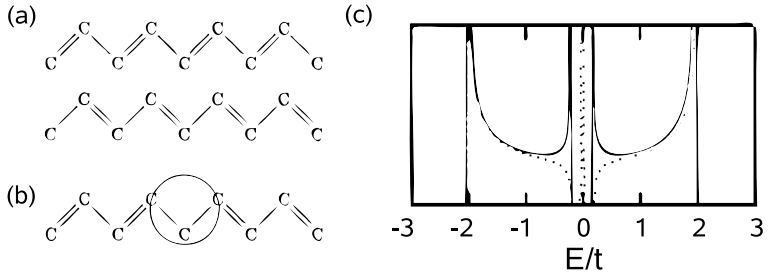

Figure 2.1: (a) Two alternative ground states A and B of polyacetylene with alternating single– and double–bonds. (b) Domain wall between A and B phase. (c) Formation of a domain wall results in the development of a mid–gap state in the one–electron density of states and a net–electric charge of $+e$ if the state is empty [Laug 99].

chain molecule. A simple counting argument gives rise to fractionally charged excitations in heavily doped systems [Su 81]. The ground state of polyacetylene is idealized as a chain molecule with alternating single– and double–bonds as shown in Figure 2.1 (a). The ground state is two–fold degenerate and can schematically be represented by

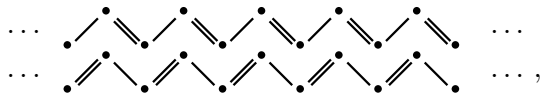

where we term the two degenerate dimerization patterns A and B phases. Removing one bond from the ground state of, e.g., the A phase yields

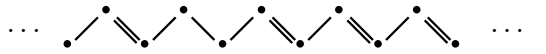

and leads to two defects in the alternating bond order. Now, we can shift the bonds between neighboring links and separate the two defects from each other:

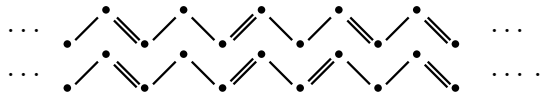

We find the bonds between the two defects oriented as in phase B. Each of the elementary defects can be seen as a domain wall between phases A and B as shown in Figure 2.1 (b). If the removed bond would be an electron with charge e and spin $1/2$, each of the domain walls would have a charge $e/2$ and spin $1/4$. However, the bonds represent pairs of electrons and we do not get fractional charge. Instead we find that a domain wall acquires charge e with spin 0. Charge and spin separate and so–called mid–gap states are formed, see Figure 2.1 (c).

A generalization of this model is to consider the case of a one–third filled band [Su 81]. In this case, we find three degenerate ground states instead of two. One of these is for example

Here, removing one bond leads to

We find three defects which can be separated by rearranging the bonds to

Since the removed bond leads to three elementary defects, true fractions of the elementary electric charges are unavoidable. The domain walls carry now charges of $\pm e/3$ and $\pm 2e/3$. As we will see later on, the argument of fractionalization of an added "defect" can be generalized to the fractionalization of spinless fermions on frustrated lattices. A further insight into the physics of polyacetylene, beyond the counting arguments by Schrieffer et al., is provided by the field–theory description by Jackiw and Rebbi [Jack 75].

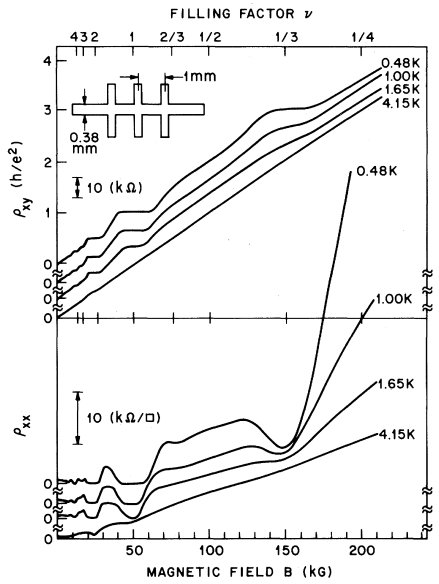

Figure 2.2: The fractional quantum Hall effect. The Hall resistance (upper curve) in a high mobility heterostructure shows plateaus at magnetic fields B that correspond to filling factors ν. At the same filling factors, the magneto resistivity (lower curve) shows minima [Tsui 82].

The second prominent example of fractionalization of charge is the fractional quantum Hall effect. It was discovered by Tsui and Stormer in 1982 [Tsui 82], who received the Nobel prize in 1998 together with Laughlin for their work. Using high–mobility $\mathrm{GaAs/AlGaAs}$ heterostructures, they observed quantization of Hall conductance at filling factors $\nu = 1/3$ and $\nu = 2/3$ at very low temperatures (Figure 2.2). Later, richer structures with other fractional filling factors ν have been found. Laughlin [Laug 83] explained the behavior of electrons by a correlated ground–state wavefunction which has fractionally charged excitations. In distinction to the previously considered trans–polyacetylene, direct electron–electron interactions are crucial here. In an applied magnetic field, correlations become strong since the kinetic energy of the electrons is reduced. The famous ground–state wavefunction for N electrons at positions $z = x + iy$ reads

$$\psi_m(z_1, \ldots, z_N) = \prod_{j<k} (z_j - z_k)^m \exp\left(-\frac{1}{4l^2}\sum_j^N |z_j|^2\right). \tag{2.1}$$

Here, $\nu = 1/m$ with m being an odd integer number and the magnetic length is $l^2 = \frac{1}{eB}$. The first factor includes the electronic correlations, i.e., each electron repels all other electrons. The second factor enforces an approximately constant density. The fractional quantum Hall liquid has a finite gap (i.e., it is incompressible) and the quantized Hall conductance is given by

$$\sigma_{xy} = \frac{e^2}{h}\nu, \tag{2.2}$$

with the Planck constant h and the filling fraction ν. Furthermore, there is no dissipation and $\sigma_{xx} = \sigma_{yy} = \rho_{xx} = \rho_{yy} = 0$.

To see that the Laughlin wavefunction (2.1) carries fractional charges, it is useful to look at the connection between the fractional charge and the quantization of Hall conductance. Therefore, we pierce the ground–state in a "Gedanken experiment" with an infinitesimal thin solenoid carrying a magnetic flux Φ along the $\hat{z}$–axis (perpendicular to the plane). The finite gap ensures that we can adiabatically increase the flux Φ. Once the flux reaches a magnetic flux quantum of $\Phi_0 = hc/e$, we can use a gauge transformation to effectively remove it from the Hamiltonian and the resulting state is an eigenstate. This new eigenstate has a new charge which has accumulated in the vicinity of the solenoid. From Faraday's law, we know that

$$\oint_\Gamma d\mathbf{r} \cdot \mathbf{E} = -\frac{1}{c}\frac{\partial \Phi}{\partial t}, \tag{2.3}$$

where Γ is a closed path around the flux tube. The current density induced by an electric field $\mathbf{E}$ in the probe with $\rho_H = 1/\sigma_H$ obeys

$$\mathbf{E} = \rho_{xy}\mathbf{J} \times \hat{z}. \tag{2.4}$$

We can combine (2.3) and (2.4) to

$$\rho_{xy} \oint_\Gamma \mathbf{J} \cdot (\hat{z} \times d\mathbf{r}) = -\frac{1}{c}\frac{\partial \Phi}{\partial t}.$$

The left hand side represents the total current flowing into the region that is enclosed by the path Γ and we can write

$$\rho_{xy}\frac{dQ}{dt} = -\frac{1}{c}\frac{d\Phi}{dt},$$

where Q is the charge enclosed by Γ. After one flux quantum Φ_0 has been added, the final charge is

$$Q = \frac{1}{c}\sigma_{xy}\Phi_0 = \frac{h}{e}\sigma_{xy},$$

where we exploited the fact that $\sigma_{xy} = \rho_{xy}^{-1}$ if $\rho_{xx}\rho_{yy} = 0$. Using expression (2.2) for the conductivity, we find for a given filling factor ν a fractionalized charge of

$$Q = \nu e.$$

The sign of the charge is reversed by reversing the sign of the added flux. From the "Gedanken experiment", we can see the relation between magnetic flux and fractional charge in the fractional quantum Hall effect.

Note that the above argument depends on the dimensionality of the system: Piercing the probe with a flux leads only to point–like excitations when the probe has two spatial dimensions.

The fractionally charged excitations have been observed directly by different techniques, for example by shot noise measurements [Picc 97] and ultra sensitive electrometers made from a quantum dot [Gold 95]. These techniques are not restricted to the fractional quantum Hall effect and might be used to detect fractional charges in experimental realizations of the model considered in this thesis.

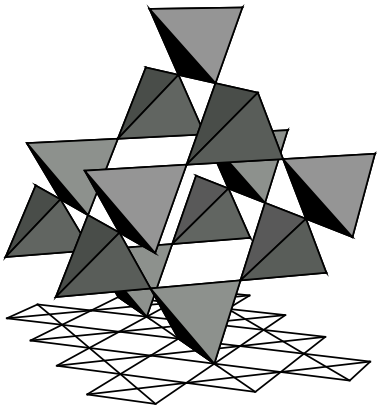

Figure 2.3: 3D pyrochlore lattice with a 2D projection on a checkerboard lattice [Moes 04].

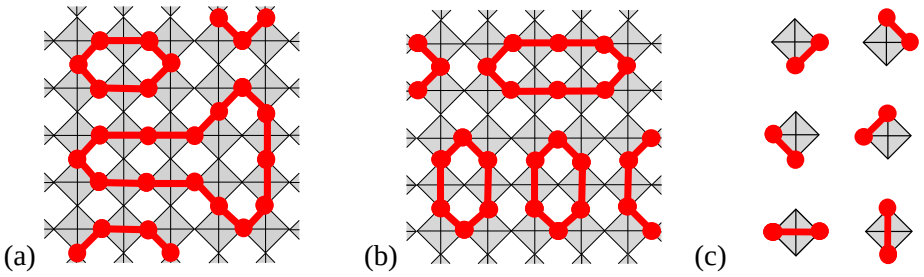

Figure 2.4: Panels (a) and (b) show examples of allowed configurations on a checkerboard lattice at half filling. The occupied sites are connected by red lines. Panel (c) shows the six different allowed configurations of a single crisscrossed square.

2.2 Fractional charges on frustrated lattices

The aforementioned examples of fractional charges are restricted to low–dimensional systems. It was not clear whether or not fractionally charged excitations exist in 2D or 3D systems without strong magnetic fields. Recently, the existence of excitations with charge $\pm e/2$ has been predicted in a geometrically frustrated pyrochlore lattice. In order to illustrate the concept of fractional charges on frustrated lattices, a checkerboard lattice is considered here. The checkerboard lattice can be thought of as a projection of the pyrochlore lattice on a plane, see Figure 2.3. One can learn much from the simpler 2D system. However, as we will see in the next chapters, there are certain differences in the physics of the two systems due to the different dimensions. Also spin systems on the pyrochlore and checkerboard lattice have recently received a wide interest [Misg 03, Herm 04, Lauc 04, Shan 04].

In the following, we adopt the ideas of [Fuld 02] and consider a model Hamiltonian of spinless fermions

$$H = -t \sum_{\langle i,j \rangle} \left(c_i^\dagger c_j + \text{H.c.} \right) + V \sum_{\langle i,j \rangle} n_i n_j \tag{2.5}$$

on a crisscrossed checkerboard lattice. The operators $c_i(c_i^\dagger)$ annihilate (create) fermions on sites i. The density operators are $n_i = c_i^\dagger c_i$. We assume that half of the sites are occupied by fermions, i.e., $\sum_i n_i = \frac{N}{2}$ for a system with N sites. Our main interest is the regime $|t|/V \ll 1$.

For a moment, let us set the hopping integral t to zero. The ground–state manifold is then macroscopically degenerate: Every configuration that satisfies the so–called tetrahedron rule of having exactly two particles on each tetrahedron (crisscrossed square) is a ground state [Ande 56]. In other words, the system has a finite $T = 0$ entropy (for possible technical applications, see [Zhit 03]). Figures 2.4 (a) and (b) show examples of such classical ground–state configurations. We will refer to configurations satisfying the tetrahedron rule as "allowed configurations". One can visualize the origin of a macroscopic degeneracy as follows: Take the set of six allowed crisscrossed squares which are shown in Figure 2.4 (c), and construct row by row an allowed configuration of a given size. Each time when adding a crisscrossed square, we have to choose between one and three different possibilities, depending on the neighboring crisscrossed squares. Since there is a choice between different configurations to make, we have an exponential number of different allowed configurations that can be constructed from the set of allowed configurations of single crisscrossed squares. The exact value of the degeneracy can be obtained from a mapping to the so–called six–vertex model [Baxt 82].[1] From this mapping, we know that (i) the ground–state manifold of the model grows as $W \sim (4/3)^{3N/4}$ where N is the number of lattice sites [Lieb 67] and (ii) all correlation functions decay algebraically [Baxt 82].

The classical ($t = 0$) ground states have the important property of being incompressible in the sense that no fermion can hop to another empty site without creating defects. In other words, we have to violate the tetrahedron rule if we want to transform one allowed configuration into another.

Fractional charges. Placing one additional particle with charge e onto an empty site leads to a violation of the tetrahedron rule on two adjacent crisscrossed squares (see Figure 2.5 (a)). The energy is increased by $4V$ since the added particle has four nearest neighbors. There is no way to remove the violations of the tetrahedron rule geometrically by simply moving the electrons, i.e., the energy increase of $4V$ is conserved. However, fermions on a crisscrossed square with three particles can hop to another neighboring crisscrossed square without creating additional violations of the tetrahedron rule, i.e., without increase of repulsive energy (see panels (b) and (c) in Figure. 2.5). By these hopping processes, two local defects (violating the tetrahedron rule) can separate and the

[1] For this mapping, we use the fact that the crisscrossed squares form a bipartite square lattice. First, we divide the crisscrossed squares into two sublattices A and B. Then we draw an arrow from the center of A to B sublattice crisscrossed square where they share an empty side, and from B to A where they share an occupied site.

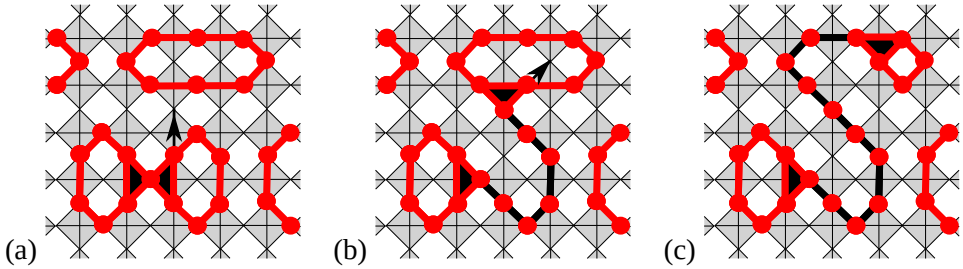

Figure 2.5: Adding one fermion to the half–filled checkerboard lattice leads to two defects on adjacent crisscrossed squares. Two defects with charge $e/2$ can separate without creating additional defects and are connected by a string consisting of an odd number of fermions, shown by a black line.

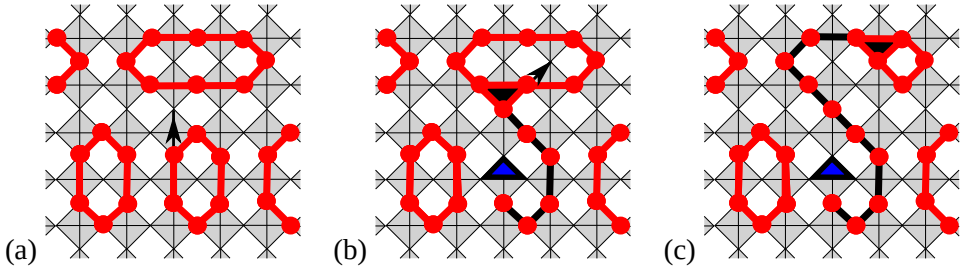

Figure 2.6: Hopping of a fermion to a neighboring site in an allowed configuration generates a fluctuation—a fractional charged particle (fcp) and fractional charged hole (fch) are generated. The two defect with charge $\pm e/2$ can separate without creating additional defects and are connected by a string consisting of an even number of fermions, shown by a black line.

added fermion with charge e breaks into two pieces. They carry a fractional charge of $e/2$ each. The separation gains additional kinetic energy of order t. Energy and momentum must be conserved by the decay processes. If we associate momentum $\mathbf{k}$ and energy $E(\mathbf{k})$ with the added fermion which we inserted, they must now be shared between the free fractionally charged particles (fcp's) into which it has decayed

$$E\left(\mathbf{k}\right) = 4V + \epsilon\left(\mathbf{k}_1\right) + \epsilon\left(\mathbf{k}_2\right),$$

where $\epsilon\left(\mathbf{k}\right)$ is the dispersion of a fcp and $\mathbf{k} = \mathbf{k}_1 + \mathbf{k}_2$.

The two defects are always connected by a string of occupied sites consisting of an *odd* number of sites. Thus, the fractional charges can be alternatively interpreted as the ends of a string–like excitation.

Quantum Fluctuations. If we relax the constraint of having two fermions on each crisscrossed square and consider a very small but finite ratio t/V, quantum fluctuations come into play. The quantum fluctuations lead also to fractional charges, but do not change the net charge of the systems. Starting from an allowed configuration, the hopping

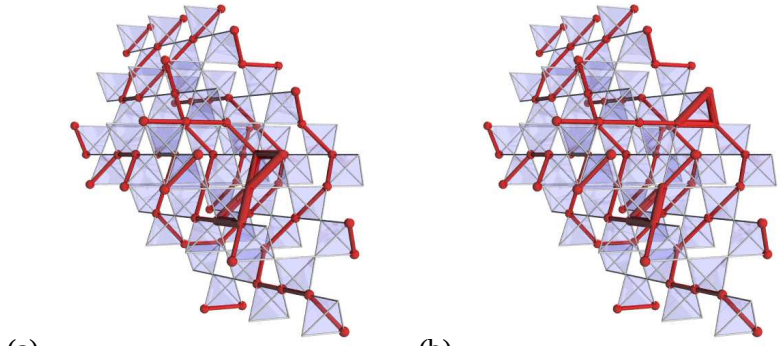

(a) (b)

Figure 2.7: Adding one fermion to the half–filled pyrochlore lattice leads to two defects on adjacent tetrahedra. The two defects with charge $e/2$ can separate without creating additional defects and are connected by a string consisting of an odd number of fermions.

of a fermion to a neighboring site increases the energy by V. One crisscrossed square contains three fermions while the other has only one fermion, as shown in Figure 2.6. Two mobile fractional charges with opposite charges $+e/2$ and $-e/2$ arise. The fractionally charged particle (fcp) and fractionally charged hole (fch) are connected by a string of an *even* number of fermions. The energy associated with a vacuum fluctuation consisting of a free fcp and a free fch is

$$\Delta E_{\text{vac}} = V + \epsilon\left(\mathbf{k}\right) + \bar{\epsilon}\left(-\mathbf{k}\right),$$

where $\epsilon\left(\mathbf{k}\right)$ denotes the kinetic energy of a fcp and $\bar{\epsilon}\left(-\mathbf{k}\right)$ the kinetic energy of a fch. The potential energy is lowered by the kinetic energy of the two defects leading to a reduction of the macroscopic degeneracy. Processes in lowest non–vanishing order in $\mathcal{O}(t/V)$ connect different allowed configurations and reduce the macroscopic degeneracy. Details of possible low–order processes and a perturbative treatment of quantum fluctuations will be given in Chapter 4.

Fractional charges in 3D All above mentioned arguments for the existence of fcp's on a 2D checkerboard lattice can be directly transferred to a 3D pyrochlore lattice at half filling (see Figure 2.7). For example, fcp's correspond to tetrahedra with three fermions and fch's to tetrahedra with only one fermion. To our knowledge, this model gives the first realization of fcp's in 3D systems. There exist, however, certain differences in the behavior of fractional charges in 2D and 3D which will be discussed in the following chapters.

Chapter 3

Classical correlations

To start a systematic study of models of the kind introduced in the preceeding chapter, we first exclude quantum fluctuations and consider the corresponding classical system. In other words, we neglect the quantum–mechanical kinetic energy and consider statistical ensembles of allowed configurations. In the long–run, one wants to understand the behavior of mobile, fractionally charged, excitations resulting from weak particle or hole doping of such systems.

The motion of spinless fermions (or hard–core bosons) with nearest–neighbor repulsion V on a lattice is mapped to dimer/loop models for some given lattice geometries and filling factors. The addition of a fermion (or boson) leads to a new dimer. The ground states of the considered systems fulfill a local constraint of having a certain number of particles on each unit cell or, equivalently, a certain number of dimers at each site. As a first step, we obtain classical defect–defect correlations for such dimer models. A defect here carries a fractional charge of $e/2$. From the correlation functions, we can directly conclude about confinement/deconfinement of fractional charges in the classical limit.

3.1 Frustrated lattice structures and dimer models

We are interested in lattices for which the ground state of the Hamiltonian (2.5) with repulsive nearest–neighbor interaction term V only has at certain fillings a macroscopic degeneracy, which increases exponentially with the system size. Furthermore, these ground states have the property that they are characterized by a local constraint. An example of such lattices is the aforementioned crisscrossed checkerboard lattice. At half filling, all classical ground states fulfill the local constraint of having exactly two particles on each crisscrossed square. Configurations fulfilling this local constraint can be reinterpreted as dimer coverings on the square lattice with two dimers touching every site. To see this, we observe that the centers of the crisscrossed squares form a square lattice, as shown in Figure 3.1 (a). Each nearest–neighbor square link passes through exactly one site of the checkerboard lattice. The dimer coverings are then constructed by drawing a dimer whenever the traversed site of the checkerboard lattice is occupied. Similarly, the pyrochlore lattice can be mapped on a dimer model on a diamond lattice and the kagomé

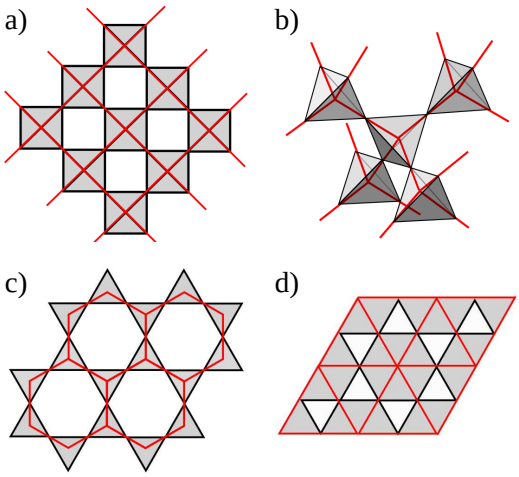

Figure 3.1: Mapping of lattices which show frustration (black) to lattices on which the dimer models are defined (red). (a) Checkerboard lattice with nearest–neighbor repulsion → square lattice, (b) pyrochlore lattice with nearest–neighbor repulsion → diamond lattice (c) kagomé lattice with nearest–neighbor repulsion → honeycomb lattice and (d) kagomé lattice with repulsion interaction on hexagons only → triangular lattice. The constraint of having a certain number of particles in each unit cell translates into the constraint of having a fixed number of dimers touching each site.

lattice on a dimer model on a honeycomb lattice, see Figure 3.1 (b) and (c). We also consider a slightly modified model of (2.5) on the kagomé lattice. Namely the kinetic–energy hopping term runs as usual over nearest–neighbors, but the repulsion term V is summed over all possible pairs of sites on a hexagon. In this case, we obtain a dimer model on a triangular lattice, see Figure 3.1 (d). Depending on the filling factor of the original lattice, we obtain different coverings in which each site is either touched by one (hard–core dimer covering) or by two dimer (loop covering). Adding one dimer leads to two defects on adjacent sites which can separate as shown in Figure 3.2. Obviously, on bipartite lattices, the two defects reside on different sublattices. These defects correspond to two fractionally charged particles (fcp's) as defined is Section 2.2.

Our study includes bipartite (square and honeycomb lattice) and non–bipartite 2D triangular lattice as well as a bipartite 3D diamond lattice, with two different filling factors (hard–core dimer and loop). Wherever possible, we obtain analytical results and compare them to numerical simulations. These classical correlations provide informations about correlations near the so–called Rokshar–Kivelson point (RK point) of the quantum Hamiltonian because at the RK point the quantum mechanical ground state is given by an equally weighted superposition of all configurations [Rokh 88] (see Section 4.1.2). Furthermore, in our case, one can expect classical correlations on the square lattice to hold even for the fermionic model since the low–energy excitations can be described equivalently by hard–core bosons or fermions (see Section 4.2.1).

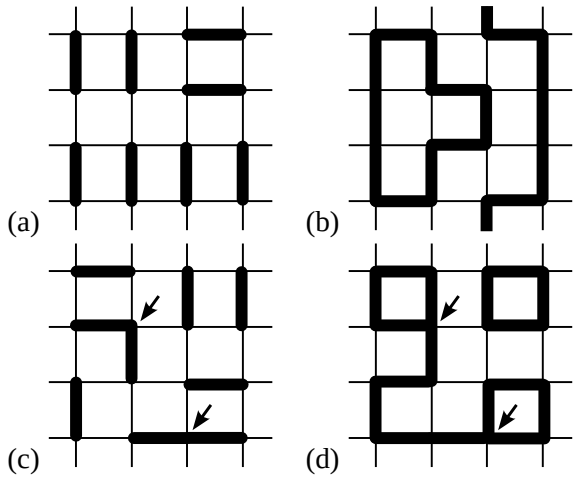

Figure 3.2: Hard–core dimer (a) and loop (b) covering of a square lattice. Panels (c) and (d) show two defects in the coverings at positions marked by arrows.

Historically, studies of monomer and dimer models started very early [Fowl 37]. At zero doping, the Pfaffian method introduced by Kasteleyn [Kast 61] allows to obtain classical correlations analytically. For the square lattice with hard–core dimer covering, the correlation for a pair of monomers has been obtained in [Fish 61, Hart 66].

Defect–defect correlations $C(\mathbf{0},\mathbf{r}) \sim \langle n_{\mathbf{0}} n_{\mathbf{r}} \rangle$, which give the probability to find two defects at a certain distance $\mathbf{r}$, allow us to conclude about confinement or deconfinement of fractional charges in the classical limit. The confinement results from the entropy term $S(\mathbf{r}) \sim \ln C(\mathbf{r})$ in the free energy $F(\mathbf{r}) = U_0 - TS(\mathbf{r})$. Recall, that all configurations have the same energy and thus $U = U_0$. A separation of two defects to an infinite distance leads to an energy increase

$$\Delta F(\infty) \quad \sim \quad -T[\ln C(\infty) - \ln C(0)]. \tag{3.1}$$

Consequently, $\Delta F(\infty)$ is at any finite temperature infinite if the defect–defect correlation function tends to zero (confinement), e.g., an algebraical decay leads to a logarithmic divergence of the free energy. On the other hand, if the correlations decay to a constant finite value, the increase of free energy remains finite (deconfinement).

3.2 Analytic calculation for the checkerboard lattice

As described above, the half–filled checkerboard lattice with nearest–neighbor repulsion can be mapped onto a loop model on the square lattice, meaning that each site is connected to exactly two dimers. This can then be interpreted as covering by fully packed loops (FPLs) with two colors assigned to occupied and unoccupied bonds. Using the machinery developed for loop coverings of this kind [Kond 96a, Kond 98], which is summarized in Appendix A, we can read off the appropriate exponent of the defect–defect correlation

function. The problem at hand corresponds to fugacities $n_b = 2\cos(\pi e_b) = 1$ and $n_g = 2\cos(\pi e_g) = 1$ since links of both colors are equally weighted. Thus, using (A.0.2) with $e_b = e_g = 1/3$, the exponent is simply

$$2x_{1,1} = \frac{1}{2\pi}\left(\frac{4\pi}{3} - \frac{2\pi}{3}\right) = \frac{1}{3}. \tag{3.2}$$

The result (3.2) that $C(\mathbf{0},\mathbf{r}) \sim 1/x^{1/3}$ will be verified numerically by Monte Carlo simulations in the next section.

The defect–defect correlations in the half–filled case are proportional to the restricted partition function

$$Z_{11}(\mathbf{0},\mathbf{r}) \sim |\mathbf{r}|^{-2x_{11}} \tag{3.3}$$

of the two–color fully packed loop model (see Appendix A). It counts the number of configurations with defects at $\mathbf{0}$ and $\mathbf{r}$ connected by one string of each color. One expects $C(\mathbf{0},\mathbf{r})$ to become isotropic at large distances and to decay algebraically as $Z(\mathbf{0},\mathbf{r}) \sim |\mathbf{r}|^{1/3}$.

3.3 Numerical simulations

Dimer models are numerically preferable to those particle model on the original lattices, because the constraints are included in a more natural way. Even though dimer models have been intensively investigated in the study of spin models [Diep 05], not much is known about defect–defect correlations, e.g., $C(\mathbf{0},\mathbf{r}) \sim \langle n_{\mathbf{0}} n_{\mathbf{r}}\rangle$. In the following, we measure the correlations along a coordinate axis [$\mathbf{r} = (x,0)$] and refer to it as $C(x)$.

The classical two–point correlation functions at zero temperature are determined as averages over all degenerate ground states. For the numerical implementation, an allowed configuration with fixed filling is generated, i.e., a ground state of the undoped system with no violation of any local constraint. Then we add a dimer onto an unoccupied random link. This leads to two defects on adjacent sites of the lattice, which subsequently propagate via local dimer moves through the system without creating any new defects. At each step, the defect–defect distance x is counted in a histogram $Z(x)$, which after normalization yields the correlation function $C(x) = Z(x)/Z_0$. The normalization is somewhat arbitrary, we choose it so that $C(1) = 1$. The algorithm is terminated when the standard deviation of the measured quantity falls below a certain threshold. Results of simulations with different initial configurations are compared for verification. For 2D lattices about $10^7 - 10^8$ samplings were necessary. For a 3D diamond lattice, it took about 10^{10} steps until convergence was reached. We also applied an alternative Monte Carlo algorithm with loop updates [Yana 78, Sylj 02], which is known to be ergodic and unbiased, but shows considerably slower convergence. The ergodicity follows directly from the fact that any difference between two allowed configurations can be represented in terms of closed loops with alternating occupied and empty links [Bark 98].

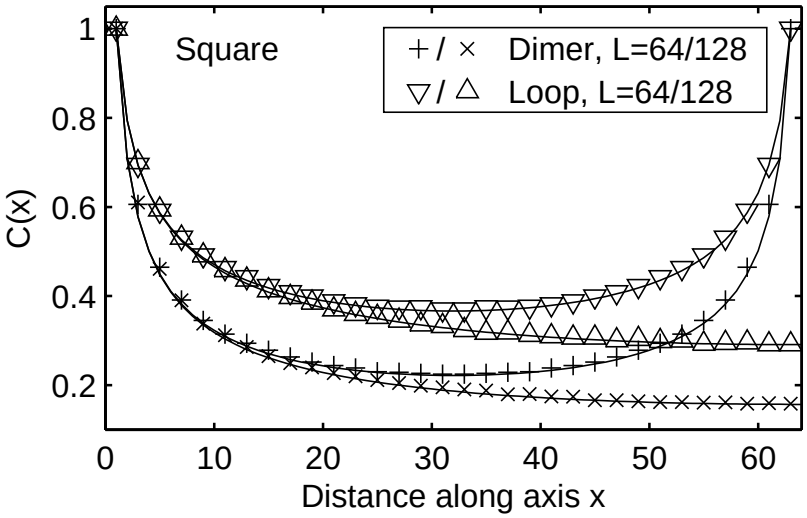

Figure 3.3: Classical defect–defect correlation functions on a square lattice with hard–core dimer and loop coverings along a coordinate axis. Results are shown for lattices with $L = 64$ and $L = 128$. The numerical data are well fitted by the exact asymptotic results. The periodic boundary conditions are taken into account by plotting the fit against a rescaled distance variable.

The algorithms have been applied to different lattice structures and filling factors (see Figure 3.1). To test the algorithm, we first reproduced the known monomer two–point correlations in the hard–core dimer model on the square and triangular lattice (see Figure 3.3 and Figure 3.6) as well as the dipolar correlations in the undoped system on a square lattice [Moes 04, Isak 04].

3.3.1 Square lattice

Figure 3.3 compares the numerical data and the analytical results. Note that for the numerical fit, a rescaled distance variable $x' = L\sin(\pi x/L)/\pi$ is used in order to account for periodic boundary conditions. We extracted the exponent from the numerical data by linear interpolation of $\log$–$\log$ plots and verified the results by finite size scaling $C(x/L) = L^{\gamma}(x/L)^{\gamma}c(x/L)$ with exponent γ and system size L.

In the case of a hard–core dimer covering (quarter–filled checkerboard lattice), the exponent agrees with the results from [Krau 03], i.e., $C(x) \sim 1/x^{1/2}$. The correlations in the case of a loop covering (half–filled checkerboard) are well fitted by the power law $C(x) \sim 1/x^{1/3}$ which was obtained analytically (see above). Figure 3.4 shows the good agreement between the finite size scaling and the calculated exponent. As expected, the correlations do not show any angle dependence at large distances (not shown here). In both cases, the decay of the correlation function is algebraic, which is expected for 2D bipartite lattices: The two defects have long–range correlation and feel each others presence at all distances. The bipartiteness of the square lattice is also seen by the strictly zero correlations $C(x)$ for distances which connect sites that reside on the same sublattice.

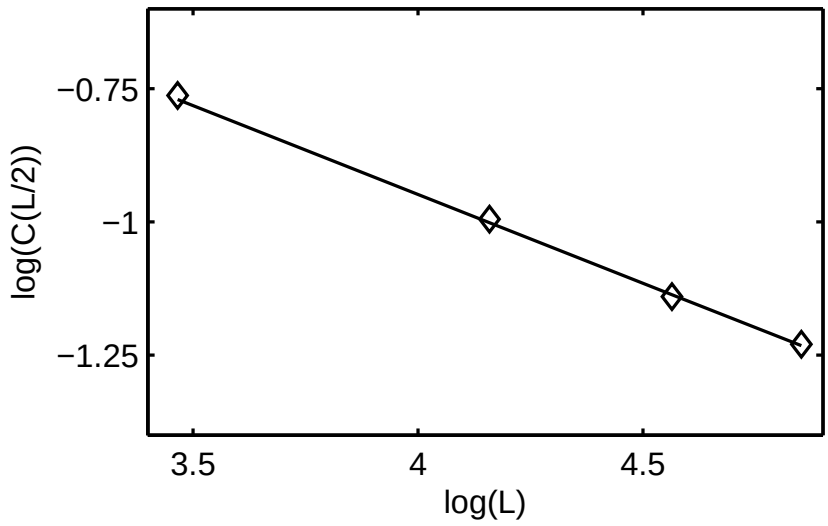

Figure 3.4: Finite size scaling of classical defect–defect correlation functions on a $L \times L$ square lattice with loop coverings. The numerical data are well fitted by the exact asymptotic result for the exponent $\gamma = 1/3$.

The algebraic decay to zero leads to a logarithmic confinement of fractional charges at any finite temperature.

3.3.2 Honeycomb lattice

The kagomé lattice with nearest–neighbor repulsion at one–third and two–third filling are mapped to the hard–core dimer and the loop model on the honeycomb lattice, respectively. The numerically obtained correlations along the axes of the Bravais lattice are both $C(x) \sim 1/x^{1/2}$ (see Figure 3.5). Consequently, the monomers are logarithmically confined. Note that the two models, i.e., filling factors one–third and two–third, are equivalent in the absence of defects. They can be identified by exchanging links which are occupied by a dimer and those which are not occupied. The faster algorithm described above did not show the equivalence of the two models. Therefore, we used the manifestly ergodic loop algorithm.

3.3.3 Triangular lattice

The kagomé lattice with repulsion on the hexagons only can be mapped at one–sixth filling to a hard–core dimer model and at one–third filling to a loop model on the triangular lattice. For small distances, the correlation functions decay exponentially in both cases (see Figure 3.6). The values obtained for the hard–core dimer model are in agreement with those obtained in [Fend 02]. For distances larger than a few lattice spacings, $C(x)$ is constant within the noise ratio and tends to a finite value in the limit $x \to \infty$ [Moes 01].

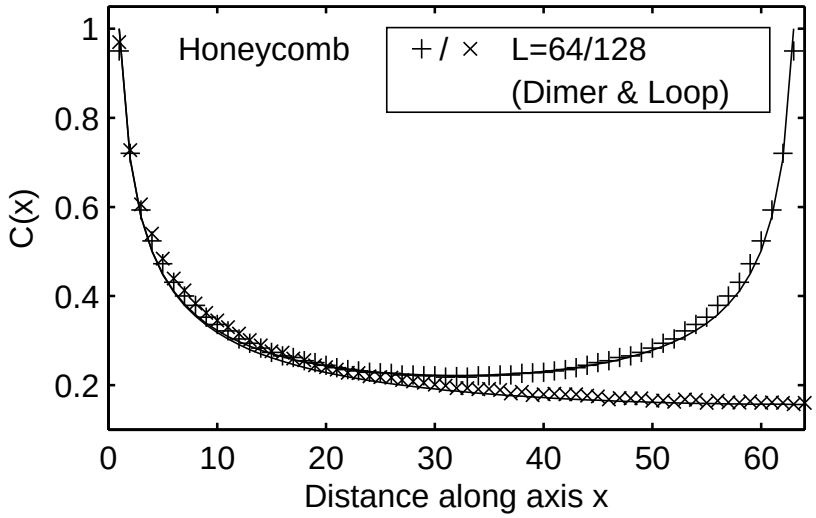

Figure 3.5: Classical defect–defect correlation functions on a honeycomb lattice with hard–core dimer and loop coverings along an axis of the Bravais lattice. Numerical results are shown for lattices with $L = 64$ and $L = 128$ together with a power law $\sim x^{1/2}$. The periodic boundary conditions are taken into account by plotting the fit against a rescaled distance variable.

This implies that the free energy difference (3.1) of two infinitely separated defects in the classical hard–core dimer and loop model is finite and the two defects are deconfined.

3.3.4 Diamond lattice

The pyrochlore lattice at quarter and half filling corresponds to the hard–core dimer and the loop model on the diamond lattice, respectively. Monte Carlo simulations for two different lattice sizes are shown in Figure 3.7. Many more samplings are needed in 3D than in 2D to achieve a good signal to noise ratio, because the phase space is considerably larger. From a logarithmic plot, we found that the correlation functions decay exponentially with respect to the inverse distance along the axes of the Bravais lattice as approximately $C(x) \sim \exp(\frac{1}{4x})$ for the hard–core dimer covering and approximately $C(x) \sim \exp(\frac{1}{6x})$ for the loop covering. The correlations decay in both cases to a finite value, and using (3.1) we conclude that fractional charges are deconfined.

The striking difference between 2D and 3D bipartite lattices, i.e., long range versus short range correlations, can be seen from the Coulomb gas approach [Nien 87]. Monomers in 3D follow a Coulomb law with potential $V(r) \propto 1/r$, as opposed to the divergence at large distances $V(r) \propto \log r$ which is seen in 2D [Huse 03]. The defect–defect correlations then decay exponentially with the inverse distance in the case of the diamond lattice. A recent work on spin 1/2 Heisenberg anti–ferromagnets on the pyrochlore lattice predicts a fractionalized spin liquid with $U(1)$ gauge structure where the $1/r$ potential acts between pairs of spinons and pairs of monopoles [Herm 04].

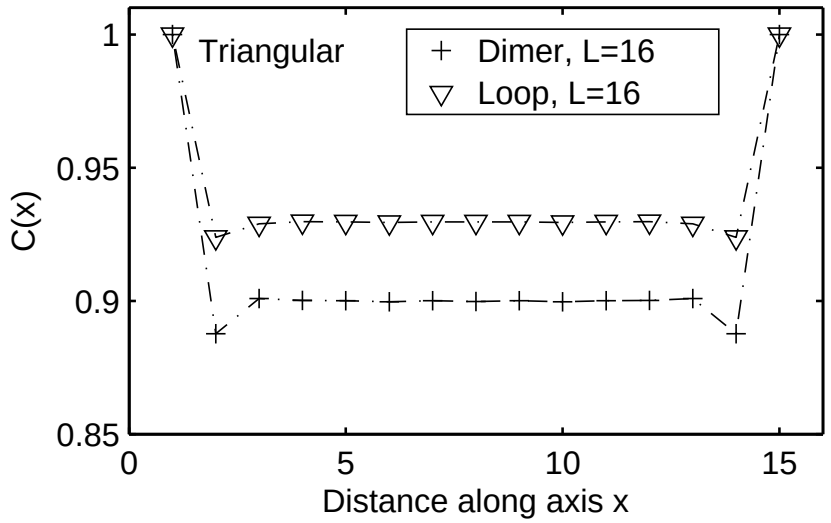

Figure 3.6: Classical defect–defect correlation functions on a triangular lattice with hard–core dimer and loop coverings along a coordinate axis. Lines are guides to the eye. Results are shown for a lattice with $L = 16$.

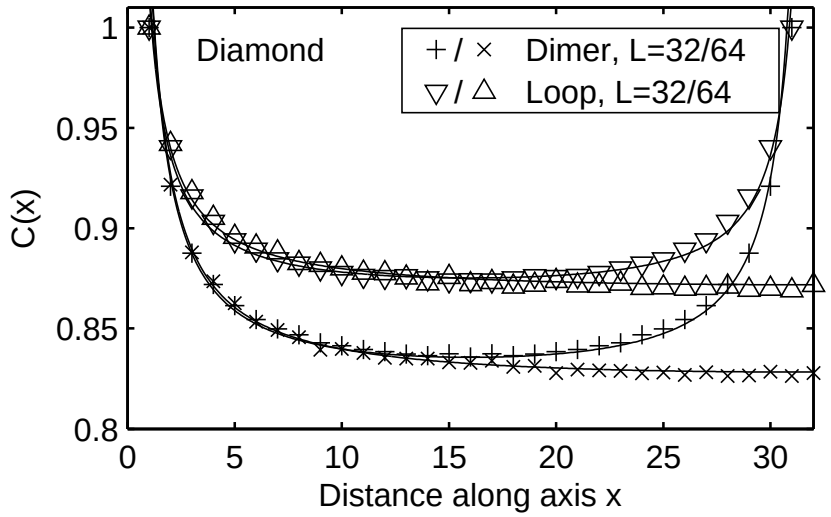

Figure 3.7: Classical defect–defect correlation functions on a diamond lattice with hard–core dimer and loop coverings along a coordinate axis. Results are shown for lattices with $L = 32$ and $L = 64$. Exponential functions are fitted to the numerical data. The periodic boundary conditions are taken into account by plotting the fit against a rescaled distance variable.

Chapter 4

Quantum mechanical studies of the checkerboard lattice

So far, we considered only the classical limit and excluded quantum fluctuation. In this chapter, we include quantum fluctuations and investigate quantum–mechanical properties of quarter– and half–filled checkerboard lattices. The macroscopic degeneracy, which is present in the classical limit, is lifted and the nature of the quantum–mechanical ground state is an open question. For a systematic study, we will first define an effective Hamiltonian [Rung 04] describing the low–energy excitations of spinless fermions in the regime $|t| \ll V$. The effective Hamiltonian and its implications will be discussed in detail. We then use numerical exact diagonalization of finite lattices to obtain the quantum–mechanical ground state as well as excited states. The nature of the former determines the confinement/deconfinement of two static fractionally charged particles (fcp's) and the latter give insight into the dynamical properties.

4.1 Effective Hamiltonian

We consider the model Hamiltonian (2.5) of spinless fermions on the crisscrossed checkerboard lattice. Written in terms of annihilations (creation) operators $c_i(c_i^\dagger)$ and density operators $n_i = c_i^\dagger c_i$, it reads

$$H = -t \sum_{\langle i,j \rangle} \left(c_i^\dagger c_j + \text{H.c.} \right) + V \sum_{\langle i,j \rangle} n_i n_j .$$

The band structure of non–interacting ($V = 0$) particles on the checkerboard lattice consists of a dispersive and a flat band

$$\begin{aligned} \varepsilon^-(\mathbf{k}) &= -2t - 4t \cos \frac{k_x a}{\sqrt{2}} \cos \frac{k_y a}{\sqrt{2}}, \\ \varepsilon^+(\mathbf{k}) &= 2t, \end{aligned} \tag{4.1}$$

where a is the lattice constant. In passing we mention that in the presence of interactions, correlations are generally strong in flat band regimes, because the kinetic energy does

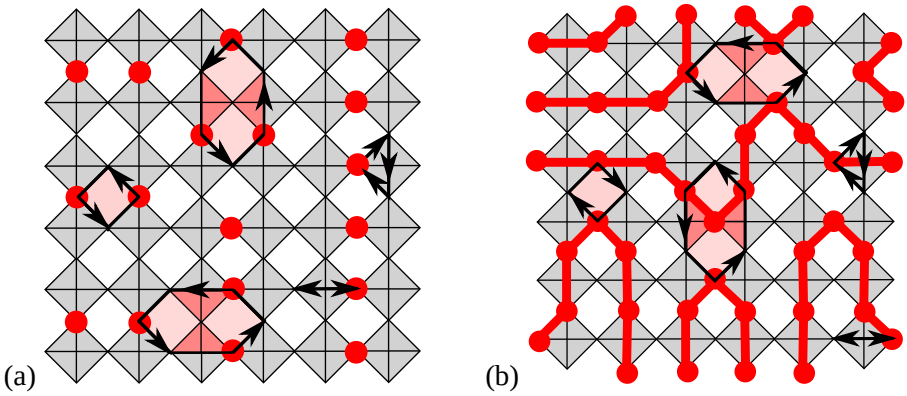

Figure 4.1: Examples of allowed configurations on a checkerboard lattice: (a) Quarter filling and (b) half filling with possible low–order hopping processes.

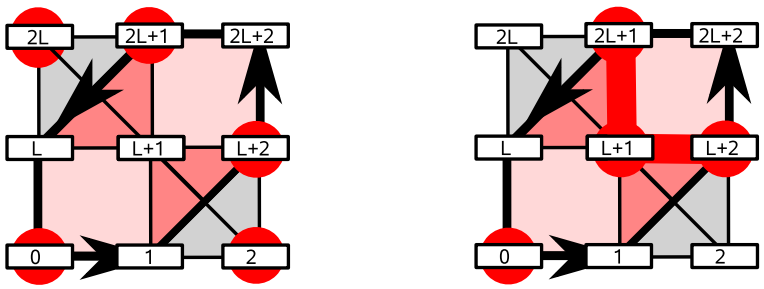

Figure 4.2: Difference between ring–hopping processes around hexagons with empty and occupied site in the center on a checkerboard lattice with $L \times L$ sites and row–wise enumeration.

not strongly counteract repulsions [Miel 91]. In the following, we assume $t > 0$. Note that our coordinate system is rotated by 45° relative to that of, e.g., [Rung 04]. The resulting difference in boundary conditions can lead to noticeable numerical differences in particular for very small cluster sizes.

Our main interest is the regime $0 < |t| \ll V$ of systems where one quarter ($n_f = 1/4$) or one half ($n_f = 1/2$) of the sites are occupied by fermions. The macroscopically degenerate classical ground–states at the considered filling factors are discussed in Chapter 3.

In the following, we discuss a Hamiltonian that acts only on the Hilbert space spanned by the allowed configurations and contains processes up to order t^3/V^2. The processes can be classified as self–energy contributions and ring–exchange processes (see Figure 4.1). The down–folded Hamiltonian reads

$$\mathcal{H} = H_\Sigma + H_{\text{eff}}.$$

Here, H_Σ comprises the terms that are diagonal in the real space basis and H_{eff} those which connect different allowed configurations. The diagonal part H_Σ contains self–energy contributions resulting from processes in which a fermion hops to an empty neighboring site or around an adjacent triangle and returns again to the same site (see Figure 4.1). H_Σ leads to a constant energy shift and does not lift the macroscopic degeneracy because in all allowed configurations the fermions have the same number of empty neighboring site. We find for the quarter– and half–filled checkerboard with N sites

$$H_\Sigma = -\frac{N}{4}\left(6\frac{t^2}{V} + 6\frac{t^3}{V^2}\right)$$

and

$$H_\Sigma = -\frac{N}{2}\,4\frac{t^2}{V}, \tag{4.2}$$

respectively. Note that in the half–filled case the t^3/V^2 contributions from hole– and particle–hoping around a triangle cancel each other. In the following, we will ignore H_Σ and consider H_{eff} only. The total amplitude of ring–exchange processes around empty squares is proportional to t^2/V. It vanishes for spinless fermions. This is due to the fact that these processes occur in both, clockwise and counter–clockwise direction, which have opposite signs and cancel each other. The same argument holds for all processes which involve $2m$ sites with m even—the right and left exchanges cancel due to the fermionic anti-commutation relations. The macroscopic ground–state degeneracy is first lifted by ring exchanges $\sim t^3/V^2$ around hexagons. Thus, the effective Hamiltonian reads

$H_{\text{eff}} = -g \sum_{\{\,,\,\}} \Big(\big|$  $\big\rangle\big\langle$  $\big| - \big|$  $\big\rangle\big\langle$  $\big| + \text{H.c.}\Big)$, (4.3)

with an effective hopping element $g = 12\ t^3/V^2 > 0$ and the sum taken over all vertical and horizontal oriented hexagons. The pictographic operators represent the hopping around hexagons which have either an empty or an occupied central site. In [Rung 04]

it has been shown that the effective Hamiltonian (4.3) gives a good approximation of the low–energy excitations of the full Hamiltonian (2.5) in the limit considered. The signs of matrix elements depend on the representation and the sequence in which the fermions are ordered. When the sites are enumerated row–wise as shown in Figure 4.2, an exchange process commutes an odd number of fermionic operators if the site in the center of the hexagon is empty and an even number if it is occupied. Thus, we find for the matrix elements of a flippable hexagon

$\langle f|$  $\rangle\langle$ $|i\rangle \;\rightarrow\; -1,$

$\langle f|$ 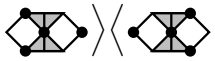 $\rangle\langle$ $|i\rangle \;\rightarrow\; 1.$

The ring–exchange processes in Hamiltonian (4.3) lead to negative matrix elements $-g$ whenever the site in the center of the hexagon is occupied and to positive matrix elements $+g$ when it is empty.

All configurations that fulfill the rule of having exactly *one* fermion on each tetrahedron, i.e., the classical ground states of the quarter–filled checkerboard, contain only flippable hexagons which have an empty site in the center. Consequently, in the chosen representation, all matrix elements have a non–negative sign and the system can equivalently be viewed as a hard–core bosonic system.

4.1.1 Height representation and conserved quantities

Conserved quantities of a Hamiltonian allow for a reduction of the numerical effort by exploiting the resulting block–diagonal form of the matrix representation. Furthermore, one can classify eigenstates by the eigenvalues of the conserved quantities as quantum numbers. We observe that Hamiltonian (4.3) connects only certain subsets of allowed configurations and refer to these as "subensembles". In the following, we specify different quantum numbers in order to characterize different subensembles. A topological quantity, which is conserved by all local processes, i.e., ring–exchange processes, is the average tilt in a scalar height field which will be introduced in the next paragraph. Another useful quantum number involves the number of particles on particular sublattices which will be introduced later on.

First, we show that allowed configurations of the quarter– and half–filled checkerboard can be represented by a vector field $\mathbf{f}$ for which the discretized lattice version of the curl vanishes. This vector field can thus be written as a pure, discrete gradient of a scalar field (height field) h, i.e.,

$$\mathbf{f} = \nabla h. \tag{4.4}$$

Figure 4.3 shows the vector field $\mathbf{f}$ as arrows on the sites of the checkerboard lattice and h as numbers in the non–crossed squares. In order to define the height field h, we begin by dividing the crisscrossed squares of the checkerboard into two sublattices A and B. The crisscrossed squares on sublattice A get a clockwise and on sublattice B a counter–clockwise orientation (see Figure 4.3). In the half–filled case (Figure 4.3 (b)), we define the field $\mathbf{f}$ by placing arrows of unit length on the sites of the checkerboard lattice. If

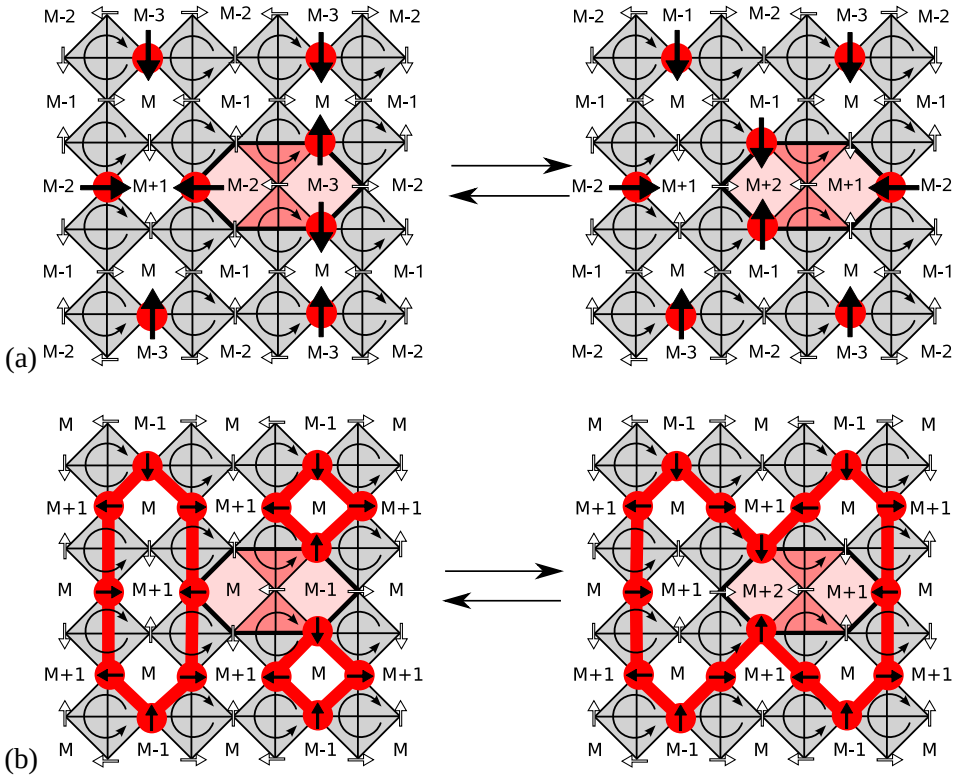

Figure 4.3: Height representation for examples of allowed configurations of a $\sqrt{32} \times \sqrt{32}$ checkerboard lattice with periodic boundary conditions at (a) quarter filling and (b) half filling. The height field is uniquely defined for a given configuration up to an additive constant M. Details of the mapping can be found in the text. The effect of a ring–exchange process around a hexagon on the height fields is shown explicitely.

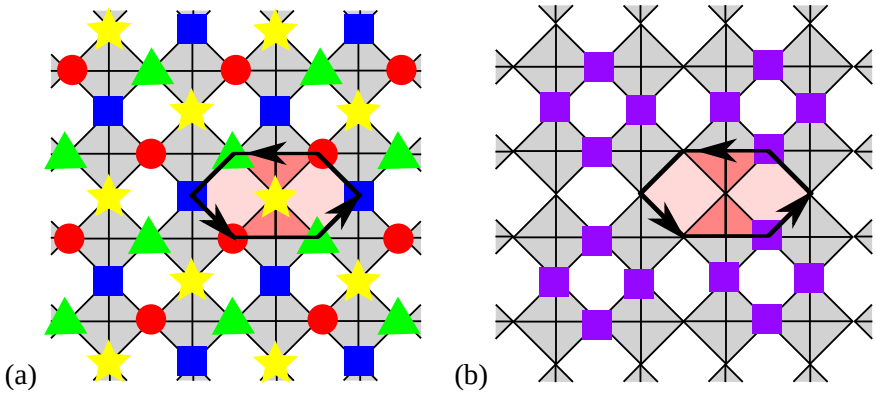

Figure 4.4: (a) The effective Hamiltonian conserves the number of fermions on each of the four sublattices of the checkerboard lattice which are labeled by blue squares, red circles, yellow stars and green triangles. (b) Ring–exchange processes change the number of fermions sites marked by purple squares by two.

the site is occupied, the arrows point in the same direction as the orientation assigned to the adjacent crisscrossed squares. If the site is empty, the arrows point in the opposite direction. In the quarter–filled case (Figure 4.3 (a)), we place arrows with length three on occupied sites and arrows with unit length on empty sites, following the same rule for the directions. With this recipe, the discretized line integral of $\mathbf{f}$ around crisscrossed squares vanishes in either case. Every integral over a closed loop in the lattice can be decomposed into integrals around crisscrossed squares. This enables us to define for each allowed configuration a scalar height h which satisfies (4.4) up to a constant M. For a finite lattice with periodic boundary conditions and $N_x \times N_y$ crisscrossed squares, the height at the upper and at the lower boundary can differ only by an integer $-N_y \leq \kappa_y \leq N_y$, which is the same for all columns. The same holds for the potential difference between the left and right side $-N_x \leq \kappa_x \leq N_x$. This defines topological quantum numbers (κ_x, κ_y), which we refer to as global slope. These topological numbers remain unchanged by all local processes that transform one allowed configuration into another, in other words, by ring–exchange processes along contractible loops. Ring hopping defined by H_{eff} belongs to that category. As seen in Figure 4.3, it merely lowers or raises the local potential of two adjacent plain squares by ± 2 in the half–filled case and ± 4 in the quarter–filled case. It follows that the subensembles of allowed configurations are characterized by their topological quantum numbers. This does not exclude degeneracies, i.e., several subensembles may have the same topological quantum numbers (κ_x, κ_y). For large system sizes this is necessarily the case as the number of subensembles grows faster with increasing system size than the number of realizable pairs (κ_x, κ_y).

The effective Hamiltonian has additional conserved quantities, which can be used for further classifications of subensembles. We can divide the sites of the checkerboard lattice into four sublattices as shown in Figure 4.4 (a). The effective Hamiltonian conserves the number of fermions on each sublattice. Consequently, we can decompose the Hilbert

space into sectors with fixed number of fermions on the four sublattices and label those by the quantum numbers $(N_{\mathcal{B}}, N_{\mathcal{Y}}, N_{\mathcal{G}}, N_{\mathcal{R}})$ which are conserved by H_{eff}.

For $(\kappa_x, \kappa_y) \neq (0, 0)$ it can be seen by inspection of different allowed local fermion arrangements that the lattice symmetry is broken [Rung 04]. Assume a positive average slope of h in the thermodynamic limit, i.e., a finite positive value of κ_x/N_x. This implies that it is more probable to find fermions along diagonal stripes. Furthermore, if the numbers $(N_{\mathcal{B}}, N_{\mathcal{Y}}, N_{\mathcal{G}}, N_{\mathcal{R}})$ are not equal, it implies immediately that it is more probable to find a fermion on the sublattice with the larger quantum number and that a charge density modulation is present. Thus, the lattice symmetry is preserved only in a sector with $(\kappa_x, \kappa_y) = (0, 0)$ and $N_{\mathcal{B}} = N_{\mathcal{Y}} = N_{\mathcal{G}} = N_{\mathcal{R}}$.

The matrix representation of the effective Hamiltonian is block–diagonal in the subensemble and each block corresponds to a set of quantum numbers $(N_{\mathcal{B}}, N_{\mathcal{Y}}, N_{\mathcal{G}}, N_{\mathcal{R}})$ and (κ_x, κ_y). We can diagonalize the Hamiltonian by diagonalizing each block separately. This reduces considerably the computational cost.

4.1.2 Signs of Hamiltonian matrix elements

For the identification of exactly solvable points in parameter space (see Section 4.2.1) or the future application of quantum Monte Carlo simulations, it is very advantageous to find a gauge transformation which determines the sign of matrix elements accordingly. We first present gauge transformations that change the sign of g in the effective Hamiltonian (4.3) and then show under which conditions it is possible to remove the sign problem, which results from fermionic statistics in the half–filled case.

Consider a sublattice $\mathcal{P}$ that contains the sites around every second plaquette as shown in Figure 4.4 (b). Ring–exchange processes change the number of fermions on this sublattice by two. We can multiply all configurations by a factor of

$$(-1)^{\frac{1}{2}\sum_{i\in\mathcal{P}} n_i},$$

where the sum is taken over all sites of the purple sublattice $\mathcal{P}$ and the operators n_i are equal unity if site i is occupied and zero otherwise. This gauge transformation changes the sign of each ring exchange and thus proves that the sign of g can be chosen arbitrarily ($g \leftrightarrow -g$ symmetry).

We can use the above transformation for the quarter– and half–filled case to change the overall sign of g. However, a sign problem remains in the half–filled case since the matrix elements of the effective Hamiltonian (4.3) have different relative signs.

The sign problem, manifested in the opposite signs of the ring–exchange processes around empty and occupied hexagons in (4.3), can be avoided in certain (but not all) cases. We make use of the fact that we can represent the ground–state manifold as fully–packed loops (the mapping is presented in Chapter 3). We notice that ring exchange around hexagons with an occupied site in the center does not change the loop topology (and their number). In contrast, ring exchange around empty hexagons always does. The three topological different cases are shown in Figure 4.5 (a). Let us consider configurations

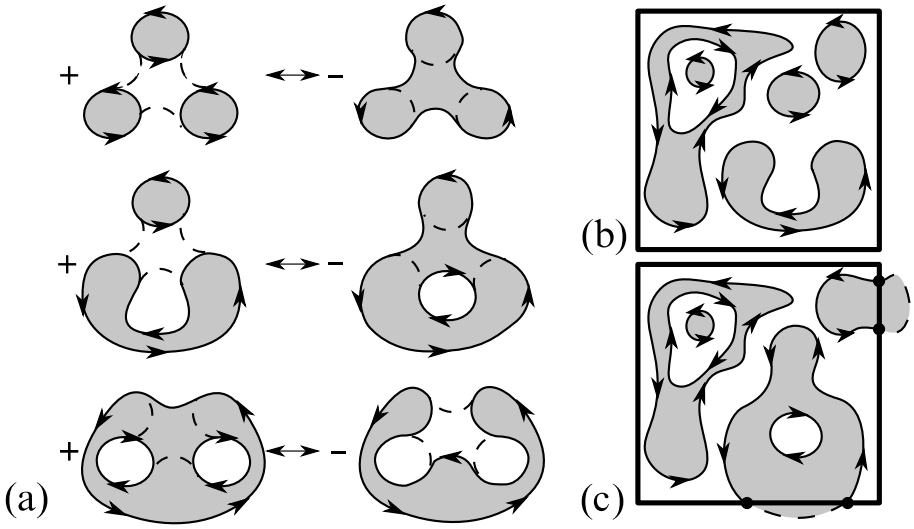

Figure 4.5: The three different actions of the effective Hamiltonian on the topology of loop configurations are shown in panel (a). Panels (b) and (c) show representations of two configurations by fully–packed directed loops.

with an even number of fermions remaining fixed at the boundary ("fixed" boundary conditions). Then, fermion configurations are represented by closed loops as well as loops terminating at the boundary (arcs). First, we consider closed loops (Figure 4.5 (b)). We orient these as follows: (i) Color the areas separated by the loops white and grey, with white being the outmost color; (ii) orient all loops so that the white regions are always to the right. In the presence of arcs (Figure 4.5 (c)) we can choose how to close them on the outside without intersections (the outside region has no dynamics). Letting white be the color at infinity, we orient the loops as described above. We now notice that the relative signs resulting from the exchange processes around empty hexagons are consistent with multiplying each loop configuration by

$$i^r(-i)^l, \tag{4.5}$$

where $r(l)$ is the total number of the (counter–)clockwise winding loop. Hence, by simultaneously changing the sign of the exchange–processes around empty hexagons and transforming the loop states

$$|\mathcal{L}\rangle \quad \rightarrow \quad i^{l(\mathcal{L})}(-i)^{r(\mathcal{L})}|\mathcal{L}\rangle, \tag{4.6}$$

we cure the sign problem, thus making the system effectively bosonic.

Note that this construction need not work for periodic boundary conditions: Firstly, only even–winding sectors on a torus allow two-coloring, and secondly, even for the even windings, it might be possible to dynamically reverse the coloring while returning to the same loop configuration, resulting in non–trivial state counting. It appears though that for the periodic boundary conditions on *even* tori (preserving the bipartiteness of the

lattice), the lowest–energy states belong to the sector where such a transformation works. At least this is suggested by the exact diagonalization results below. We also remark that the presented non–local loop-orienting construction is restricted to the ring-exchange processes of length six, i.e., to the effective Hamiltonian (4.3).

4.1.3 Doped system

Placing one additional fermion with charge e onto an empty site leads to a violation of the tetrahedron rule on two adjacent crisscrossed squares. These two local defects can separate without creating additional defects, thereby gaining additional kinetic energy of order t, see Section 2.2.

This finding motivates the introduction of an extra term into the effective Hamiltonian (4.3) that moves the defects and acts only on the subspace of allowed configurations in the presence of a given number of defects:

$$H_{\rm tg} \;=\; H_{\rm eff} - t \sum_{\langle i\ j\rangle} P \left(c_i^\dagger c_j + \text{H.c.} \right) P. \tag{4.7}$$

It includes the lowest order ring–exchange processes $H_{\rm eff}$ and a projected hopping term. We will refer to this effective Hamiltonian as the tg model. The hopping t is projected by the projector P onto the manifold of allowed configurations in the presence of a fixed number of defects, i.e., two in the case of one added fermion. By introducing the independent parameters t and g, the effect of ring exchange onto the dynamics of fractionally charged excitations can be determined. The tendency for confinement can be studied even on rather small clusters by increasing the ring exchange strength g relatively to t.

4.2 Ground states and lowest excitations

In this section, we investigate the nature of the quantum–mechanical ground state. In particular, we want to make statements about confinement of fcp's. We introduce an additional parameter to study different phases and obtain the quantum–mechanical ground state by means of exact diagonalization. The computational effort increases exponentially with the system size. In order to be able to consider clusters of reasonable size, we diagonalize the effective Hamiltonian (4.3) instead of the full Hamiltonian (2.5). The effective Hamiltonian acts only on the subset of allowed configurations and the size of the low–energy Hilbert space grows much slower with the number of sites than the full Hilbert space.

4.2.1 Half filling

We begin by studying a Hamiltonian which includes in addition to $H_{\rm eff}$ an extra term that counts the number of flippable hexagons (see Rokhsar and Kivelson [Rokh 88]). That number is an essential parameter to understand the effect of the kinetic energy term. The original Hamiltonian plus the extra term reads

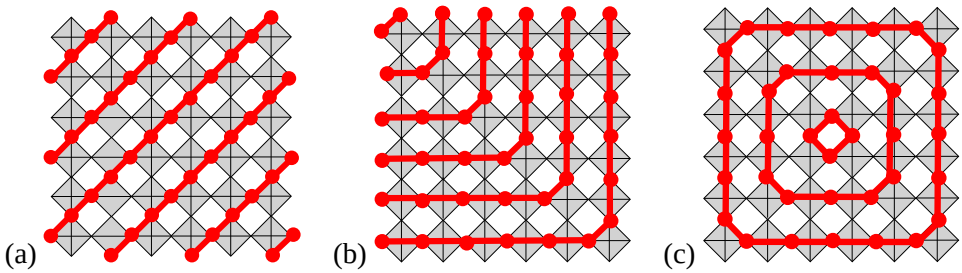

Figure 4.6: Fragments of possible "frozen" ground states: (a) no fluctuations under any local ring exchange, (b) and (c) no fluctuations only in fermionic systems. Neighboring occupied sites (dots) are connected by a solid line.

$$H_{g\mu} = H_{\text{eff}} + \mu \sum_{\{\hexagon,\hexagon\}} \Big(\Big| \hexagon \Big\rangle\Big\langle \hexagon \Big| + \Big| \hexagon \Big\rangle\Big\langle \hexagon \Big| \Big) , \qquad (4.8)$$

where the pictographic operators with grey–colored dots in the center are summed over flippable hexagons, independent of the occupancy of the site in the center. In some limiting cases, we can solve the Hamiltonian (4.8) exactly and study possible phases of it.

$\mu \to +\infty$**:** Ground states are all configurations which contain no flippable hexagons, i.e., they consist of all configurations that are not connected to any other configuration. The ground states have a gap to the first exited state which is of order μ. We can easily find configurations that have no flippable hexagons. There are ground states which are completely analogous to the staggered ground state of the quantum–dimer model (QDM) on the square lattice, i.e., they remain frozen by any local ring exchange.

Quite interestingly, there are in addition numerous ground states (see Figure 4.6) which remain unaffected by any fermionic dynamics but would not be so in the bosonic case. This is seen by recalling, that in the fermionic case only ring exchanges are allowed of perimeter $2m$ with m being an *odd* integer. The energy of two static fractional charges is independent of the distance between them and thus they are deconfined. In other words, we can find configurations with arbitrary distances between two fcp's that have no flippable hexagons.

$\mu \to -\infty$**:** Ground states are configurations with maximal number of flippable hexagons N_{fl}. To find the configurations which maximize N_{fl}, we introduce a simple Metropolis–like Monte Carlo algorithm. The algorithm begins with an arbitrary allowed configuration as initial configuration. Then we produce a vacuum fluctuation (one crisscrossed square with three fermions and one with one fermion) and let the two defects propagate randomly. When the defects have annihilated each other, we obtain a new allowed configuration. This update technique can reach *all* allowed configurations, i.e., it is ergodic within the space of allowed configurations. The ergodicity can be seen explicitely from

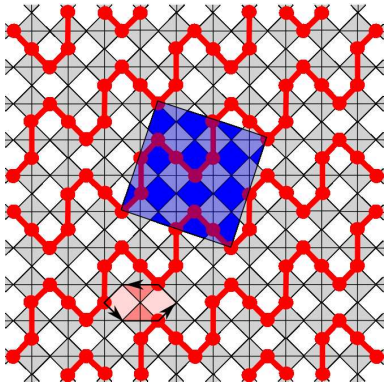

Figure 4.7: One of several configurations of the half–filled checkerboard lattice maximizing the number of flippable hexagons. The unit cell contains $\sqrt{20} \times \sqrt{20}$ sites. Neighboring occupied sites (dots) are connected by a solid line.

the fact that any difference between two allowed configurations can be represented in terms of closed loops with alternating occupied and empty links [Bark 98]. In order to maximize $N_{\rm fl}$, we accept a new configuration with a higher probability if the number of flippable hexagons $N_{\rm fl,new}$ of the new configuration has increased. The probability to accept a new configuration is given by

$$P\left(N_{\rm fl,new}\right) \sim \begin{cases} 1 & , N_{\rm fl,new} - N_{\rm fl,old} \geq 0 \\ e^{\beta\left(N_{\rm fl,new} - N_{\rm fl,old}\right)} & , N_{\rm fl,new} - N_{\rm fl,old} < 0 \end{cases} ,$$

where the parameter β serves merely as a control parameter to assure fast convergence. If a new configuration has been accepted, we take it as the initial configuration for the next iteration, otherwise we restore the previous one. We find the maximum of $N_{\rm fl}$ by taking the configuration with maximal $N_{\rm fl}$ of all accepted configurations. For a checkerboard lattice with 200 sites and $\beta = 5$ about 10^6 iterations are necessary to maximize $N_{\rm fl}$.

Applying the algorithm to lattices with up to 1000 sites and different boundary conditions, we find configurations of the type shown in Figure 4.7 to maximize $N_{\rm fl}$. The maximal number of flippable hexagons $N_{\rm fl}$ is proportional to the number of lattice sites N. The unit cell has $\sqrt{20} \times \sqrt{20}$ sites and we will refer to those as "squiggle" configurations [Penc 06]. For a lattice with N sites, we find five degenerate ground–state configurations with the quantum numbers $(N_{\mathcal{B}}, N_{\mathcal{Y}}, N_{\mathcal{G}}, N_{\mathcal{R}})$=$(3\frac{N}{20}, 3\frac{N}{20}, 2\frac{N}{20}, 2\frac{N}{20},)$ and another five with $(N_{\mathcal{B}}, N_{\mathcal{Y}}, N_{\mathcal{G}}, N_{\mathcal{R}})$=$(2\frac{N}{20}, 2\frac{N}{20}, 3\frac{N}{20}, 3\frac{N}{20})$. All are within the $(\kappa_x, \kappa_y) = (0, 0)$ sector. In the thermodynamic limit, the system has a crystalline ground state and a gap of μ to the first excited state. If a system with periodic boundary conditions is considered and the unit cell does not fit into the cluster, modified versions of the squiggle configuration form to maximize $N_{\rm fl}$.

We use the above introduced Monte Carlo algorithm also to consider static fractional charges in our model. For this, we generate an initial configuration with two fcp's at fixed position $\mathbf{0}$ and $\mathbf{r}$ with a distance $d = |\mathbf{r}|$ along a diagonal (distance is measured by the

number of crisscrossed squares). We maximize the number of flippable hexagons $N_{\rm fl}$ for different distances d. It turns out that the maximal $N_{\rm fl}$ is decreased by two if d is increased by one. Consequently, the energy increases linearly with the distances of the two defects (or fcp's) which leads to confinement by a constant confining force.

$\mu = g > 0$**:** This point is the exactly solvable Rokshar–Kivelson (RK) point [Rokh 88]. The ground states are completely analogous to the above considered configurations which remain frozen by local ring exchanges (see Figure 4.6). In addition to the states remaining unchanged, there are also liquid–like ground states, similarly to the original RK construction. In the following, we want to construct these liquid–like ground states. We can rewrite Hamiltonian (4.8) as

$H_{\rm g=\mu} = g \sum_{\{\bigcirc,\bigcirc\}} \left(\left| \right\rangle - \left| \right\rangle \right) \left(\left\langle \right| - \left\langle \right| \right)$
$+ g \sum_{\{\bigcirc,\bigcirc\}} \left(\left| \right\rangle + \left| \right\rangle \right) \left(\left\langle \right| + \left\langle \right| \right) .$ (4.9)

Since (4.9) is a sum over projectors, we know that all eigenvalues are non–negative. Let us use the gauge transformation (4.6) to rewrite the Hamiltonian (4.9):

$H_{\rm g=\mu} = g \sum_{\{\bigcirc,\bigcirc\}} \left(\left| \right\rangle - \left| \right\rangle \right) \left(\left\langle \right| - \left\langle \right| \right)$
$+ g \sum_{\{\bigcirc,\bigcirc\}} \left(\left| \right\rangle - \left| \right\rangle \right) \left(\left\langle \right| - \left\langle \right| \right) .$ (4.10)

Here we have a form in which *all* off-diagonal elements are non–positive. Under this condition, we can write down the exact ground–state wavefunction which has zero energy for each subensemble. Each subensemble has a unique ground state which is given by the equally weighted superposition of all configurations within that subensemble. A ground–state wavefunction reads

$$|\psi^{(l)}_{0,RK}\rangle = \frac{1}{\sqrt{N^{(l)}_{\rm dim}}} \sum_i |C^{(l)}_i\rangle,$$

where the sum is taken over all configurations i of the subensemble (l) with $N^{(l)}_{\rm dim}$ dimensions. The corresponding energy can be easily computed: We gain the energy $-g$ for each flippable hexagon and loose $+\mu$. Thus, we find for $g = \mu > 0$ the ground-state energy

$$\langle \psi^{(l)}_{0,RK} | H_{\rm g\mu} | \psi^{(l)}_{0,RK} \rangle = 0.$$

In other words, the state $|0\rangle$ is automatically annihilated by all projectors in the transformed Hamiltonian (4.10). Since all off–diagonal elements are non–positive, the ground state has only positive amplitudes and $|\psi^{(l)}_{0,RK}\rangle$ is the unique ground state for each subensemble. These coherent superpositions are the analogs of the Resonating Valence Bond

(RVB) state, originally discussed by P. W. Anderson [Ande 73]. Fcp's are deconfined and the energy independent of the distance between them. For fermionic systems, we find a well defined RK point only if a gauge transformation exists, such that all off–diagonal matrix elements are non–positive. If such a transformation does not exist, the energy is larger than zero and the subensembles do consequently not form a ground state.

Exact diagonalization. Now that we know the ground states in the limiting cases $\mu = \pm\infty$ and $\mu = g$, we want to explore the phases for a finite range of μ values. Therefore, we investigate the quantum mechanical ground state of small clusters by means of exact diagonalizations. First, we generate all allowed configurations that fulfill the tetrahedron rule. Then we sort the configurations according to the quantum numbers into subensembles and generate a block–diagonal matrix representation of the Hamiltonian (4.8). We can finally find the ground state of the system from diagonalization of sparse block–diagonal matrices. The actual diagonalization is done using the Lanczos algorithm, which is described in Appendix B.1. We find qualitatively the same results for clusters of different size, ranging from 32 to 72 sites. In the following, we consider a 72–site checkerboard cluster with periodic boundary conditions. The low–energy Hilbert space of allowed configurations has $16\ 448\ 400$ dimensions and can be decomposed into a few hundred subensembles, where the largest one has $1\ 211\ 016$ dimensions. The sparse block–diagonal matrix of the Hamiltonian can be easily diagonalized on a 64 bit workstation. We can then extract relevant informations about the system from the quantum mechanical ground state $|\psi_0\rangle$, e.g., charge density distribution, density–density correlations, and energies.

Figure 4.8 shows ground–state energies as well as energies of the lowest excited states for $\mu = -g \ldots 1.2g$ and $g > 0$ of all subensembles. The two degenerate ground states $|\psi_0^{(1)}\rangle$ and $|\psi_0^{(2)}\rangle$ for $\mu < g$ lie within the subensembles which contain configurations with the maximal number of flippable hexagons. Both are within the $(\kappa_x, \kappa_y) = (0, 0)$ sector and the number of fermions on the four sublattices are $(N_\mathcal{B}, N_\mathcal{Y}, N_\mathcal{G}, N_\mathcal{R}) = (6, 6, 12, 12)$ and $(N_\mathcal{B}, N_\mathcal{Y}, N_\mathcal{G}, N_\mathcal{R}) = (12, 12, 6, 6)$, respectively. The states $|\psi_0^{(1)}\rangle$ and $|\psi_0^{(2)}\rangle$ are related by a rotation of 90° around a symmetry axis of the checkerboard lattice. Because of the periodic boundary conditions and the small size, we find a modified version of the squiggle configurations. These maximize the number of flippable hexagons which fit into the cluster under the constraint of periodic boundary conditions. We saw above that the system is in a crystalline state for $\mu \to -\infty$. The diagonalization of the finite clusters shows for $\mu < g$ no level crossing of ground states as indication for phase transitions, i.e., the ground state is always in the same subensemble, and we expect the system to stay in a crystalline phase. However, a level crossing of the first excited states at $\mu \approx 0.9g$ might indicate a transition from the squiggle phase to a phase with a different order. Consequently, at the physical point with $\mu = 0$, the system is in a crystalline and confining phase. In the thermodynamic limit, we expect to recover the 10–fold degeneracy of the squiggle phase instead of the two–fold degeneracy found from the diagonalization of finite systems. For small μ, the average weight of configurations in the ground state with the maximum number N_fl in Figure 4.9 is large. For $\mu \to g$ it

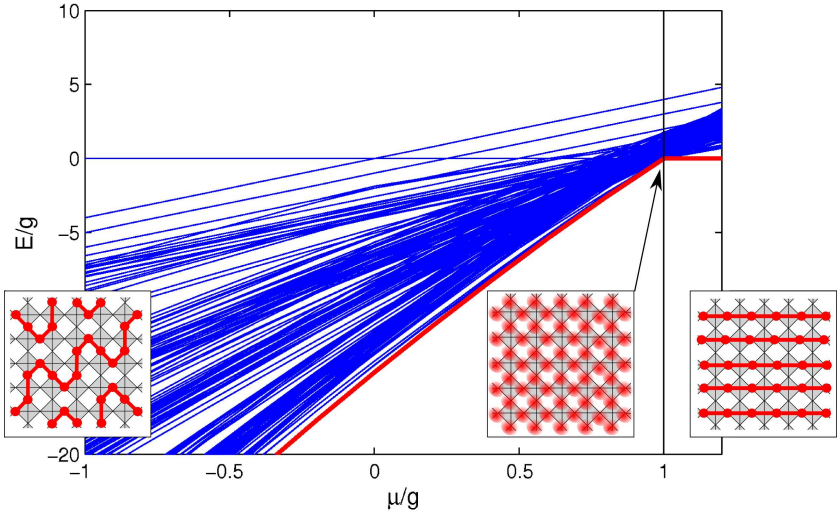

Figure 4.8: Energies of the ground state and lowest excited states in each subensemble of a 72–site half–filled checkerboard cluster for different values of μ of the $g\mu$ Hamiltonian. Level crossing of ground states occurs only at $\mu = g$. The insets indicate different phases: Maximal flippable plus fluctuations for $\mu < g$, a critical point $\mu = g$ where the ground state is an equally weighted superposition of all configurations, and isolated configurations as ground states for $\mu > g$.

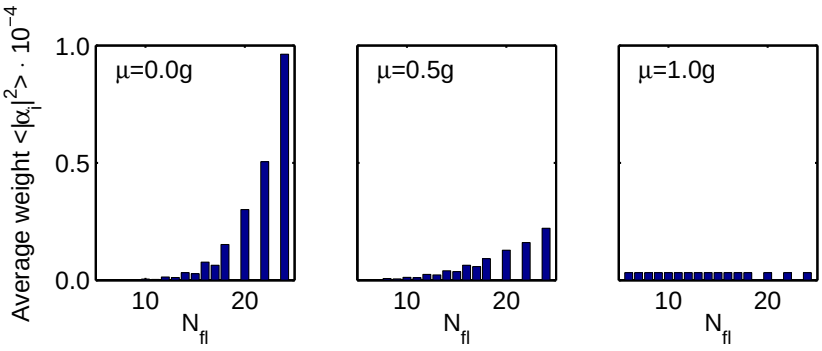

Figure 4.9: Average weight $\langle|\alpha_i|^2\rangle$ of a configuration $|c_i\rangle$ with $N_{\rm fl}$ flippable hexagons in the quantum mechanical ground states $|\psi_0^{(l)}\rangle = \sum_i \alpha_i |c_i\rangle$ of a $\sqrt{72} \times \sqrt{72}$ checkerboard cluster for different values of μ.

	E_0	E_1	E_2	E_3
Energy / g	-14.4631	-14.3976	-14.0027	-13.9739
Degeneracy	2	2	2	2

Table 4.1: Lowest energies and degeneracies of the effective Hamiltonian on a half–filled $\sqrt{72} \times \sqrt{72}$ checkerboard cluster.

becomes the same for all configurations. This can be interpreted as a further indication for the presence of a crystalline phase at $\mu = 0$.

For $\mu = g$, we are at the above described RK point. The ground state is formed by equally weighted superpositions of all configurations of certain subensembles. The degeneracy is determined by the number of disconnected subensembles. As a consequence of the fermionic signs, we observe that not all subensembles form a ground state with zero energy. These are subensembles in which the Fermi sign can not be removed by a suitable gauge transformation.

For $\mu > g$, we find isolated configurations as ground states and the physical properties are the same as described above in the limit $\mu \to \infty$.

The lowest energies and degeneracies for $\mu = 0$ are shown in Table 4.1. The two–fold degenerate states are related by a rotation of 90° and reflect the symmetry of the Hamiltonian. Figure 4.10 compares energies of a system in which the Fermi sign is taken into account by calculations in which we neglect the Fermi sign. Ground–state energies as well as the first excited states in the $(\kappa_x, \kappa_y) = (0, 0)$ sector are the same in both cases. In subensembles $(\kappa_x, \kappa_y) \neq (0, 0)$, the energies of the ground states including the Fermi sign are generally higher than the ones for bosons. It also turns out that the weights of the different configurations in the corresponding eigenstates are the same in both cases. States for which the fermionic phase cannot be fixed are much higher in energy and do not mix with the ground states. The fermionic or bosonic nature of the low lying excitations are indistinguishable as long as the allowed motions are ring-exchange processes of length six.

The ground states within the subensembles are unique and the quantum numbers $(N_\mathcal{B}, N_\mathcal{Y}, N_\mathcal{G}, N_\mathcal{R}) = (6, 6, 12, 12)$ and $(N_\mathcal{B}, N_\mathcal{Y}, N_\mathcal{G}, N_\mathcal{R}) = (12, 12, 6, 6)$ reflect the charge order which is shown in Figure 4.11 (a) and (b). We find a stripe order on the alternating stripes with an average occupation of $1/3$ and $2/3$, respectively. Figure 4.11 (c) and (d) show the density–density correlation function

$$C^{(l)}_{i_0 i} = \langle \psi^{(l)}_0 | n_i n_{i_0} | \psi^{(l)}_0 \rangle - \langle \psi^{(l)}_0 | n_i | \psi^{(l)}_0 \rangle \langle \psi^{(l)}_0 | n_{i0} | \psi^{(l)}_0 \rangle. \tag{4.11}$$

Note that panels (c) and (d), even though looking quite similar, show the correlations of inequivalent sites, with the center i_0 in one case having on average an occupation of $1/3$ and in the other case an occupation of $2/3$. The correlations in the quantum–mechanical ground states are best understood as reflecting the algebraic correlations present in the classically degenerate allowed manifold. They are the sum of the correlations of all allowed configurations with equal weight and are shown in Figure 4.11 (e). Specific

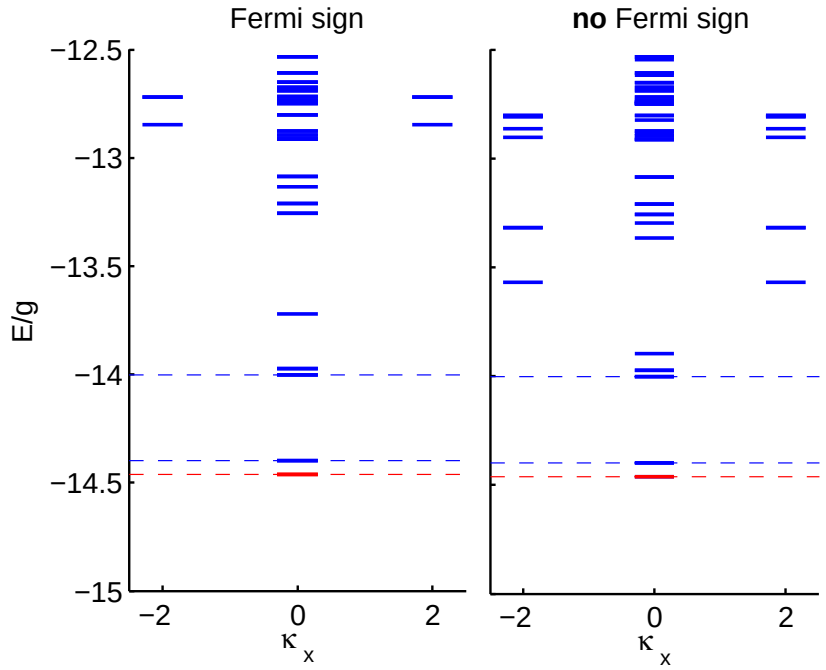

Figure 4.10: Ground–state energy (in red) and energies of lowest excited states of the effective Hamiltonian $H_{\rm eff}$ in sectors with different global slopes $(\kappa_x, \kappa_y) = (\kappa_x, 0)$. The left panel shows the data from an exact diagonalization of a 72–site cluster where the Fermi sign is taken into account. The right panel shows the same data from a calculation with equal signs of all matrix elements.

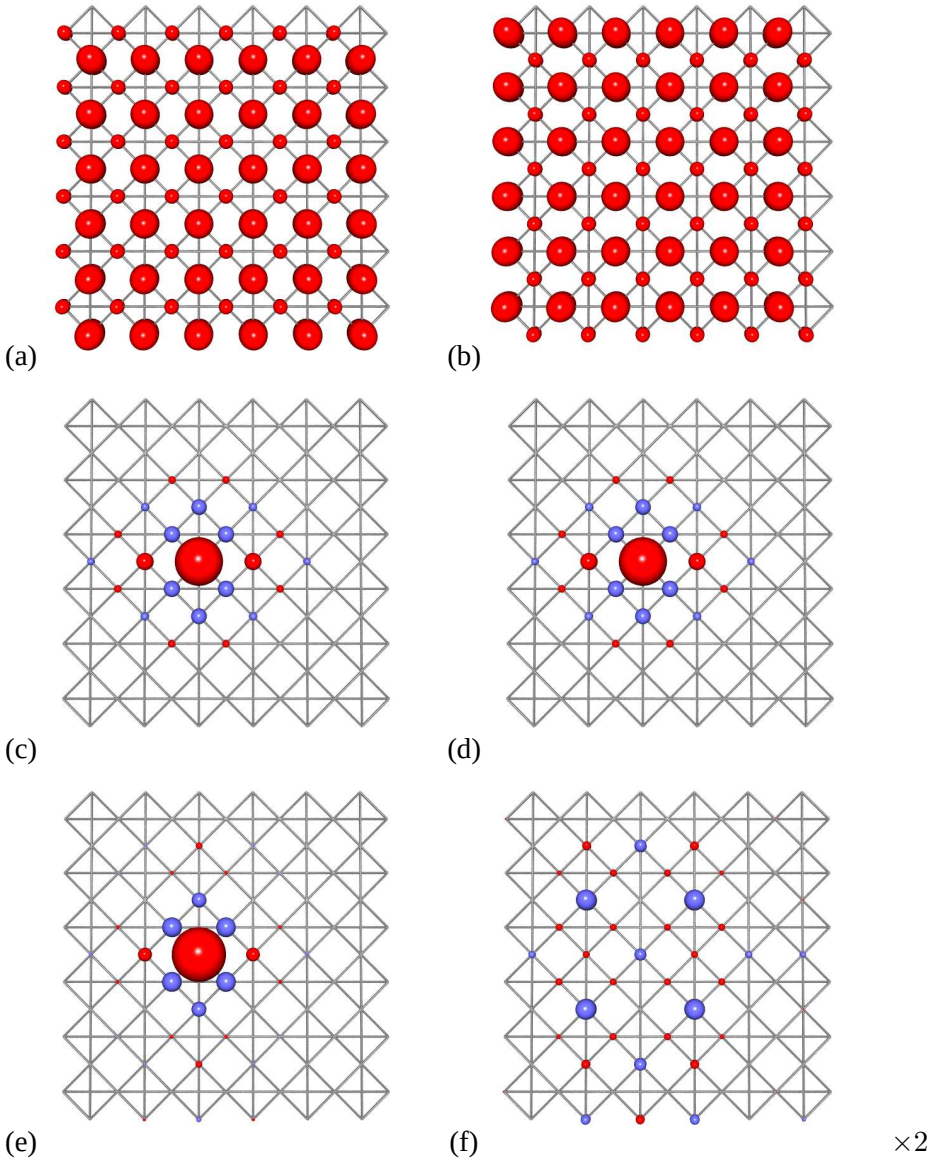

Figure 4.11: Half filling: Panels (a) and (b) show the charge density distribution $\langle\psi_0^{(l)}|n_i|\psi_0^{(l)}\rangle$, while (c) and (d) show the density–density correlation function $C_{i_0 i}^{(l)}$ for the two degenerate ground states $|\psi_0^{(l)}\rangle$ with $l = 1, 2$. Panel (e) shows the classical density–density correlation function which is obtained by averaging over all allowed configurations. The radius of the dots is proportional to the absolute value. A red or blue color represents a positive or negative value, respectively. The site i_0 is chosen arbitrarily and shows up as the largest dot in the panels (c)–(e). The difference between (c) and (e) is shown in (f).

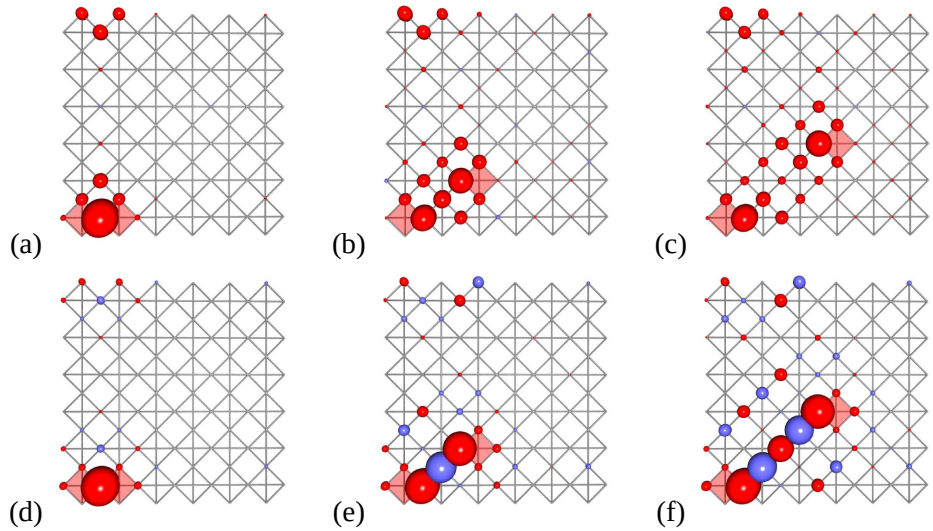

Figure 4.12: (a)–(c): Local loss of kinetic energy due to the separation of two fractionally charged defects (two fcp's). Radius of the dots is proportional to the local energy loss. The positions of fcp's are shown by red crisscrossed square. (d)–(f): Red (blue) dots show an increase (decrease) of the local density (vacuum polarization due to two fcp's).

quantum–mechanical features resulting from the ring hops become visible by determining the difference of the actual correlations of panel (d) and the classical correlations (e) [Rung 04]. This is shown in panel (f). A negative value at the central site i_0 indicates the expected general reduction of fluctuations compared to the generic value.

Next, we place an additional particle onto an empty site of the checkerboard lattice. Hereby we select that particular ground state which in the presence of the added particle gives the lowest energy. As a consequence, two neighboring crisscrossed squares have three particles attached to them. Recall that the separation of the two crisscrossed squares, containing three particles; each generates a string. It consists of an odd number of sites and is linked to two loops with an even number of sites each. The fractional charges of $e/2$ sit at the ends of a string.

We determine the changes of the kinetic energy density in the presence of the two charges $e/2$. This is done by keeping the two crisscrossed squares with the fractional charges fixed at **0** and **r** and determining the ground state $\bar{\psi}_0^{\mathbf{0r}}$ and its energy for a cluster of 72 sites. The latter can be decomposed into local contributions by calculating the following expectation value of the energy at site i

$$\epsilon_i = -\frac{g}{6} \sum_{\{\hexagon, \hexagon \mid i \in \hexagon\}} \left\langle \bar{\psi}_0^{\mathbf{0r}} \right| \left(\pm \left| \hexagon\hexagon \right\rangle \left\langle \hexagon\hexagon \right| + \text{H.c.} \right) \left| \bar{\psi}_0^{\mathbf{0r}} \right\rangle . \quad (4.12)$$

The sum is over all hexagons containing site i and the sign depends on the occupancy of the central site. The result is shown in Figure 4.12 (a)–(b). One notices a decrease in kinetic energy in the region between the two fractional charges, i.e., along the connecting

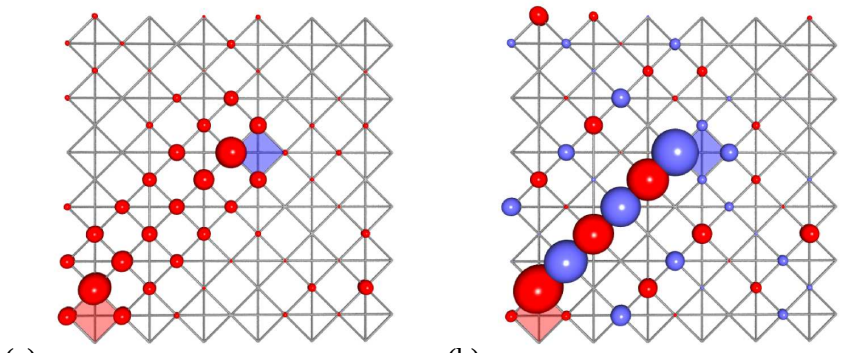

(a) (b)

Figure 4.13: (a): Local loss of kinetic energy due to the separation of two fractionally charged defects. Radius of the dots is proportional to the local energy loss. The position of the fcp is shown by a red crisscrossed square and the fch by a blue colored one. (b): Red (blue) dots show an increase (decrease) of the local density (vacuum polarization due to a fcp–fch pair).

string. The reason is that due to the topological changes caused by the generated string the number of flippable hexagons positioned between the fractional charges is decreased. The energy decrease is approximately proportional to the length of the generated string and implies at large distances a constant confining force. Consider a configuration with two defects of charge $e/2$ separated along a diagonal (see Figure 4.12 (a)–(c)). Then we find that the maximal number of flippable hexagons is reduced by $2d$, where d is the number of crisscrossed squares between the defects, as shown above in the limit $\mu \to -\infty$. We have also determined the density changes caused by the separation of the fractional charges (see Figure 4.12 (d)–(f)). They are obtained from the ground state in the presence of the two defects $|\bar{\psi}_0^{\mathbf{0r}}\rangle$ by simply calculating

$$\delta n_i = \langle \psi_0^{\mathbf{0r}} | n_i | \psi_0^{\mathbf{0r}} \rangle - \langle \bar{\psi}_0 \mid n_i \mid \bar{\psi}_0 \rangle \,. \tag{4.13}$$

While the total changes add up to zero, the vacuum is modified by the breaking up of the charge. It is polarized along the connecting string. The same findings discussed here apply also when a particle is removed from the ground state or when a particle–hole excitation is generated out of the ground state, see Figure 4.13. The calculations have been performed in a reduced Hilbert space in which only two static defects are present. In a calculation in the full Hilbert space the energy would not increase linearly to infinity, but the connecting string is expected to break when the energy increase is larger than the repulsion energy V. In other words, additional defects (fcp–fch pairs) are created if it is energetically preferable. For the relevant parameters (e.g., $g = 0.01t$ and $V = 10t$) this occurs when two fcp's have separated over 1000 lattice sites. This effect is also known for the case of confined quarks where pair production (quark anti–quark pairs) occurs before the quarks have been separated to an observable distance.

Excitations at the RK point The above described RK point of Hamiltonian (4.8) has the particular property that fcp's are deconfined. The excitations at this point are analyzed using a relation to the height model and the single–mode approximation. We make use of a mapping of allowed configurations to the fully packed loop (FPL) model (see Chapter 3 for details). Hamiltonian (4.8) acting on the fully–packed loop representation reads

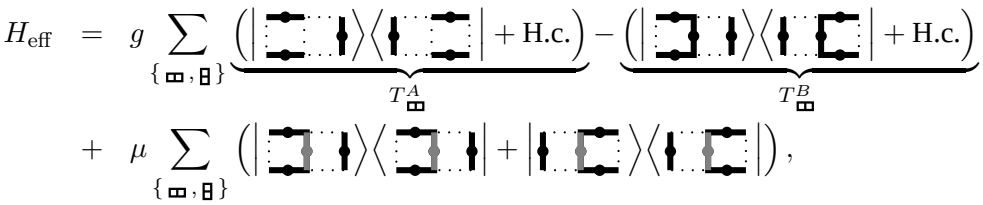

where g and μ are defined as above. The gray colored loop segments are either occupied or empty. In the following discussion, we use the gauge transformation (4.5) and obtain a matrix representation in which all off–diagonal matrix elements are non–positive. Consequently, we can write down the ground state at the RK point ($\mu = g$) as equally weighted superposition of all allowed configurations. The RK point is already well understood for bosonic quantum FPL and quantum–dimer models (QDM) [Chak 02, Shan 04, Rokh 88].

There has been strong interest in related QDM following the discovery of a topological liquid phase on a triangular lattice [Moes 01]. Let us shortly mention the main results and refer to the relevant literature. It has been established that a gapped topological phase with deconfined excitations exists in 2D for QDMs on non–bipartite lattices [Moes 01, Naya 01, Fend 02, Misg 02] while on bipartite lattices, such as a square lattice, systems typically crystallize into a phase with a broken translation/rotation symmetry. The liquid phase is "shrunk" into a single quantum critical point with gapless excitations [Rokh 88, Moes 03a, Frad 03]. In both cases, an effective gauge theory results—a $U(1)$ theory (see Chapter 5) for such a critical point and a Z_2 theory for the deconfined phase [Frad 90, Moes 02]. Several related models, such as the quantum six/eight-vertex model [Kita 03, Ardo 04, Chak 02, Shan 04] have been shown to conform to the same dichotomy: Whenever the loops can be unambiguously oriented, the model is critical (i.e., long range correlations) and is described by a $U(1)$ gauge theory. Our model differs from the conventional QDM [Rokh 88] by the FPL as well as the dynamics. Therefore, we would like to know whether a deconfined phase exists when it is extended so that it has an RK point.

The quantum dynamics of the Hamiltonian $H_{\rm eff}$ (4.3) and similarly $H_{g\mu}$ (4.8) can be described in terms of a height model [Henl 97, Herm 04] as well. The associated conserved quantities, κ_x and κ_y, as well as its insensitivity to a constant shift of the height field imply gapless hydrodynamic modes with $\omega(k) \sim k^2$ as $k \to 0$. The liquid state of the quantum FPL model at the RK point corresponds to the rough phase of the height model in which case the modes can be identified as the so-called resonons at wave vector (π, π) [Rokh 88] and the equivalent of the pi0ns (signaling the incipient crystalline order), here at $\mathbf{Q} = (0, 0)$ [Moes 04, Moes 03a, Moes 03b].

For constructing gapless excitations in our model, we adopt the single–mode approximation which has been successfully applied before to hard–core dimers on the square

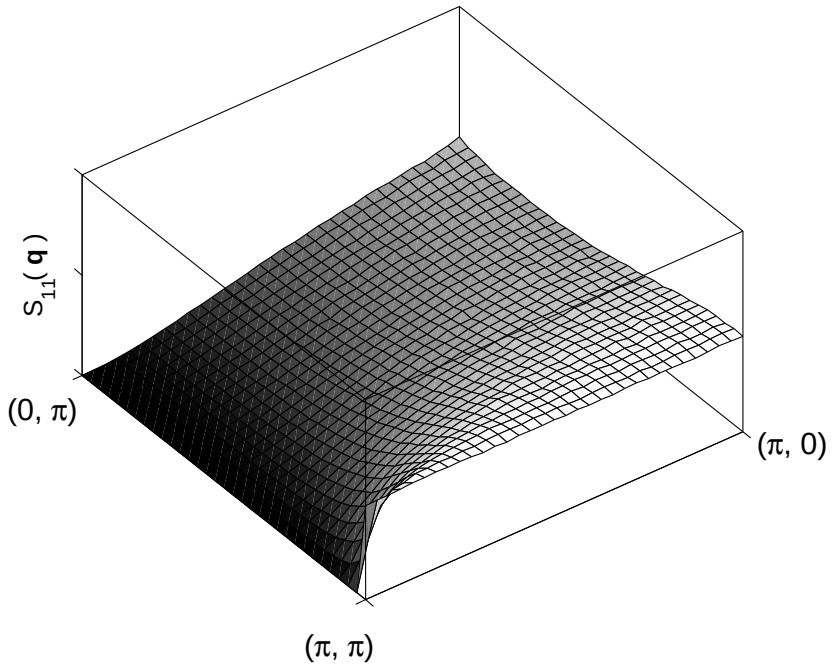

Figure 4.14: Structure factor $S_{11}(\mathbf{q})$ for the loop covering on the square lattice.

lattice [Rokh 88]. Let us denote by $|0\rangle$ the ground state at the RK point in which all configurations are contained with equal amplitude. The operator $d^+_{\hat{\tau}}(\mathbf{r})$ ($d^-_{\hat{\tau}}(\mathbf{r})$) creates (annihilates) a dimer at position $\mathbf{r} = (x, y)$ in direction $\hat{\tau}$. Here, $\hat{\tau}$ can either be in the direction of the x–axis ($\hat{\tau} = \hat{e}_1$) or y–axis ($\hat{\tau} = \hat{e}_2$). The density operator $n_{\hat{\tau}}(\mathbf{r}) = d^+_{\hat{\tau}}(\mathbf{r})d^-_{\hat{\tau}}(\mathbf{r})$ has the Fourier transform $n_{\hat{\tau}}(\mathbf{q}) = \sum_{\mathbf{r}} n_{\hat{\tau}}(\mathbf{r}) \exp(i\mathbf{q} \cdot \mathbf{r})$. We use the operators $n_{\hat{\tau}}(\mathbf{q})$ to construct the states $|\mathbf{q}, \hat{\tau}\rangle = n_{\hat{\tau}}(\mathbf{q})|0\rangle$ which are for $\mathbf{q} \neq 0$ orthogonal to $|0\rangle$. The excitation energies have an upper bound

$$E(\mathbf{q}, \hat{\tau}) \leq \frac{f(\mathbf{q})}{S_{\tau\tau}(\mathbf{q})},$$

where $\mathbf{q} = \mathbf{Q} + \mathbf{k}$ and $\mathbf{Q}$ is a reciprocal lattice vector, $f(\mathbf{q})$ is the oscillator strength and $S_{\hat{\tau}\hat{\tau}}(\mathbf{q})$ the structure factor. In order to calculate $f(\mathbf{q})$, we observe that the density operators commute with the potential energy term and thus the only contributions arise from the kinetic energy term. By using the commutation relation $[d^{+/-}_{\hat{\tau}}, n_{\hat{\tau}}] = \mp d^{+/-}_{\hat{\tau}}$ repeatedly, the contribution from the resonating terms at $\mathbf{R}$ for $\hat{\tau} = \hat{e}_1$ can be computed. The commutators needed for the calculation of the structure factor $f(\mathbf{q})$ are (lattice spacing $a = 1$):

$$[n_{\hat{e}_1}(-(\mathbf{Q}+\mathbf{k})), [-T^{A/B}_{\square}, n_{\hat{e}_1}((\mathbf{Q}+\mathbf{k}))]] = 4T^{A/B}_{\square} \times \exp(2i\mathbf{Q} \cdot \mathbf{R}) \sin^2((\mathbf{Q}+\mathbf{k}) \cdot \hat{e}_1) \quad ,$$

$$[n_{\hat{e}_1}(-(\mathbf{Q}+\mathbf{k})),[-T^{A/B}_{\square\!\square},n_{\hat{e}_1}((\mathbf{Q}+\mathbf{k}))]] = 4T^{A/B}_{\square\!\square}$$
$$\times \exp(2i\mathbf{Q}\cdot\mathbf{R})(1+\cos((\mathbf{Q}+\mathbf{k})\cdot\hat{e}_2))(1-\cos((\mathbf{Q}+\mathbf{k})\cdot\hat{e}_1)).$$

The result is that to leading order the original findings $f(\mathbf{k}) \sim (\mathbf{k}\times\hat{\tau})^2$ of [Rokh 88] are recovered in the vicinity of the $\mathbf{Q}$ points $(0,0)$, (π,π) and $(0,\pi)$.

Next, we consider the structure factor $S_{11}(\mathbf{q})$, i.e., the Fourier transform of the dimer density correlation function. Here, we make use of an asymptotic expression given in [Moes 04] ,

$$\langle n_{\hat{e}_1}(\mathbf{0})n_{\hat{e}_1}(\mathbf{r})\rangle \quad\sim\quad (-1)^{x+y}\,\Xi\,\frac{y^2-x^2}{(x^2+y^2)^2}+\frac{\Upsilon}{(x^2+y^2)^{3/2}},$$

where Ξ and Υ are constants. The structure factor is $S_{11}(\mathbf{q}) \neq 0$ except along the direction $\mathbf{q}=(q_1,\pi)$ where it vanishes with the exception of (π,π). At $(0,\pi)$ both $f(\mathbf{q})$ and $S_{11}(\mathbf{q})$ are zero. An analysis shows that the quotient of the two remains finite. The structure factor $S_{11}(\mathbf{q})$ shows no singularities. The FPL model differs here from the hard–core dimer model for which $S_{11}(\mathbf{q})$ diverges logarithmically at $\mathbf{Q}=(\pi,0)$ [Moes 03a]. The difference is due to a slower algebraic decrease with distance of the correlation function for hard–core dimer covering. We have also verified the above result for our structure factor $S_{11}(\mathbf{q})$ by means of Monte Carlo simulations, shown in Figure 4.14.

We conclude the study of the half–filled checkerboard lattice with several observations and open questions addressing the possible phase diagram of the model defined by (4.8). The bosonic version studied in [Shan 04] has three phases depending on the parameter μ/g: The two "flat" phases, i.e., the Néel phase [Shan 04] and the plaquette phase (also found in [Sylj 02, Moes 04]) as well as a maximally tilted frozen phase, with the RK point perched between the latter two phases. We have already argued that some of the flat states are actually frozen for fermions and hence cannot be used to define the fluctuation-stabilized phases for $\mu/g < 1$. The nature, and number of such phases are an open question, but let us attempt an analysis. Firstly, the maximally-flat (Néel, DDW) phase appears to be replaced by the somewhat analogous squiggle phase (Figure 6.5). In the bosonic case, the region of $-0.374 < \mu/g < 1$ corresponds to the plaquette phase, while its direct fermionic analog does not appear to be present anywhere in the fermionic phase diagram. We rule this phase out based on the fact that the squiggle phase breaks the symmetry between the numbers of fermions on different sublattices $(N_{\mathcal{B}}, N_{\mathcal{Y}}, N_{\mathcal{G}}, N_{\mathcal{R}})$, while a "fermionic plaquette" phase does not. The results of the exact diagonalization on the small samples indicate that this symmetry remains broken all the way up to $\mu/g = 1$, i.e., the RK point, with the ratio of 2/3 being consistent with the squiggle phase. This observation is also strongly disfavoring a critical liquid phase to the left of the RK point, hence the fermionic RK point in this model is likely to be an isolated quantum critical point just as it is for the bosonic model. The gapless modes identified above are in agreement with such a scenario.

4.2.2 Quarter filling

Analogously to the half–filled case, we investigate the ground–state properties of a checkerboard lattice at one–quarter filling by considering the extended effective Hamiltonian

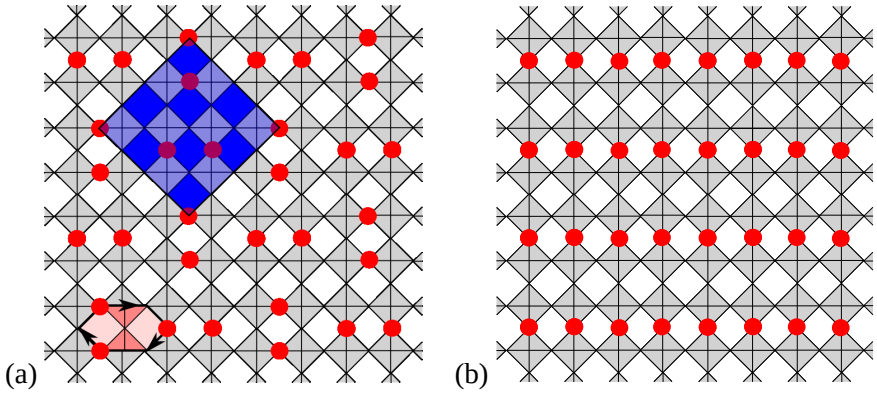

Figure 4.15: (a) One of several configurations of the quarter–filled checkerboard lattice maximizing the number of flippable hexagons. (b) Configuration with no flippable hexagons.

(4.8). For $\mu \to +\infty$, ground states are of the same nature as in the half–filled case, i.e, configurations which contain no flippable hexagons, see Figure 4.15 (b). For $\mu \to -\infty$, we find again the maximal flippable configurations to minimize the energy. Using the above described Monte Carlo algorithm, we find configurations as shown in Figure 4.15 (a) to maximize N_{fl}, which have a unit cell containing 16 sites. For a lattice with N sites, we find eight degenerate ground–state configurations with quantum numbers $(N_{\mathcal{B}}, N_{\mathcal{Y}}, N_{\mathcal{G}}, N_{\mathcal{R}})$=$(\frac{N}{4}, \frac{N}{4}, \frac{N}{4}, \frac{N}{4},)$. All are within the $(\kappa_x, \kappa_y) = (0, 0)$ sector. At $g = \mu$, we are at the RK point and find frozen and liquid–like ground states. In contrast to the half–filled case, all subensembles form a ground state with zero energy since the quarter–filled checkerboard has no fermionic sign problem.

Exact diagonalization. Now, we explore the phases for a finite range of μ values. Thereby, we find qualitatively the same phase diagram as in the previously considered half–filled case. The low–energy Hilbert space of all allowed configurations of a quarter–filled 72–site cluster has 90 176 dimensions. The two degenerate ground states $|\psi_0^{(1)}\rangle$ and $|\psi_0^{(2)}\rangle$ for $\mu < 1$ lie within the subensembles which contain configurations with the maximal number of flippable hexagons. Both are within the $(\kappa_x, \kappa_y) = (0, 0)$ sector and characterized by the quantum numbers $(N_{\mathcal{B}}, N_{\mathcal{Y}}, N_{\mathcal{G}}, N_{\mathcal{R}}) = (4, 4, 5, 5)$ and $(N_{\mathcal{B}}, N_{\mathcal{Y}}, N_{\mathcal{G}}, N_{\mathcal{R}}) = (5, 5, 4, 4)$, respectively. Because of the periodic boundary conditions and the small size, we find a modified version of the configurations to maximize the number of flippable hexagons. The absence of level crossing of ground–state energies for $\mu < g$ suggests that the system remains in a crystalline phase. However, a level crossing of the first excited states at $\mu \approx 0.9g$ might indicate a transition from the "maximal flippable" phase to a phase with a different order. At the physical point with $\mu = 0$, the system is in a crystalline and confining phase.

The lowest energies and degeneracies for $\mu = 0$ are shown in Table 4.2. The ground states within the subensembles are unique and the quantum numbers $(N_{\mathcal{B}}, N_{\mathcal{Y}}, N_{\mathcal{G}}, N_{\mathcal{R}}) = (4, 4, 5, 5)$ and $(N_{\mathcal{B}}, N_{\mathcal{Y}}, N_{\mathcal{G}}, N_{\mathcal{R}}) = (5, 5, 4, 4)$ reflect a charge order which is shown in

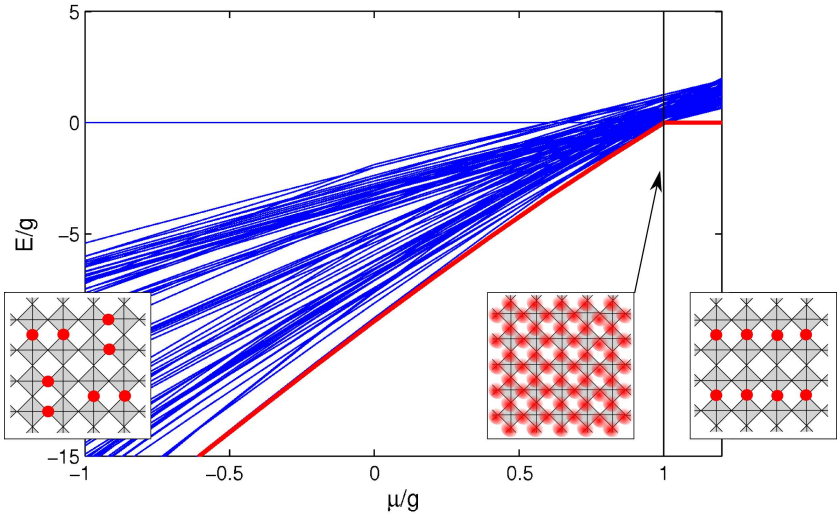

Figure 4.16: Energies of the ground state and lowest excited states in each subensemble of the $g\mu$ Hamiltonian for different values of μ at quarter filling. Level crossing of ground states occurs only at $\mu = g$. The insets indicate different phases: Maximal flippable plus fluctuations for $\mu < g$, a critical point $\mu = g$ where the ground state is an equally weighted superposition of all configurations, and isolated configurations as ground states for $\mu > g$.

	E_0	E_1	E_2	E_3
Energy / g	-9.4698	-9.1299	-8.9315	-8.9124
Degeneracy	2	2	2	2

Table 4.2: Energy spectrum and degeneracies of the effective Hamiltonian on a quarter–filled $\sqrt{72} \times \sqrt{72}$ checkerboard cluster.

Figure 4.17 (a) and (b). We find a stripe order with an average occupation of $4/9$ and $5/9$, respectively, on the alternating stripes. Figure 4.17 (c) and (d) show the density–density correlation function (4.11). As in the half–filled case, we observe qualitatively the same correlations for inequivalent sites. Furthermore, panel (f) shows the difference between the classical correlations (panel (e)) and the quantum mechanical correlations shown in panel (d).

This short numerical investigation of the quarter–filled case showed that we can expect to find qualitatively the same behavior for both filling factors. In Chapter 5, we will consider a lattice gauge–field theory for both filling factors which relates the two cases systematically.

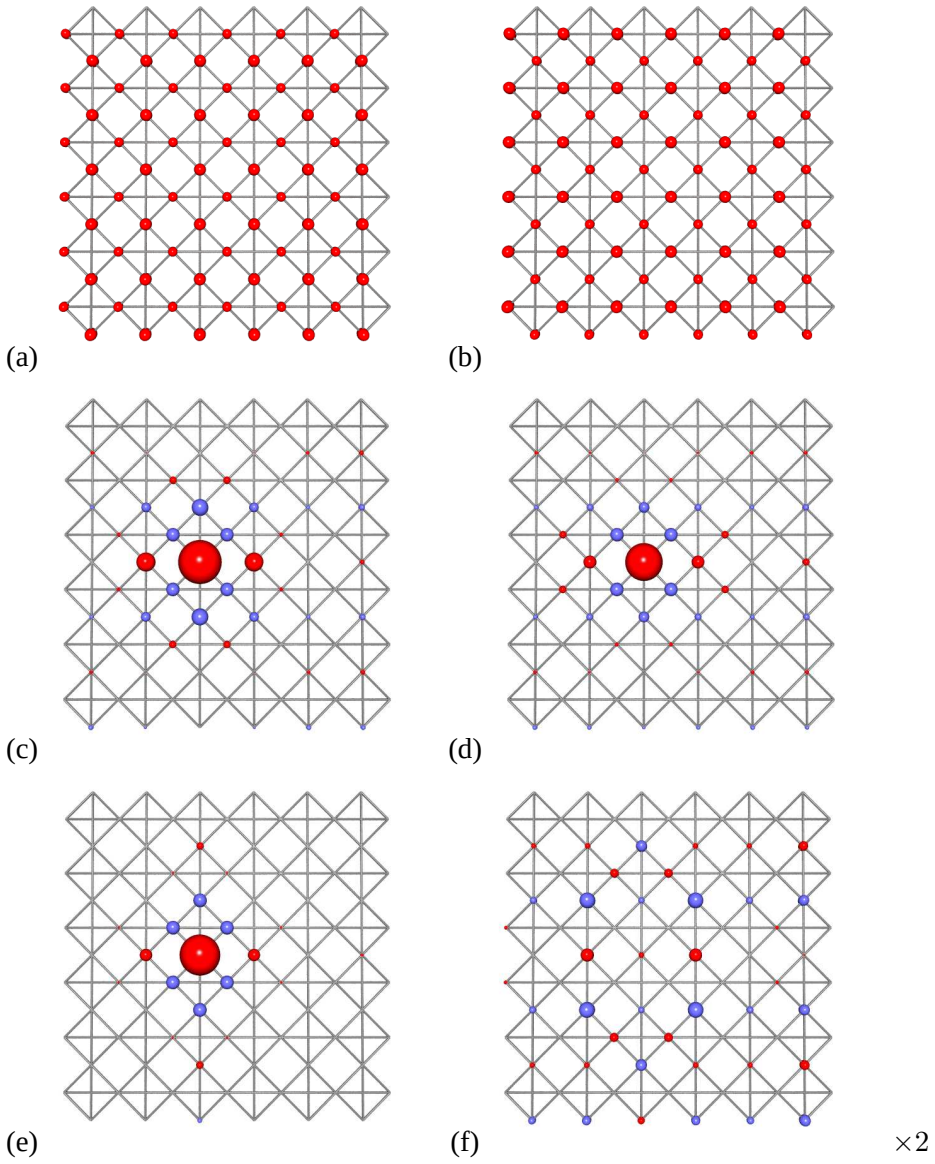

Figure 4.17: Quarter Filling: Panels (a) and (b) show the charge density distribution $\langle\psi_0^{(l)}|n_i|\psi_0^{(l)}\rangle$, while (c) and (d) show the density–density correlation function $C_{i_0 i}^{(l)}$ for the two degenerate ground states $|\psi_0^{(l)}\rangle$ with $l = 1, 2$. Panel (e) shows the classical density–density correlation function which is obtained by averaging over all allowed configurations. The radius of the dots is proportional to the absolute value. Red or blue color represents a positive or negative value, respectively. The site i_0 is chosen arbitrarily and shows up as the largest dot in the panels (c)–(e). The difference between (c) and (e) is shown in (f).

4.3 Dynamical properties

In this section, spectral functions and optical conductivity of the half–filled checkerboard lattice are presented which give insight into the dynamical properties of fcp's. One could assume that for an infinitely large system the two defects propagate freely and independently throughout the system. In that case they should be considered as two elementary excitations each having a dispersion $\tilde{\varepsilon}(\mathbf{k}) \sim t$ and each carrying the fractional charge $e/2$. It should be emphasized that they are not quasiparticles in the sense of Landau's Fermi liquid theory because they are not adiabatically connected to independent particles. Whether or not two defects actually *do* separate completely is a very subtle problem. As shown in Section 4.2.1, the presence of an ordered ground state leads to a weak confinement of fcp's with a characteristic length which depends on the ratio t/V. The following calculations show how confinement and deconfinement of fcp's becomes visible in the dynamical properties, e.g., spectral functions and optical conductivities.

4.3.1 Numerical details

Obviously, conventional approximation schemes such as mean–field theories or Green's function decoupling schemes are unable to describe the strong local correlation expressed by the tetrahedron rule. Furthermore, until now neither a creation operator formalism nor a field theoretical description for the fcp's has been derived. This suggests again numerical studies to calculate the dynamical properties. Unfortunately, the fact that we are dealing with fermions rules out the use of standard Monte–Carlo techniques. Thus, we have chosen the exact diagonalization of the Hamiltonian (2.5) for small finite lattices, even though the numerical effort increases exponentially with system size.

Diagonalization within the full Hilbert space was done for a lattice containing 18 sites. Larger systems can be considered if we restrict ourselves to certain low–energy sectors within the corresponding Hilbert spaces. They are defined by the number of violations of the tetrahedron rule. For the actual calculations, we used the smallest possible Hilbert spaces allowing for the dynamical processes that we are interested in. At half filling, they consist of the allowed configurations and those with one additional vacuum fluctuation present (one fcp and one fch). In the doped case, i.e, with one fermion added to the system, the configurations account for no other violations of the tetrahedron rule than those that are due to the added fermion (two fcp's). We refer to the space spanned by these selected configurations as the "minimal Hilbert space". The dimensions are strongly reduced as compared to the full Hilbert space (see Table 4.3). Calculations for the doped system have also been done for two other subspaces. In one case, the two–fcp's subspace is extended to three fcp's and one fch in order to check the validity of the results for the two fcp subspace. We refer to this Hilbert space as "one extra fluctuation". In the second case, we confine the two fcp's to adjacent crisscrossed squares, i.e., particles do not split in to two. Such calculations have the purpose to demonstrate that charge fractionalization leads to qualitatively different behavior.

The spectral functions and optical conductivity of interacting many–particle systems

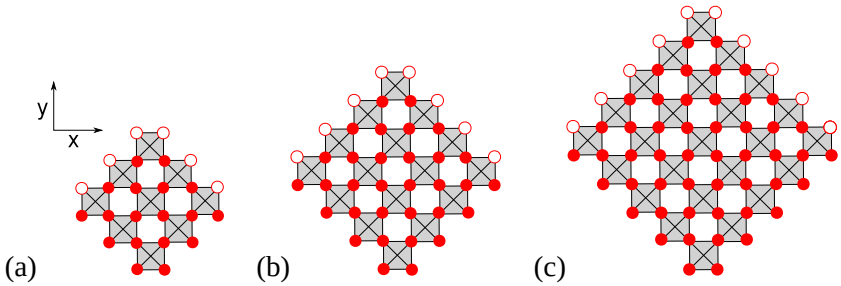

Figure 4.18: Checkerboard lattice (periodic boundary conditions are used for the calculations). Lattices with (a) 18 sites ($\sqrt{18} \times \sqrt{18}$), (b) 32 sites ($\sqrt{32} \times \sqrt{32}$) and (c) 50 sites (($\sqrt{50} \times \sqrt{50}$)) are considered.

	18 sites	32 sites	50 sites
Half filling			
Full Hilbert space	48 620	601 080 390	$1.2641\ 10^{14}$
Allowed states	68	2970	67 832
Minimal (1 fluct.)	2 228	168 858	16 178 232
System doped with one particle			
Full Hilbert space	43 758	565 722 720	$1.2155\ 10^{14}$
Minimal (0 fluct.)	1 323	98 784	8 698 450
Confined (0 fluct.)	612	47 520	1 695 800
One extra fluctuation	11 475	2 435 808	–

Table 4.3: Dimensions of the full Hilbert space and some relevant subspaces for different lattice sizes.

are expectation values of the form

$$G(z) = \langle\psi_0|A\ \frac{1}{z-H}\ A^\dagger|\psi_0\rangle \tag{4.14}$$

and can therefore conveniently be calculated numerically by the Lanczos continued fraction method [Gagl 87] or kernel polynomial expansion [Silv 96] (see Appendix B). We found essentially identical results for both algorithms. However, the implementation of the Lanczos method turned out to be slightly faster.

We rewrite first $G(z)$ as

$$G(z) = \langle\psi_0|A\ A^\dagger|\psi_0\rangle\langle\phi_0|\ \frac{1}{z-H}\ |\phi_0\rangle, \tag{4.15}$$

where

$$|\phi_0\rangle = \frac{A^\dagger|\psi_0\rangle}{\sqrt{\langle\psi_0|AA^\dagger|\psi_0\rangle}}. \tag{4.16}$$

Then the state $|\phi_0\rangle$ is taken as starting vector to generate an orthogonal basis for the Hamiltonian H (iteratively using the Lanczos algorithm). Using the tridiagonal form of the Hamiltonian with respect to the Lanczos basis and Kramers' rule, the expectation value can be easily rewritten in terms of diagonal elements a_n and off–diagonal elements b_n of the Hamiltonian in form of a continued fraction

$$G(z) = \frac{\langle\psi_0|AA^\dagger|\psi_0\rangle}{z - a_0 - b_1^2 \frac{1}{z-a_1-b_2^2\frac{1}{z-a_{2\ldots}}}}. \tag{4.17}$$

Well converged results were obtained already after several hundred iterations.

4.3.2 Results

Spectral functions. Direct insight into the dynamics of a many–body system is provided by the spectral function

$$A(\mathbf{k},\omega) = A^-(\mathbf{k},\omega) + A^+(\mathbf{k},\omega), \tag{4.18}$$

which is the probability for adding (+) or removing (–) a particle with momentum $\mathbf{k}$ and energy ω ($\hbar = 1$) to the system. The particle contribution is defined by

$$A^+(\mathbf{k},\omega) \;=\; \lim_{\eta\to 0^+} -\frac{1}{\pi}\mathrm{Im}\langle\psi_0^N|c_\mathbf{k}\,\frac{1}{\omega + i\eta + E_0 - H}\,c_\mathbf{k}^\dagger|\psi_0^N\rangle \tag{4.19}$$

and the hole contribution by

$$A^-(\mathbf{k},\omega) \;=\; \lim_{\eta\to 0^+} -\frac{1}{\pi}\mathrm{Im}\langle\psi_0^N|\,c_\mathbf{k}^\dagger\,\frac{1}{\omega + i\eta - E_0 + H}\,c_\mathbf{k}|\psi_0^N\rangle. \tag{4.20}$$

This function can be directly related to angular–resolved photoemission spectroscopy (ARPES). Here $|\psi_0^N\rangle$ is the ground state of the system with N particles. A small value of $\eta = 0.1t$ is used for Lorentzian broadening. The operators $c_\mathbf{k}$ and $c_\mathbf{k}^\dagger$ are obtained from the corresponding operators in the real–space representation

$$c_\mathbf{k}^\dagger = \frac{1}{\sqrt{N_\mathbf{k}}}\sum_j e^{i\mathbf{r}_j\mathbf{k}}c_j^\dagger, \tag{4.21}$$

where $N_\mathbf{k}$ denotes the number of $\mathbf{k}$ points in the extended (!) BZ and the sum is taken over all lattice sites. The resulting integrated spectral density is

$$D(\omega) = \frac{1}{N_\mathbf{k}}\sum_\mathbf{k} A(\mathbf{k},\omega). \tag{4.22}$$

For a system with a translationally invariant ground state or if an average over all degenerate ground states is considered, $D(\omega)$ is conveniently calculated in the real space representation as a local expectation value.

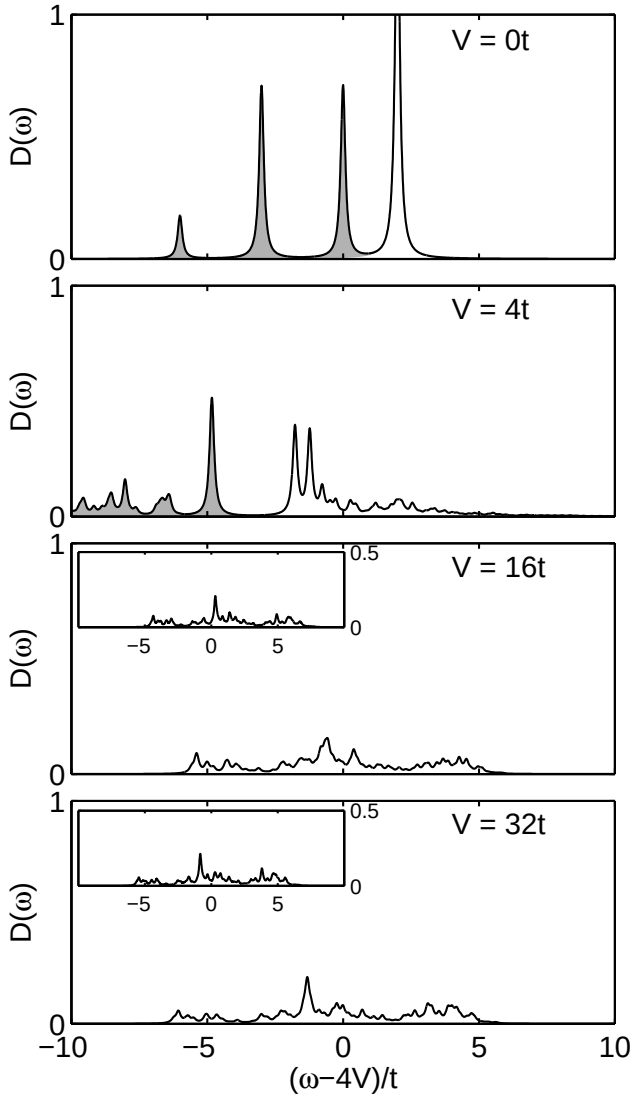

Figure 4.19: Integrated spectral density $D(\omega)$ of a half–filled $\sqrt{18} \times \sqrt{18}$ checkerboard lattice for increasing nearest–neighbor repulsion V. The contributions of $A^-(\mathbf{k}, \omega)$ is shown as shaded area. The insets show $D(\omega)$ calculated for minimal Hilbert spaces. Bandwidths and positions of the dominant features are almost unchanged. The peaks are broadened by choosing $\eta = 0.1t$.

The integrated spectral density $D(\omega)$ for the Hamiltonian (2.5) is displayed in Figure 4.19. The different values of the nearest–neighbor repulsion V show the transition from an independent–particle system to the strongly correlated limit. A rather small system is considered in order to allow for a diagonalization within the full Hilbert space with reasonable computational effort. For $V = 0$, the dispersion is given by (4.1). The integrated spectral density $D(\omega)$ includes contributions from the allowed $\mathbf{k}$–points ($\mathbf{k} = 2\pi/3\ (n_x, n_y)$ with $(n_x, n_y) \in \mathbb{Z}^2$). The dispersive band ε^- is completely filled and contributes only to $D^-(\omega)$ while the flat band is empty and contributes exclusively to $D^+(\omega)$.

Adding a particle increases the energy by $4V$. Removing it decreases the repulsion energy by $2V$. Together this leads to an increasing separation of particle and hole part of the spectrum with increasing V and finally to the formation of a gap. Thus, one expects a metal–insulator transition as a function of V. At small but finite V the peaks are broadened as an incoherent background develops. However, we are interested in the opposite limit of large V.

In the limit of large V, it is sufficient to calculate the spectral functions within the minimal Hilbert space, as seen from the good agreement with results for the full Hilbert space, shown in Figure 4.19 for parameter values $V = 16t$ and $V = 32t$. Therefore we may study much larger systems and compare results for different lattice sizes. In particular, this enables us to approach the question whether or not the two defects created by injecting one particle are closely bound to one another or not. Unfortunately, calculations on finite clusters can not distinguish between free particles and weakly bound pairs. For a first answer, we compare for different lattice sizes the results within the minimal Hilbert space with those from an artificially restricted calculation keeping the two defects confined to two adjacent crisscrossed squares. From Figure 4.20 it is seen that without the restriction a broad low–energy continuum is obtained which is missing when the restriction is imposed. The bandwidths are about $13t$ and $8t$ in the two cases. This suggests a simple interpretation. The dynamics of two separated fcp's having a bandwidth of $\approx 6t$ each due to six nearest neighbors would yield the calculated $13t$ while a confined added particle has a much smaller bandwidth, i.e., $8t$. A similar observation holds true for $A^+(\mathbf{k}, \omega)$ (see Figure 4.21) where $\mathbf{k} = (0, \pi/2)$ and $\mathbf{k} = (0, \pi)$ are considered.

One observes two interesting facts: (i) The states with large momentum $\mathbf{k}$ give the main contributions to the low–energy continuum in $D(\omega)$. This is consistent with the picture that a particle with large momentum lowers its kinetic energy more efficiently when decaying into fractional excitations than a particle with small momentum. (ii) $A^+(\mathbf{k}, \omega)$ shows in the "confined" calculation a peak–like feature at the low–energy edge that reminds one of the Landau–Fermi liquid peak while nothing alike is seen for the "free" case.

A third observation deserves a comment. For vanishing momentum, the full spectral weight of A^+ is contained in a single sharp δ–like peak near the center of the band. This suggests that $|\tilde{\psi}^{N+1}\rangle = c^\dagger_{\mathbf{k}=\mathbf{0}}|\psi_0\rangle$ is an exact eigenstate of the Hamiltonian H in the limit $t/V \to 0$ with $\tilde{H}|\tilde{\psi}^{N+1}\rangle = \tilde{E}|\tilde{\psi}^{N+1}\rangle$. This can be seen by evaluation of

$$H|\tilde{\psi}^{N+1}\rangle \quad = \quad H c^\dagger_{\mathbf{k}=\mathbf{0}}|\psi_0\rangle$$

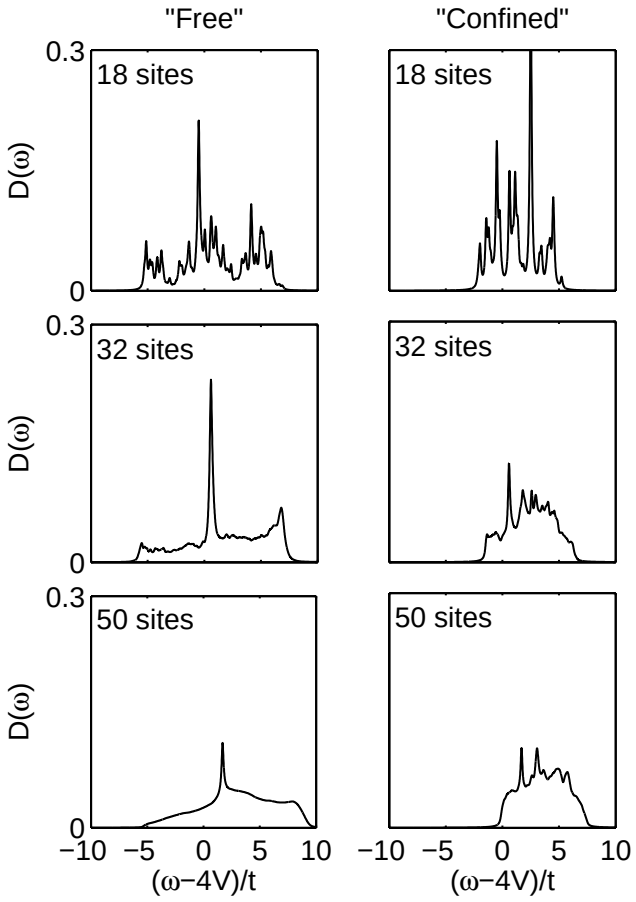

Figure 4.20: Integrated spectral density $D(\omega)$ for $V = 25t$ calculated for different lattice sizes. The left panel shows the data from "free" systems which include states with separated fractional charges. The right panel shows the data from systems where the two defects are "confined" and cannot separate. A Lorentzian broadening of $\eta = 0.1t$ is used.

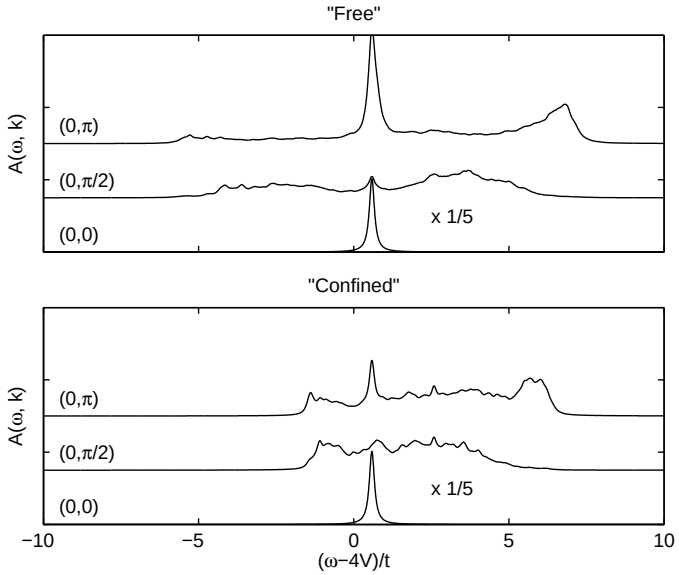

Figure 4.21: Spectral density $A(\mathbf{k},\omega)$ for $V = 25t$ calculated for some k–points. The upper panel shows data from the systems which include states with separated fractional charges. The lower panel shows the data from a system where the two defects are "confined" and can not separate. The peaks are broadened by choosing $\eta = 0.1t$.

$$\begin{aligned} &= \left[H, c^\dagger_{\mathbf{k}=\mathbf{0}}\right]|\psi_0\rangle + c^\dagger_{\mathbf{k}=\mathbf{0}} H|\psi_0\rangle \\ &= \left[H, c^\dagger_{\mathbf{k}=\mathbf{0}}\right]|\psi_0\rangle + E_0|\tilde{\psi}^{N+1}\rangle. \end{aligned} \tag{4.23}$$

The contributions of the kinetic and the repulsive energy to the commutator are given by

$$\left[H_{\rm kin}, c^\dagger_{\mathbf{k}=\mathbf{0}}\right] = \left[\sum_{\mathbf{k}'} \varepsilon(\mathbf{k}') c^\dagger_{\mathbf{k}'} c_{\mathbf{k}'}, c^\dagger_{\mathbf{k}=\mathbf{0}}\right] = \varepsilon(\mathbf{k}=\mathbf{0}) c^\dagger_{\mathbf{k}=\mathbf{0}}$$

and

$$\left[H_{\rm rep}, c^\dagger_{\mathbf{k}=\mathbf{0}}\right] = \frac{V}{\sqrt{N}} \sum_{\langle ij\rangle} \left(c^\dagger_j n_i + c^\dagger_i n_j\right), \tag{4.24}$$

respectively. The latter is calculated by using the real space representation $c^\dagger_{\mathbf{k}=\mathbf{0}} = 1/\sqrt{N}\sum_l c^\dagger_l$. Since the ground state contains in the considered limit only configurations that obey the tetrahedron rule, each empty site has exactly four occupied neighbors. Thus, the sum over all nearest neighbors applied to the ground state leads to

$$\left[H_{\rm rep.}, c^\dagger_{\mathbf{k}=\mathbf{0}}\right]|\psi_0\rangle = 4V \frac{1}{\sqrt{N}} \sum_i c^\dagger_i |\psi_0\rangle = 4V|\tilde{\psi}^{N+1}\rangle.$$

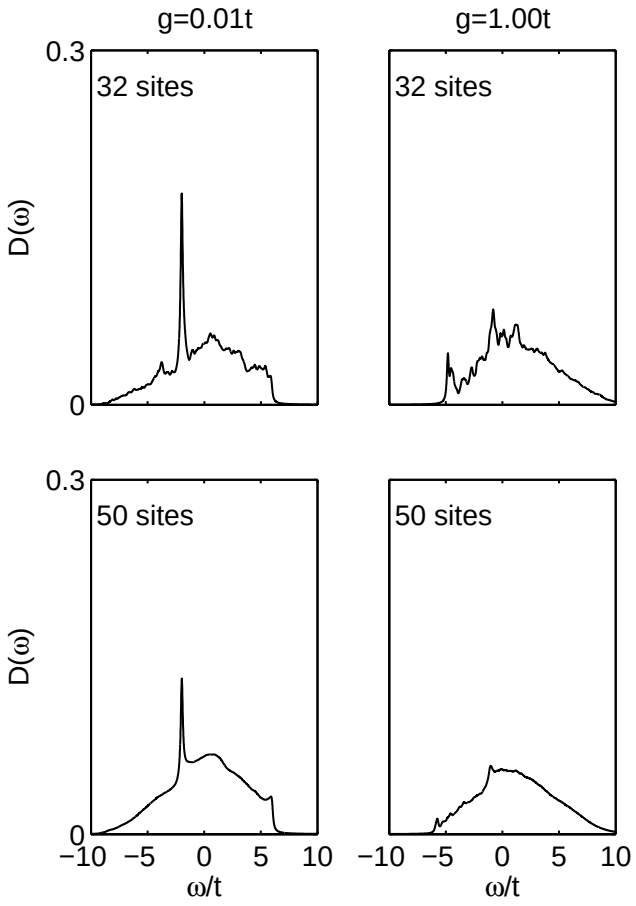

Figure 4.22: Integrated spectral density of a $\sqrt{32} \times \sqrt{32}$ cluster calculated for the effective tg Hamiltonian for two different values of g. The peaks are broadened by choosing $\eta = 0.1t$.

Collecting everything yields

$$H|\tilde{\psi}^{N+1}\rangle = (\varepsilon(\mathbf{k} = \mathbf{0}) + 4V + E_0)\,|\tilde{\psi}^{N+1}\rangle. \tag{4.25}$$

The ground–state wave function with one added particle of zero momentum is indeed an eigenfunction of the Hamiltonian with energy $\varepsilon(\mathbf{k} = \mathbf{0}) + 4V + E_0$. Note that for the doped system, no vacuum fluctuations are taken into account for this particular calculation and thus one has to add a constant energy shift from the self–energy contributions (loss of ground state correlations).

The integrated spectral density $D(\omega)$ of the effective Hamiltonian (4.7) shows a strong dependence on the ratio t/g. In the "physical" regime, corresponding to the previously considered parameters with $g \sim t^3/V^2 = 0.01t$, the integrated spectral density $D(\omega)$ (Figure 4.22) shows qualitatively the same features as the full Hamiltonian. If g is assumed to be equal to t, the broad continuum at the bottom of the spectral density vanishes and a sharp δ–peak evolves instead. Note the similarities to $D(\omega)$ for the artificially

confined situation. The spectral weight of the peak can be viewed as that of a Landau quasiparticle peak. This suggests the interpretation that the ring exchange term leads to charge order which is destroyed by the separation of the two fcp's. In the regime with $g \ll t$ ($g = t^3/V^2$) the diameter of the two bounded fcp's is larger than the system size considered and thus the excitations seem to be deconfined. An artificial increased g in the tg Hamiltonian (4.7) leads to much stronger confinement and the diameter of the bounded pair is small compared to the system size—leading to a finite weight of the quasiparticle peak. Considering the ring exchange g in the effective Hamiltonian as an independent parameter (not fixed to t^3/V^2) allows us to explore the regime where the fcp separation is small compared to the system size. These findings suggest that for parameters $V/t \approx 10$ quasiparticles with a spatial extent over more than hundred lattice sites are formed. The huge spatial extent of the quasiparticle in the "physical" regime is expected to lead to interesting effects. In particular, one could expect to find a transition from a "confining electron" phase to an "fcp plasma" phase with yet unknown properties in dependence of doping concentration. The transition would take place when the average distance of bounded fcp–fcp pairs becomes smaller than the diameter of the bound pair.

Optical Conductivity. The regular part of the optical conductivity $\sigma_{\rm reg}$ is defined by

$$\sigma_{\rm reg}(\omega) \quad = \quad \lim_{\eta\to 0^+} -\frac{1}{\omega\pi}\,{\rm Im}\langle\psi_0^N|j_{\mathbf{x}}\,\frac{1}{\omega+i\eta+E_0-H}\,j_{\mathbf{x}}|\psi_0^N\rangle. \tag{4.26}$$

Here $|\psi_0^N\rangle$ is the ground state of the system with N particles and as before we use a small $\eta = 0.1$ for broadening. The current operator is given by

$$j_{\mathbf{x}} \quad = \quad i[H,X] = it\sum_j \left(c^\dagger_{\mathbf{r}_j} c_{\mathbf{r}_j+\mathbf{x}} - c^\dagger_{\mathbf{r}_j+\mathbf{x}} c_{\mathbf{r}_j}\right).$$

Calculations have been performed for the current density along the x–axis with $\mathbf{x} = \mathbf{e}_x$. The regular part of the optical conductivity $\sigma_{\rm reg}(\omega)$ is shown in Figure 4.23 for increasing values of the nearest–neighbor repulsion V. For $V = 0$, one observes a peak–like structure. With increasing V, the structures become broader. In the half–filled (undoped) case, the complete weight is moved to larger ω and the Drude weight goes to zero. One expects a transition to an insulating state. For large V, the weight is distributed around $\omega = V$. This corresponds to the energy that is needed to generate a fcp–fch pair which carry an electrical current.

In the doped case, one finds a different behavior. Finite weight is found at $\omega = 0$ for arbitrarily large values of V and the charge is carried by two fcp's with charge $e/2$ each. A part of the weight is shifted to larger ω where additional fcp–fch pairs are generated as charge carriers. We compare the results based on the calculations in the full Hilbert space with those for the minimal Hilbert space for the case $V = 16t$. The features at small ω are reproduced very well, but in the minimal Hilbert space vacuum fluctuations are absent and thus there is no contribution to the current from fcp–fch pairs.

Next, we investigate the influence of fractional charges on the optical conductivity (see Figure 4.24). Most features are independent of lattice size. For the "free" system

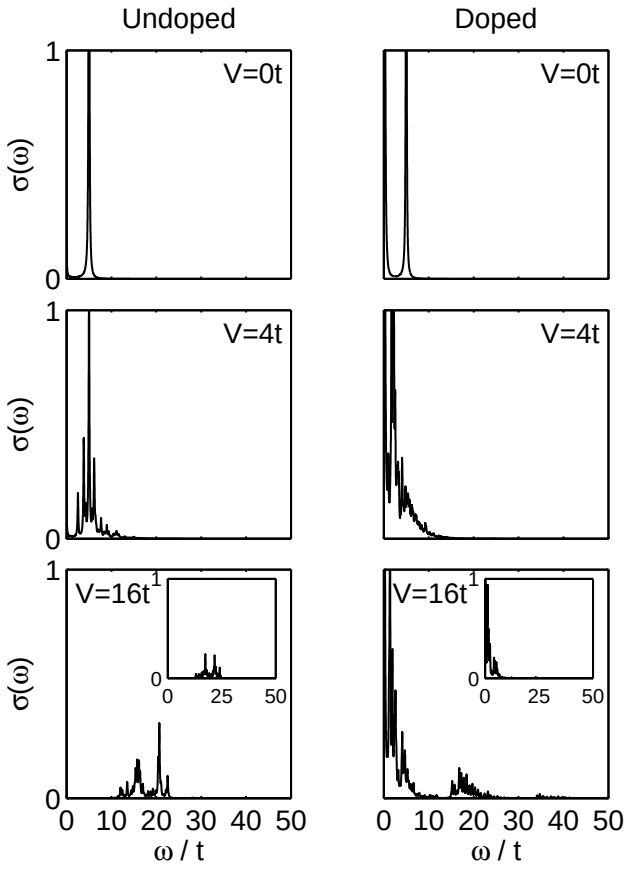

Figure 4.23: Regular part of optical conductivity $\sigma_{\rm reg}(\omega)$ of the $\sqrt{18} \times \sqrt{18}$ checkerboard lattice for increasing nearest–neighbor repulsion V. Panels on the left show the half–filled case; those on the right half filling plus one additional charge. The insets show the data for the same values within the minimal Hilbert space. The peaks are broadened by choosing $\eta = 0.1t$.

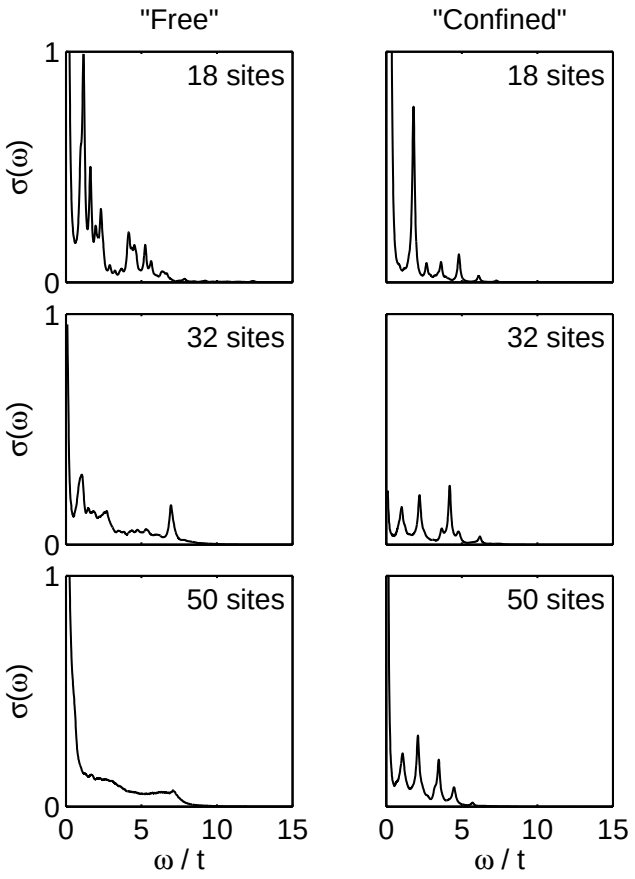

Figure 4.24: Regular part of optical conductivity $\sigma_{\rm reg}(\omega)$ for the doped system with $V = 25t$ calculated for different lattice sizes. The left panel shows the data for "free" systems which include states with separated fractional charges. The right panel shows the data for systems where the two defects are "confined" and can not separate. The peaks are broadened with $\eta = 0.1t$.

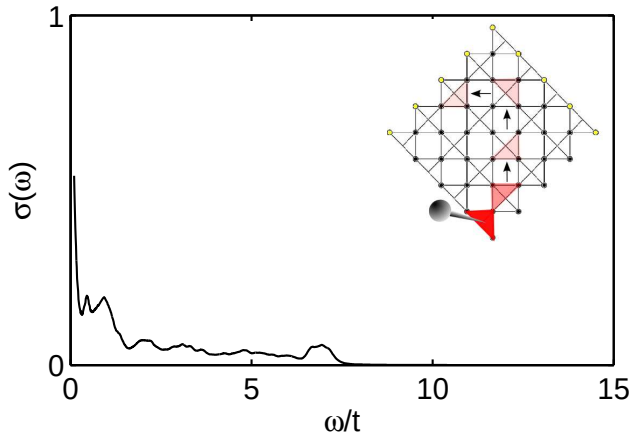

Figure 4.25: Regular part of optical conductivity $\sigma_{\mathrm{reg}}(\omega)$ for the doped system with $V = 25t$. Only one of the fractionally charged excitations is mobile while the other one is fixed. The peaks are broadened by choosing $\eta = 0.1t$. Arrows mark motions of particles.

one finds a bandwidth of nearly $13t$ which is the same as for the spectral functions. There are sharp peaks superposed onto a broad structure. The "confined" system has a reduced bandwidth of nearly $8t$ and the broad structure is less pronounced.

In Figure 4.25, the optical conductivity due to *one* moving fcp is shown. Here we keep one of the two fcp's at a fixed position and let only the other one propagate freely. One observes a Drude peak and broad structure. Except for the Drude peak no other peaks are observed. The bandwidth is reduced to about half of the bandwidth of two fcp's, as expected for the picture of one free fcp.

Chapter 5

Gauge field description of the checkerboard lattice

In the preceeding chapter, we found numerical evidence for a confining ground state of the effective model in 2D. Now we want to point out similarities to known models. In particular, we find a gauge theoretic description which is related to the compact quantum electrodynamics (compact QED) in $2+1$ dimensions based on a local $U(1)$ gauge symmetry. For a deeper understanding of the model, we perform a duality transformation and emphasize the relation to the discrete Gaussian model (DGM). We begin with the simpler case of the one–quarter filled checkerboard and derive then, analogously, the results for a the half–filled case.

5.1 Quarter filling

Here, we consider the case where one–quarter of the checkerboard–lattice sites are occupied by particles. In the limit of small t ($|t| \ll V$), the low–energy manifold can be mapped on a dimer model on a $L \times L$ square lattice, see Figure 5.1. Details of this mapping can be found in Chapter 3. The effective Hamiltonian (4.3) in the limit $|t| \ll V$ acting on the dimer representation reads

$$H_{\text{eff}} = g \sum_{\{\square,\square\}} \Big(\Big| \quad \Big\rangle\Big\langle \quad \Big| + \text{H.c.} \Big) \,, \tag{5.1}$$

with g defined as in (4.3). The terms represent hopping processes around hexagons of the original checkerboard lattice.

Each ring–exchange process can be decomposed into a product of two resonance processes around adjacent plaquettes:

$$\begin{aligned} \Big| \quad \Big\rangle\Big\langle \quad \Big| &= \Big| \quad \Big\rangle\Big\langle \quad \Big| \cdot \Big| \quad \Big\rangle\Big\langle \quad \Big| \\ \Big| \quad \Big\rangle\Big\langle \quad \Big| &= \Big| \quad \Big\rangle\Big\langle \quad \Big| \cdot \Big| \quad \Big\rangle\Big\langle \quad \Big| . \end{aligned} \tag{5.2}$$

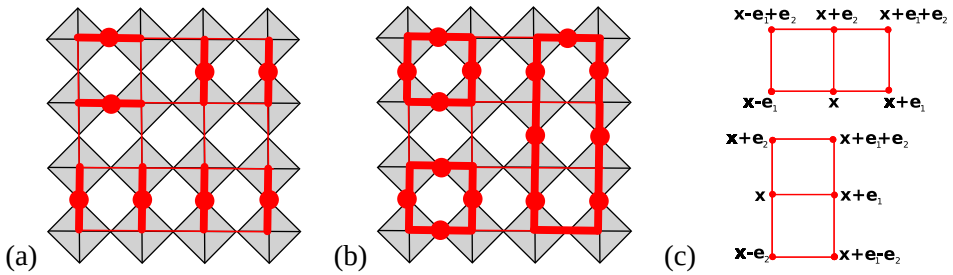

Figure 5.1: Representation of allowed configurations: (a) An example of a configuration of the quarter–filled checkerboard mapped to a dimer covering on the square lattice. (b) For the half–filled checkerboard an example configuration is mapped to a loop covering. Panel (c) shows the labeling of sites which is used for the representation of resonance terms around two adjacent plaquettes.

The problem of the quarter–filled checkerboard can now be treated in close analogy to Fradkin's ideas for the quantum dimer model (QDM) on a square lattice [Frad 90, Frad 91]. A similar approach has also been used in [Herm 04].

First, an enlarged Hilbert space on the links of the lattice is introduced. For each link $(\mathbf{x}, \mathbf{x}+\hat{e}_j)$ an integer variable $n_j(\mathbf{x}) \in [-\infty, +\infty]$ is defined, where $\mathbf{x}$ denotes the coordinates of a lattice site and $\hat{e}_{j=1,2}$ are unit vectors along the axes. The states $|\{n_j(\mathbf{x})\}\rangle$ span an enlarged Hilbert space which has arbitrary integer numbers for the links instead only zero or one. One can consider the states $|\{n_j(\mathbf{x})\}\rangle$ as eigenstates of the quantum rotor operators $\hat{n}_j(\mathbf{x})$ with eigenvalues $n_j(\mathbf{x})$. To restrict the relevant Hilbert space to states with zero or one dimer per link $[n_j(\mathbf{x}) = 0, 1]$ only, an infinite energy is attached to all unwanted states by defining the Hamiltonian

$$H_{\text{dimer}} = \lim_{U\to\infty} U \sum_{\mathbf{x}} \sum_{j=1}^{2} \left(\left(\hat{n}_j(\mathbf{x}) - \frac{1}{2} \right)^2 - \frac{1}{4} \right). \tag{5.3}$$

All configurations with $n_j(\mathbf{x}) = 0, 1$ lead to zero energy while all others have energies $U \to \infty$.

In order to express the resonance terms in the effective Hamiltonian (5.1) in terms of the operators $\hat{n}_j(\mathbf{x})$, the canonical conjugate operators $\hat{\phi}_j(\mathbf{x})$ of $\hat{n}_j(\mathbf{x})$ are introduced:

$$[\hat{\phi}_j(\mathbf{x}), \hat{n}_{j'}(\mathbf{x}')] = i\delta_{jj'}\delta_{\mathbf{x}\mathbf{x}'}. \tag{5.4}$$

Since the spectrum of $\hat{n}_j(\mathbf{x})$ is equal to the integers, the spectrum of the operator $\hat{\phi}_j(\mathbf{x})$ is a phase $\phi_j(\mathbf{x}) \in [0, 2\pi)$. Using the commutation relation (5.4) and the identity

$$\begin{aligned} e^{-im_j\hat{\phi}_j}\hat{n}_j e^{im_j\hat{\phi}_j} &= im_j \sum_{p=0}^{\infty} \frac{1}{p!} [\hat{n}_j, \hat{\phi}_j]_p \\ &= \hat{n}_j + m_j \end{aligned}$$

with the p times iterated commutator $[\hat{n}_j, \hat{\phi}_j]_p = [\hat{n}_j, [\hat{n}_j, \dots [\hat{n}_j, \hat{\phi}_j]]]$, we find that $e^{\pm i m_j \hat{\phi}_j}$ acts like a ladder operator with step size m_j:

$$\begin{aligned} \hat{n}_j e^{i m_j \hat{\phi}_j} |n_j\rangle &= e^{i m_j \hat{\phi}_j} \left(e^{-i m_j \hat{\phi}_j} \hat{n_j} e^{i m_j \hat{\phi}_j} \right) |n_j\rangle \\ &= e^{i m_j \hat{\phi}_j} \left(n_j + m_j \right) |n_j\rangle \\ &= \left(n_j + m_j \right) e^{i m_j \hat{\phi}_j} |n_j\rangle. \end{aligned} \tag{5.5}$$

It follows that $e^{i m_j \hat{\phi}_j} |n_j\rangle$ can be identified with $|n_j + m_j\rangle$. In particular, $e^{i m_j \hat{\phi}_j} |0\rangle = |m_j\rangle$.

Using the labeling as shown in Figure 5.1 (c), the Hamiltonian (5.1) expressed in terms of the ladder operators has the form

$$H_{\text{kin}} = g \sum_{\mathbf{x}} \left(T_{\square\!\square} \left(\mathbf{x} \right) + T_{\square\!\!\square} \left(\mathbf{x} \right) \right),$$

with

$$\begin{aligned} T_{\square\!\!\square} \left(\mathbf{x} \right) &= e^{i[\hat{\phi}_2(\mathbf{x}-\hat{\mathbf{e}}_2)+\hat{\phi}_2(\mathbf{x}+\hat{e}_1-\hat{e}_2)-\hat{\phi}_1(\mathbf{x}-\hat{e}_2)-\hat{\phi}_1(\mathbf{x})]} e^{i[\hat{\phi}_1(\mathbf{x}+\hat{e}_2)+\hat{\phi}_1(\mathbf{x})-\hat{\phi}_2(\mathbf{x})-\hat{\phi}_2(\mathbf{x}+\hat{e}_1)]} \\ &+ \text{H.c.} \\ T_{\square\!\square} \left(\mathbf{x} \right) &= e^{i[\hat{\phi}_1(\mathbf{x})+\hat{\phi}_1(\mathbf{x}+\hat{e}_2)-\hat{\phi}_2(\mathbf{x}+\hat{\mathbf{e}}_1)-\hat{\phi}_2(\mathbf{x})]} e^{i[\hat{\phi}_2(\mathbf{x})+\hat{\phi}_2(\mathbf{x}-\hat{e}_1)-\hat{\phi}_1(\mathbf{x}-\hat{e}_1)-\hat{\phi}_1(\mathbf{x}-\hat{e}_1+\hat{e}_2)]} \\ &+ \text{H.c.}\,. \end{aligned}$$

Here, the first product represents the hopping around two vertically oriented plaquettes and the second around horizontally oriented plaquettes. The terms are factorized as shown in (5.2). Now, the Hamiltonian that acts on the enlarged Hilbert space can be written as

$$H_{\text{eff}} = H_{\text{dimer}} + H_{\text{kin}} \tag{5.6}$$

with the constraint that each site is touched by exactly one dimer. The constraint reads

$$\hat{Q}(\mathbf{x}) |\text{Phys.}\rangle = \left(\hat{n}_1(\mathbf{x}) + \hat{n}_1(\mathbf{x} - \hat{e}_1) + \hat{n}_2(\mathbf{x}) + \hat{n}_2(\mathbf{x} - \hat{e}_2) \right) |\text{Phys.}\rangle = |\text{Phys.}\rangle. \tag{5.7}$$

Here, $|\text{Phys.}\rangle$ denotes any allowed configuration, i.e., a possible dimer covering of the square lattice, and the operators $\hat{Q}(\mathbf{x})$ count the number of dimers touching site $\mathbf{x}$. The Hamiltonian H conserves these number, i.e., $[\hat{Q}(\mathbf{x}), H] = 0$. Thus it can be diagonalized simultaneously with $\hat{Q}(\mathbf{x})$. It follows, that the operator $\hat{Q}(\mathbf{x})$ generates a set of local time–independent transformations of the form

$$\hat{U}_\alpha := e^{i \sum_{\mathbf{x}} \alpha(\mathbf{x}) \hat{Q}(\mathbf{x})}$$

which leave H unchanged. Thus, H has a local gauge symmetry and $\hat{Q}$ is the generator of local gauge transformations. The gauge symmetry reflects the fact that the phase of a valence bond can be chosen independently at each site. We will now write this result in a

more transparent form by making use of the bipartiteness of the considered square lattice. We can define staggered gauge fields $\hat{A}_j(\mathbf{x})$ and "electric fields" $\hat{E}_j(\mathbf{x})$ by

$$\begin{aligned}\hat{A}_j(\mathbf{x}) &= (-1)^{x_1+x_2}\hat{\phi}_j(\mathbf{x}),\\ \hat{E}_j(\mathbf{x}) &= (-1)^{x_1+x_2}\left(\hat{n}_j(\mathbf{x})-\frac{1}{2}\right),\end{aligned}$$

with $\mathbf{x}=(x_1,x_2)$ and write the constraint (5.7) as

$$\left[\Delta_j\hat{E}_j\left(\mathbf{x}\right)-\rho\left(\mathbf{x}\right)\right]|\text{Phys.}\rangle = 0. \tag{5.8}$$

The lattice divergence $\Delta_j\hat{E}_j\left(\mathbf{x}\right)$ is defined by

$$\Delta_j\hat{E}_j\left(\mathbf{x}\right) \equiv \underbrace{\hat{E}_1(\mathbf{x})-\hat{E}_1(\mathbf{x}-\hat{e}_1)}_{\Delta_1\hat{E}_1(\mathbf{x})}+\underbrace{\hat{E}_2(\mathbf{x})-\hat{E}_2(\mathbf{x}-\hat{e}_2)}_{\Delta_2\hat{E}_2(\mathbf{x})}$$

and the density is

$$\rho\left(\mathbf{x}\right) = (-1)^{x_1+x_2+1}.$$

The constraint that each site is touched by exactly one dimer, is now reflected by the standard Gauss' law (5.8). The background staggered charge density $\rho\left(\mathbf{x}\right)$ is either equal to $+1$ or -1. Instead we could define the electric fields as $\hat{E}_j(\mathbf{x})=(-1)^{x_1+x_2}\hat{n}_j(\mathbf{x})$. The motivation of the choice of half–integer valued electric fields becomes clear when we consider the half–filled checkerboard lattice. Using this formulation, the Hamiltonian (5.6) for a $L\times L$ lattice reads

$$\begin{aligned}H_{\text{eff}} &= \lim_{U\to\infty}U\sum_{\mathbf{x}}\sum_{j=1}^{2}\left(\hat{E}_j^2\left(\mathbf{x}\right)-\frac{1}{4}\right)\\ &\quad +2g\sum_{\mathbf{x}}\sum_{k=1}^{2}\cos\left(\sum\!\!\!\!\!\!\circlearrowleft_{\square}\hat{A}_j\left(\mathbf{x}\right)+\sum\!\!\!\!\!\!\circlearrowleft_{\square}\hat{A}_j\left(\mathbf{x}-\hat{e}_k\right)\right)\\ &= \underbrace{\lim_{U\to\infty}U\left(\sum_{\mathbf{x}}\sum_{j=1}^{2}\hat{E}_j^2\left(\mathbf{x}\right)-\frac{L^2}{2}\right)}_{H_{\text{dimer}}}\\ &\quad +2g\sum_{\mathbf{x}}\sum_{k=1}^{2}\cos\underbrace{\left(\sum\!\!\!\!\!\!\circlearrowleft_{\square}\hat{A}_j\left(\mathbf{x}\right)+\sum\!\!\!\!\!\!\circlearrowleft_{\square}\hat{A}_j\left(\mathbf{x}-\hat{e}_k\right)\right)}_{H_{\text{kin}}}.\end{aligned} \tag{5.9}$$

Here $\sum\!\!\!\!\!\!\circlearrowleft_{\square}\hat{A}_j\left(\mathbf{x}\right)$ denotes the oriented sum of staggered vector potentials $\hat{A}_j\left(\mathbf{x}\right)$ which is taken around one plaquette:

$$\begin{aligned}\sum\!\!\!\!\!\!\circlearrowleft_{\square}\hat{A}_j\left(\mathbf{x}\right) &= (-1)^{x_1+x_2}\left(\hat{\phi}_1\left(\mathbf{x}\right)+\hat{\phi}_1\left(\mathbf{x}+\hat{e}_2\right)-\hat{\phi}_2\left(\mathbf{x}\right)-\hat{\phi}_2\left(\mathbf{x}+\hat{e}_1\right)\right)\\ &= \hat{A}_1\left(\mathbf{x}\right)-\hat{A}_1\left(\mathbf{x}+\hat{e}_2\right)-\hat{A}_2\left(\mathbf{x}\right)+\hat{A}_2\left(\mathbf{x}+\hat{e}_1\right)\\ &= \Delta_2\hat{A}_1-\Delta_1\hat{A}_2.\end{aligned}$$

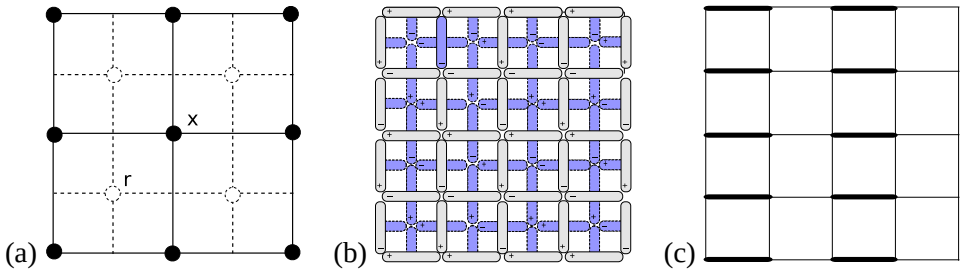

Figure 5.2: (a) Sites of the original lattice (filled circles) labeled by $\mathbf{x}$ and of the dual lattice (empty circles) labeled by $\mathbf{r}$. (b) A solution of the magnetic constraint in the sector with zero global slope and gauge $B_1(\mathbf{r}) = 0$. Links on the dual lattice are covered with blue bars representing the values of the classical fields $B_k(\mathbf{r})$ and the light gray bars the $E_j(\mathbf{x})$ field on the original lattice, having the values $\pm 1/2$. The corresponding columnar dimer state is shown by thick lines (c).

The vector $\mathbf{x}$ labels a site in between the two adjacent plaquettes, either south or west for horizontal or vertical rectangles, respectively (see Figure 5.1). Now the system can be described by Hamiltonian (5.9) acting on configurations that obey Gauss' law (5.8).

Hamiltonian (5.9) has similarities with the Hamiltonian of the compact Quantum Electrodynamic in $2 + 1$ dimensions [Poly 77]. Polyakov showed that it has a unique and gapped ground state. Two charges are confined and the energy grows linearly with the distance between them. However, our model shows important differences. The fields $E_j(\mathbf{x})$ are half integers instead of integers and the constraint selects configurations with a background charge $\rho(\mathbf{x})$. This leads to a frustration which is reflected by the macroscopic degeneracy of the classical ground states. In contrast to the model considered by Polyakov, the properties of the ground state are dominated by the quantum fluctuations even in the limit of strong coupling. In fact, for our model we expect to recover the ordered ground state which is discussed in Chapter 4. Furthermore, the cosine–term contains a sum of magnetic fluxes on two adjacent plaquettes instead of only one flux, and the kinetic energy term has a different sign. However, the latter difference can be easily removed at quarter filling by the gauge transformation presented in Chapter 4.

Duality transformation. We will gain more insight by formulating the effective Hamiltonian (5.9) in dual variables, and thereby making connection to the discrete Gaussian model and a height model [Henl 97, Kond 96b]. The constraint of having one dimer touching each site (5.8) can be solved by a classical background field and be incorporated into the Hamiltonian. First we define a dual lattice which has the sites in the center of the plaquettes of the original lattice (Figure 5.2 (a)) and label the sites with $\mathbf{r}$. In order to include the constrain (5.8) for div$E_j(\mathbf{x})$ implicitly, it is advantageous to write the electric field $E_j(\mathbf{x})$ as a sum of the curl of a fluctuating field on the sites and a classical background field on the links of the dual lattice. We define an operator $\hat{S}(\mathbf{r})$ with integer spectrum on the sites of the dual lattice and a classical half–integer valued field

$B_k(\mathbf{r}) \in \mathbb{Z} - 1/2$ on the links and demand that

$$\hat{E}_j(\mathbf{x}) = \epsilon_{jk} \left(\Delta_k \hat{S}(\mathbf{r}) + B_k(\mathbf{r}) \right). \tag{5.10}$$

Here, ϵ_{jk} is the antisymmetric Levi–Civita tensor. Indices are $j, k = 1, 2$, corresponding to the unit vectors in x– and y–direction. Inserting (5.10) into the expression for Gauss' law (5.8) yields

$$\begin{aligned} \Delta_j \hat{E}_j &= \epsilon_{jk} \left(\Delta_j \Delta_k \hat{S}(\mathbf{r}) + \Delta_j B_k(\mathbf{r}) \right) \\ &= \epsilon_{jk} \Delta_j B_k(\mathbf{r}) \\ &= \text{curl} B_k(\mathbf{r}) = \rho(\mathbf{x}). \end{aligned}$$

The first term vanishes because of the anti–symmetry of the Levi–Civita tensor and we are left with a constraint $\text{curl} B_k(\mathbf{r}) = \rho(\mathbf{x}) = (-1)^{x_1+x_2+1}$ on the background fields $B_k(\mathbf{r})$ instead of a constraint for the "electric" fields $\hat{E}_k(\mathbf{x})$. The solutions of the constraint are in one–to–one correspondence with dimer coverings on the original lattice (Figure 5.2). What we archived now is that the constraint is written in terms of the classical background fields $B_k(\mathbf{r})$.

If we take two different fields $B_k(\mathbf{r})$ and $B'_k(\mathbf{r})$, we find for the difference

$$\begin{aligned} \text{curl} \bar{B}_k(\mathbf{r}) &= \text{curl} \left(B_k(\mathbf{r}) - B'_k(\mathbf{r}) \right) \\ &= \rho(\mathbf{x}) - \rho(\mathbf{x}) \\ &= 0. \end{aligned}$$

Since the difference is curl free, it must (at least) locally be a pure gradient

$$\bar{B}_k = \Delta_k \Gamma(\mathbf{r})$$

and the local change of $B_k(\mathbf{r})$ can be absorbed in a redefinition of the operators

$$\hat{S}'(\mathbf{r}) = \hat{S}(\mathbf{r}) - \Gamma(\mathbf{r}).$$

Changes which result from large gauge transformations cannot be absorbed in a change of the operator $\hat{S}(\mathbf{r})$. These large gauge transformations correspond to a change of the global slope in terms of the height model (see Chapter 4), e.g., shifting dimers of a given covering by one site around the torus.

Now, we can solve the "magnetic" constraint by writing down a background field $B_k(\mathbf{r})$ of a certain sector. For instance, consider solutions of the constraint $\text{curl} B_k(\mathbf{r}) = \rho(\mathbf{x})$ in the sector with global slope $\kappa_x = \kappa_y = 0$. In the gauge $B_1(\mathbf{r}) = (-1)^{r_1+r_2}/2$ with $\mathbf{r} = (r_1, r_2)$, there are two different solutions of the constraint

$$B_1^{(1)}(\mathbf{r}) = \frac{(-1)^{r_1+r_2}}{2},\ B_2^{(1)}(\mathbf{r}) = \frac{(-1)^{r_2}}{2}$$

and

$$B_1^{(2)}(\mathbf{r}) \;=\; \frac{(-1)^{r_1+r_2}}{2},\; B_2^{(2)}(\mathbf{r}) = \frac{(-1)^{1+r_2}}{2}.$$

Equivalently, we can choose the gauge $B_2(\mathbf{r}) = (-1)^{r_1+r_2}/2$, leading to four configurations which correspond to columnar dimer states on the original lattice (see Figure 5.2 (b)). Thus we have solved the constraint in terms of the classical background fields. Each sector (subensemble) has a ground state. In order to write down the Hamiltonian in the dual formulation, we need the canonical conjugate operator of $\hat{S}(\mathbf{r})$ with

$$[\hat{P}(\mathbf{r}), \hat{S}(\mathbf{r}')] = i\delta_{\mathbf{r}\mathbf{r}'}.$$

Since $\hat{S}(\mathbf{r})$ has an integer spectrum, the operators $\hat{P}(\mathbf{r})$ have eigenvalues which are a phase $P(\mathbf{r}) \in [0, 2\pi)$ and we find with the same argument as in (5.5) that

$$e^{i\hat{P}(\mathbf{r})}|S\rangle = |S+1\rangle.$$

The operators $\exp\left(i \sum_{\square} \hat{A}_j(\mathbf{x})\right)$ shift the eigenvalues of $\hat{E}_j(\mathbf{x})$ by $+1$ on an oriented path around a plaquette. This increases $S(\mathbf{r})$ on the dual lattice by $+1$ and we can identify the operators

$$\sum_{\square} \hat{A}_j(\mathbf{x}) \equiv \hat{P}(\mathbf{r}).$$

In the dual formulation the Hamiltonian reads

$$\begin{aligned} H_{\text{eff}} \;=\; & \underbrace{\lim_{U\to\infty} U\left(\sum_{\mathbf{x}}\sum_{j=1}^{2}\left(\Delta_j\hat{S}(\mathbf{r}) + B_j(\mathbf{r})\right)^2 - \frac{L^2}{2}\right)}_{H_{\text{dimer}}} \\ & \underbrace{-\,2g\sum_{\mathbf{x}}\sum_{k=1}^{2}\cos\left(\hat{P}(\mathbf{r}) + \hat{P}(\mathbf{r}-\hat{e}_k)\right)}_{H_{\text{kin}}}. \end{aligned} \tag{5.11}$$

This is a frustrated version of the Discrete Gaussian Model (DGM). The frustration is created by the classical $B_j(\mathbf{r})$. For a given choice of fields $B_j(\mathbf{r})$, the classical part of the Hamiltonian has an infinite number of classical ground states. These are the possible dimer coverings of the square lattice. Note also the similarities to the model considered in [Henl 97, Isak 04].

Path integrals. It is useful to write down the Trotter expansion of the partition function of the system. It is

$$Z \;=\; \text{Tr}e^{-\beta H_{\text{eff}}}$$

where $\beta = 1/T$ and H the Hamiltonian. We split the imaginary time interval $0 \leq \tau \leq \beta$ into N_τ time steps of size d_τ and write the partition function as

$$Z = \lim_{\substack{\Delta\tau \to 0 \\ N_\tau \to \infty}} \mathrm{Tr}\left[e^{-d_\tau H_{\mathrm{eff}}}\right]^{N_\tau}.$$

By introducing an identity in terms of a complete set of eigenstates $|\{S(\mathbf{r},t)\}\rangle$ of the operators $\{\hat{S}(\mathbf{r},t)\}$ between neighboring factors, we get

$$Z = \lim_{\substack{\Delta\tau \to 0 \\ N_\tau \to \infty}} \sum_{\{S(\mathbf{r},j)\}} \prod_{j=1}^{N_\tau} \langle\{S(\mathbf{r},j)\}|e^{-d_\tau H_{\mathrm{eff}}}|\{S(\mathbf{r},j+1)\}\rangle$$

with periodic boundary conditions, i.e., $|\{S(\mathbf{r},N_\tau+1)\}\rangle = |\{S(\mathbf{r},1)\}\rangle$ and the integer j represent the jth time step. Using the fact that d_τ is small and that H_{dimer} is diagonal in the basis $|\{S(\mathbf{r},j)\}\rangle$, we can write the matrix elements as

$$\begin{aligned}\langle\{S(\mathbf{r},j)\}|e^{-d_\tau H_{\mathrm{eff}}}|\{S(\mathbf{r},j+1)\}\rangle &\approx \langle\{S(\mathbf{r},j)\}|e^{-d_\tau H_{\mathrm{kin}}}e^{-d_\tau H_{\mathrm{dimer}}}|\{S(\mathbf{r},j+1)\}\rangle \\ &= \langle\{S(\mathbf{r},j)\}|e^{-d_\tau H_{\mathrm{kin}}}|\{S(\mathbf{r},j+1)\}\rangle \\ &\quad \times e^{-d_\tau H_{\mathrm{dimer}}(\{S(\mathbf{r},j+1)\})}\end{aligned}$$

where we have taken into account only terms that are linear in d_τ. The diagonal term reads

$$H_{\mathrm{dimer}}(\{S(\mathbf{r},j)\}) = \lim_{U\to\infty} U\left(\sum_{\mathbf{r},k}\left[\Delta_k S(\mathbf{r},j) + B_k(\mathbf{r},j)\right]^2 - \frac{L^2}{2}\right).$$

The off–diagonal elements

$$\begin{aligned}&\langle\{S(\mathbf{r},j)\}|e^{-d_\tau H_{\mathrm{kin}}}|\{S(\mathbf{r},j+1)\}\rangle \\ &= \langle\{S(\mathbf{r},j)\}|e^{-d_\tau 2g\sum_{\mathbf{r}}\sum_{k=1}^{2}\cos\left(\hat{P}(\mathbf{r})+\hat{P}(\mathbf{r}-\hat{e}_k)\right)}|\{S(\mathbf{r},j+1)\}\rangle \qquad (5.12)\end{aligned}$$

are products of the form

$$\langle S(\mathbf{r},j)S(\mathbf{r}-\hat{e}_k,j)|e^{d_\tau 2J\cos\left(\hat{P}(\mathbf{r})+\hat{P}(\mathbf{r}-\hat{e}_k)\right)}|S(\mathbf{r},j+1)S(\mathbf{r}-\hat{e}_k,j+1)\rangle. \qquad (5.13)$$

They can be evaluated using the expansion

$$e^{z\cos p} = \sum_{l=-\infty}^{\infty} I_l(z)e^{ilp}, \qquad (5.14)$$

where $I_l(z)$ is the Bessel functions of order l:

$$\begin{aligned}(5.14) \quad &= \sum_{l=-\infty}^{\infty} \langle S(\mathbf{r},j)S(\mathbf{r}-\hat{e}_k,j)|e^{il\left(\hat{P}(\mathbf{r})+\hat{P}(\mathbf{r}-\hat{e}_k)\right)}|S(\mathbf{r},j+1)S(\mathbf{r}-\hat{e}_k,j+1)\rangle \\ &\quad \times I_l(2Jd_\tau) \\ &= \sum_{l=-\infty}^{\infty} I_l(2gd_\tau)\delta_{l,S(\mathbf{r},j)-S(\mathbf{r},j+1)}\delta_{l,S(\mathbf{r}-\hat{e}_k,j)-S(\mathbf{r}-\hat{e}_k,j+1)} \\ &= I_{|S(\mathbf{r},j)-S(\mathbf{r},j+1)|}(2gd_\tau)\delta_{S(\mathbf{r},j)-S(\mathbf{r},j+1),S(\mathbf{r}-\hat{e}_k,j)-S(\mathbf{r}-\hat{e}_k,j+1)} \\ &= I_{|\Delta S(\mathbf{r},j+1)|}(2gd_\tau)\delta_{\Delta_1 S(\mathbf{r},j),\Delta_1 S(\mathbf{r}-\hat{e}_k,j)}.\end{aligned}$$

Here, we use the notation

$$\Delta_0 S(\mathbf{r},j) \equiv S(\mathbf{r},j) - S(\mathbf{r},j-1)$$

for the discrete time derivative. With the approximate form

$$I_l(z) \approx \frac{e^z}{\sqrt{2\pi}} e^{-\frac{l^2}{2z}} \left(1 + O(z)\right),$$

of the Bessel functions, we find that

$$e^{2gd_\tau \cos\left(\hat{P}(\mathbf{r})+\hat{P}(\mathbf{r}-\hat{e}_k)\right)} \approx \frac{e^{2gd_\tau}}{\sqrt{2\pi}} e^{\frac{1}{4Jd_\tau}[\Delta_0 S(\mathbf{r},j)]^2} \delta_{\Delta_0 S(\mathbf{r},j),\Delta_0 S(\mathbf{r}-\hat{e}_k,j)}.$$

Thus, the partition function has the form

$$Z = \lim_{\substack{d_\tau \to 0 \\ N_\tau \to \infty}} \sum_{\{S(\mathbf{r},j)\}} e^{-\mathcal{H}_{\text{eff}}[S]} \prod_{k=1}^{2} \prod_{\mathbf{r},j} \delta_{\Delta_0 S(\mathbf{r},j),\Delta_0 S(\mathbf{r}-\hat{e}_k,j)},$$

where

$$\begin{aligned}\mathcal{H}_{\text{eff}}[S] &= \frac{1}{4gd_\tau} \sum_{\mathbf{r}j} \left[\Delta_0 S(\mathbf{r},j)\right]^2 \\ &\quad + \lim_{U\to\infty} U d_\tau \sum_{\mathbf{r}j} \sum_{k=1}^{2} \left(\left(\left[\Delta_k S(\mathbf{r},j) + B_k(\mathbf{r},j)\right]^2 \right) - \frac{L^2}{2} N_\tau \right).\end{aligned}$$

The only difference from the result obtained by Fradkin is a delta function in Z which assures that the height field changes simultaneously on two adjacent plaquettes. This indicates that our system may have similar low energy properties as the quantum dimer model on the square lattice. Furthermore, the partition function can serve as a starting point in future for a systematic study of the quarter–filled checkerboard lattice, e.g., using Monte Carlo techniques.

5.2 Half filling

In the case of half filling the low–energy manifold in the limit of small t ($|t| \ll V$) can be mapped onto a loop model on the square lattice, i.e., each site is touched by exactly two dimers (see Figure 5.1 (b)). Details of this mapping are given in Chapter 3. The effective Hamiltonian acting on the dimer representation reads in the limit $|t| \ll V$

$$H_{\text{eff}} = g \sum_{\{\square,\square\}} \Big(\Big| \quad \Big\rangle\Big\langle \quad \Big| + \text{H.c.} \Big) - g \sum_{\{\square,\square\}} \Big(\Big| \quad \Big\rangle\Big\langle \quad \Big| + \text{H.c.} \Big), \tag{5.15}$$

where g is defined as above. While in the quarter–filled case all terms in the Hamiltonian are positive, we find now ring–exchange processes with positive and negative signs. Each process can again be decomposed into a product of two resonance processes around adjacent plaquettes. Processes where the link in the middle of the two plaquettes is empty can be decomposed in the same way as in the quarter–filled case (5.2). If the link in the middle is occupied by a dimer, the process can be decomposed as

$$\Big| \quad \Big\rangle\Big\langle \quad \Big| = \Big| \quad \Big\rangle\Big\langle \quad \Big| \cdot \Big| \quad \Big\rangle\Big\langle \quad \Big|,$$
$$\Big| \quad \Big\rangle\Big\langle \quad \Big| = \Big| \quad \Big\rangle\Big\langle \quad \Big| \cdot \Big| \quad \Big\rangle\Big\langle \quad \Big|.$$

The problem of the half–filled checkerboard can now again be treated in analogy to the Quantum Dimer Model (QDM) on the square lattice. However, now we have to take care of the different signs of the two types of ring–exchange processes. First, we use the operators $\hat{n}_j(\mathbf{x})$ and its canonical conjugate $\hat{\phi}_j(\mathbf{x})$ as defined in Section 5.1 to write the effective Hamiltonian as

$$H_{\text{eff}} = H_{\text{dimer}} + H_{\text{kin}}$$

with H_{dimer} defined as in (5.3) and with

$$\begin{aligned} H_{\text{eff}} \;=\; & -g \sum_{\mathbf{x}} \Big(\sigma\left(\hat{n}_1(\mathbf{x})\right) e^{i[\hat{\phi}_1(\mathbf{x}+\hat{e}_2)+\hat{\phi}_1(\mathbf{x})-\hat{\phi}_2(\mathbf{x})-\hat{\phi}_2(\mathbf{x}+\hat{e}_1)]} \\ & \times e^{i[\hat{\phi}(\mathbf{x}-\hat{\mathbf{e}}_2)+\hat{\phi}_2(\mathbf{x}+\hat{e}_1-\hat{e}_2)-\hat{\phi}_1(\mathbf{x}-\hat{e}_2)-\hat{\phi}_1(\mathbf{x})]} \\ & + \sigma\left(\hat{n}_2(\mathbf{x})\right) e^{i[\hat{\phi}_2(\mathbf{x})+\hat{\phi}_2(\mathbf{x}-\hat{e}_1)-\hat{\phi}_1(\mathbf{x}-\hat{e}_1)-\hat{\phi}_1(\mathbf{x}-\hat{e}_1+\hat{e}_2)]} \\ & \times e^{i[\hat{\phi}_1(\mathbf{x})+\hat{\phi}_1(\mathbf{x}+\hat{e}_2)-\hat{\phi}_2(\mathbf{x}+\hat{\mathbf{e}}_1)-\hat{\phi}_2(\mathbf{x})]} + \text{H.c.} \Big). \end{aligned}$$

Here, $\sigma\left(\hat{n}_k(\mathbf{x})\right) = 2\hat{n}_k(\mathbf{x}) - 1$ denotes the sign ± 1 resulting from the occupancy of the link between the plaquettes. We find the same ring–exchange term as in the quarter–filled case, except that each term is multiplied by the term $\sigma\left(\hat{n}_k(\mathbf{x})\right)$. This additional factor gives -1 if the link is empty and $+1$ if it is occupied by a dimer.

The constraint is now that each site is touched by exactly two dimers

$$\hat{Q}(\mathbf{x})|\text{Phys.}\rangle = \frac{1}{2}\left(\hat{n}_1(\mathbf{x}) + \hat{n}_1(\mathbf{x}-\hat{e}_1) + \hat{n}_2(\mathbf{x}) + \hat{n}_2(\mathbf{x}-\hat{e}_{2the})\right)|\text{Phys.}\rangle = |\text{Phys.}\rangle.$$

We find the same local gauge symmetry as in Section 5.1, and Gauss' law can be written as

$$\left[\Delta_j \hat{E}_j\left(\mathbf{x}\right) - \rho\left(\mathbf{x}\right)\right] |\text{Phys.}\rangle = 0.$$

The background charge is now given by

$$\rho\left(\mathbf{x}\right) = 0,$$

i.e., there is no background charge. This reflects the fact that each site of the lattice is touched by exactly two dimers instead of one. Using the same notation as above, we can write the Hamiltonian as

$$\begin{aligned} H &= \underbrace{\lim_{U\to\infty} U\left(\sum_{\mathbf{x}}\sum_{j=1}^{2}\hat{E}_j^2(\mathbf{x}) - \frac{L^2}{2}\right)}_{H_{\text{dimer}}} + \\ &\quad \underbrace{-2g\sum_{\mathbf{x}}\sum_{k=1}^{2}\sigma\left(E_{3-k}(\mathbf{x})\right)\cos\left(\sum_{\square}\hat{A}_j\left(\mathbf{x}\right) + \sum_{\square}\hat{A}_j\left(\mathbf{x}-\hat{e}_k\right)\right)}_{H_{\text{kin}}}. \end{aligned}$$

Here, the oriented sums are again defined as in (5.9) and $\sigma\left(E_{3-k}(\mathbf{x})\right)$ is the sign resulting from the occupancy of the central bond. We find a coupling between the electric fields and the gauge fields resulting from the different signs of the ring–exchange processes. If we consider only the ground state and lowest excited states, we use the gauge transformation (4.5) to eliminate the relative sign between processes with occupied and empty central site. Thus, the only difference to the quarter–filled problem is a vanishing background charge $\rho(\mathbf{x})$.

Duality transformation. Again we can go to the dual formulation of the effective Hamiltonian. We introduce operators $\hat{S}(\mathbf{r})$ with integer spectrum and a classical background field $\hat{B}_k(\mathbf{r})$ which takes half–integer values on the dual lattice. The magnetic constraint becomes $\text{curl}B_k(\mathbf{r}) = \rho(\mathbf{x}) = 0$ instead. Analogous to (5.11), the Hamiltonian in dual variables reads

$$\begin{aligned} H &= \underbrace{\lim_{U\to\infty} U\left(\sum_{\mathbf{x}}\sum_{j=1}^{2}\left(\Delta_j\hat{S}(\mathbf{r}) + B_j(\mathbf{r})\right)^2 - \frac{L^2}{2}\right)}_{H_{\text{dimer}}} \\ &\quad \underbrace{+2g\sum_{\mathbf{x}}\sum_{k=1}^{2}\sigma\left(\epsilon_{3-k,l}\left(\Delta_l\hat{S}(\mathbf{r}) + B_l(\mathbf{r})\right)\right)\cos\left(\hat{P}(\mathbf{r}) + \hat{P}(\mathbf{r}-\hat{e}_k)\right)}_{H_{\text{kin}}}. \end{aligned}$$

For the lowest excited states the sign factor $\sigma\left(\epsilon_{3-k,l}\left(\Delta_l\hat{S}(\mathbf{r}) + B_l(\mathbf{r})\right)\right)$ can be neglected, leading to a similar Hamiltonian as in the quarter–filled case. The different filling

factor is now expressed by the choice of classical $B_j(\mathbf{r})$ fields. In an analogous way, we can write down the path–integral formulation.

We have achieved a systematic description of the low–energies excitations of the half–filled checkerboard. This establishes a connection between the considered charge degrees of freedom and previously studied spin systems and bosonic dimer model [Frad 91, Frad 90]. Furthermore, the derived expression in this section allow for a detailed future field theoretical work.

Chapter 6

Numerical studies of the pyrochlore lattice

The quantum–mechanical studies of a checkerboard lattice, i.e., a projection of a pyrochlore lattice onto the plane, revealed already very interesting physical effects. In particular, we found that fractionally charged excitations, which are weakly confined due to quantum fluctuations. In this chapter, we consider the pyrochlore lattice as a first true 3D example for a system which allows for fractionally charged excitations. Indications for the existence of deconfined phases have recently been found in certain spin models on pyrochlore lattices [Herm 04, Moes 03b]. Thus we find it promising to look for deconfined fractional charges on a pyrochlore lattice. We derive an effective Hamiltonian and point out similarities and differences compared with the 2D checkerboard lattice. The quantum mechanical ground state of small finite systems is calculated by means of exact diagonalization. Since the dimension of the configuration space increases exponentially with the number of sites, calculations are much more demanding in a 3D system and we are restricted to rather small systems.

6.1 Effective Hamiltonian

We start with the model Hamiltonian of spinless fermions (2.5) on the pyrochlore lattice at half filling in the regime $0 < |t| \ll V$. All configurations that obey the local constraint of having exactly two fermions on each tetrahedron are classical ground states, i.e., the tetrahedron rule is fulfilled [Ande 56]. Details about the classical limit can be found in Chapter 3.

We discuss a Hamiltonian that acts only on the Hilbert space which is spanned by allowed configurations and contains processes up to order t^3/V^2. The derivation of the effective Hamiltonian can be performed in close analogy to the previously considered effective Hamiltonian (4.3) on a checkerboard lattice: (i) Low–order processes can be classified as self–energy contributions and ring–exchange processes (see Figure 6.1). The low–energy Hamiltonian in the considered limit reads $\mathcal{H} = H_\Sigma + H_{\text{eff}}$. (ii) The diagonal part H_Σ contains the self–energy contribution resulting from processes in which a fermion

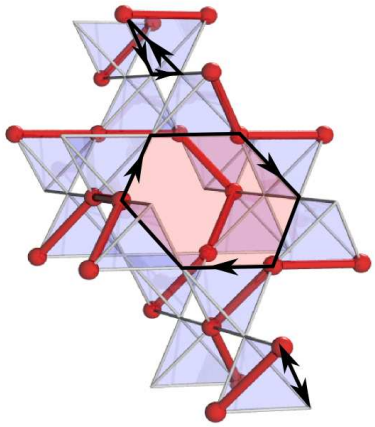

Figure 6.1: Example of an allowed configuration on the half–filled pyrochlore lattice with possible low–order hopping processes.

hops to an empty neighboring site or around an adjacent triangle and finally returns to the same site (see Figure 6.1). In all allowed configurations, the fermions have the same number of empty neighboring sites. Consequently, H_Σ leads to the same constant energy shift as in the case of the checkerboard lattice (4.2) and does not lift the macroscopic degeneracy. (iii) The macroscopic ground–state degeneracy is lifted by the lowest order of ring exchange $g = 12\,t^3/V^2$ around hexagons. The effective Hamiltonian reads

$$H_{\text{eff}} \;=\; \pm g \sum_{\{\hexagon\}} \Big(\Big| \hexagon \Big\rangle \Big\langle \hexagon \Big| + \text{H.c.} \Big)\,, \tag{6.1}$$

where the sum is taken over all hexagons. The pictographic operators represent hopping processes around hexagons and the sign of the matrix elements depends on the number of fermionic operators which have to be commuted. The hexagons lie in in the kagomé planes of the pyrochlore lattice.

6.1.1 Conserved quantities

The effective Hamiltonian conserves quantities which can be used for further classification of subensembles. Analogously to the checkerboard lattice, we can divide the sites of the pyrochlore lattice into four sublattices as shown in Figure 6.2. In Figure 6.2 (b), we recognize the similarity to the previously considered sublattices on the checkerboard lattice. The effective Hamiltonian conserves the number of fermions on each sublattice. Consequently, we can decompose the Hilbert space into sectors with fixed number of fermions on four sublattices $(N_\mathcal{B}, N_\mathcal{Y}, N_\mathcal{G}, N_\mathcal{R})$ and label those by the conserved quantum numbers. The matrix representation of the effective Hamiltonian is block–diagonal in the subensembles, where each block corresponds to a certain set of quantum numbers $(N_\mathcal{B}, N_\mathcal{Y}, N_\mathcal{G}, N_\mathcal{R})$. We can diagonalize the Hamiltonian by diagonalizing each block

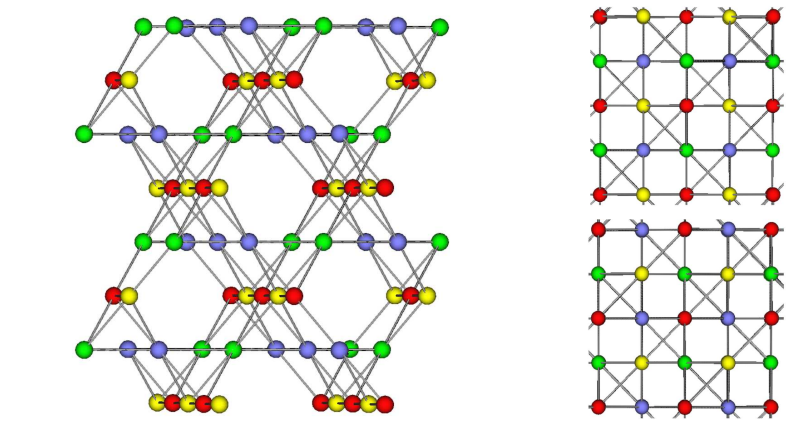

(a) (b)

Figure 6.2: Ring–exchange processes conserve the number of fermions on four sublattices (colored by red, green, blue, and yellow spheres). Panel (a) shows a perspective view and panel (b) the projections onto two different checkerboard planes.

separately and thus reduce the computational cost considerably. Furthermore, if the numbers $(N_{\mathcal{B}}, N_{\mathcal{Y}}, N_{\mathcal{G}}, N_{\mathcal{R}})$ are not equal, it implies immediately that it is more probable to find a fermion on the sublattice with larger quantum number and a charge density modulation is present. Thus, the lattice symmetry can only be preserved in a subensemble with $N_{\mathcal{B}} = N_{\mathcal{Y}} = N_{\mathcal{G}} = N_{\mathcal{R}}$.

6.1.2 Signs of Hamiltonian matrix elements

We present gauge transformations that change the sign of g in the effective Hamiltonian (6.1). This shows that the sign of g in the effective Hamiltonian (6.1) can be chosen arbitrarily ($g \leftrightarrow -g$ symmetry). Let us define a sublattice $\mathcal{P}$ that contains the purple sites of the sublattice shown in Figure 6.3. In Figure 6.3 (b) we recognize the similarity to the previously considered sublattice on the checkerboard lattice. The ring–exchange processes always change the number of fermions on this sublattice by two. We can thus change the sign of g by multiplying all configurations with a factor of

$$(-1)^{\frac{1}{2}\sum_{i\in\mathcal{P}} n_i}. \tag{6.2}$$

Here, the sum is taken over all sites of sublattice $\mathcal{P}$ and the operator n_i gives a factor one if site i is occupied and zero otherwise. Note that periodic boundary conditions can lead to violations of this rule, i.e., processes which cross the boundary might change the number of fermions on a given sublattice by values different from two, as in Chapter 4.1.2. Thus we have to choose the geometry of the considered cluster carefully in order to preserve this symmetry. In contrast to the checkerboard lattice, there is at present no local rule known to determine the sign of ring–exchange processes, and thus it is not possible to

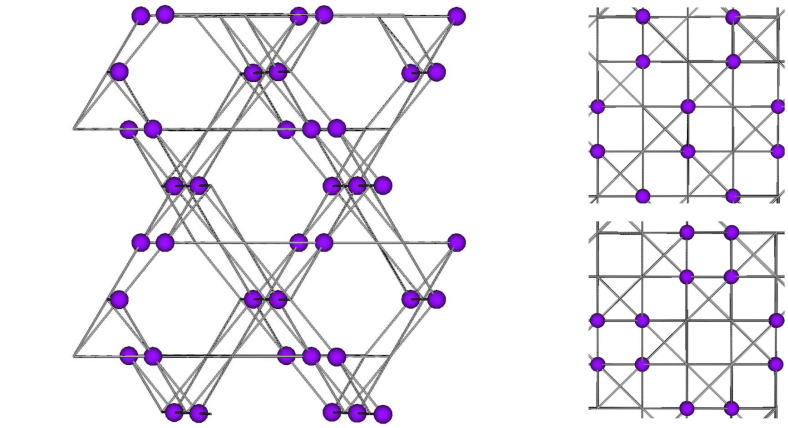

(a) (b)

Figure 6.3: Ring–exchange processes change the number of fermions on sites marked by on purple spheres by two. Panel (a) shows a perspective view and panel (b) the projections onto two different checkerboard planes.

derive a gauge transformation that removes the fermionic sign problem, i.e., the relative sign changes.

6.2 Ground state properties

For a deeper understanding of the nature of the ground state, we study a Hamiltonian which includes an extra term that counts the number of flippable hexagons, motivated by Rokshar–Kivelson [Rokh 88] as in Section 4.2.1. The number of flippable hexagons is an essential parameter to understand the effect of the kinetic energy term. The original Hamiltonian plus the extra term reads

$$H_{g\mu} = H_{\text{eff}} + \mu \sum_{\{\hexagon\}} \Big(\Big| \hexagon \Big\rangle\Big\langle \hexagon \Big| + \Big| \hexagon \Big\rangle\Big\langle \hexagon \Big| \Big) , \qquad (6.3)$$

where the pictographic operators are self explaining. In some limiting cases, we can again solve the Hamiltonian (6.3) exactly and study possible phases.

$\mu \to +\infty$: In this limit, the nature of the ground state is the same as in the case of the 2D checkerboard lattice. The ground states are all configurations which contain no flippable hexagons at all, i.e., all configurations that are not connected to any other configuration. The ground state has a gap to the first exited state which is of order μ. We can easily find configurations that have no flippable hexagons, e.g., staggered configurations. The number of different configurations that contain no flippable hexagons increases with the system size, leading to a high degeneracy of the ground states. The energy is independent

of the distance between two static fractional charges, i.e., we can find configurations that have two fcp's at arbitrary distance and contain no flippable hexagons. Consequently, the fcp's are deconfined.

$\mu \to -\infty$: Ground states are those configurations with maximal number of flippable hexagons N_{fl}. The particular order which maximizes the number of flippable hexagons has much in common with the one found for the two dimensional checkerboard lattice. For a half–filled lattice with N sites, ground–state configurations have the same quantum numbers as in the case of the checkerboard lattice: $(N_{\mathcal{B}}, N_{\mathcal{Y}}, N_{\mathcal{G}}, N_{\mathcal{R}})$ = $(2\frac{N}{20}, 2\frac{N}{20}, 3\frac{N}{20}, 3\frac{N}{20})$ and $(N_{\mathcal{B}}, N_{\mathcal{Y}}, N_{\mathcal{G}}, N_{\mathcal{R}})$ = $(3\frac{N}{20}, 3\frac{N}{20}, 2\frac{N}{20}, 2\frac{N}{20},)$ [Penc 06]. We recover the same ratio of quantum numbers $(N_{\mathcal{B}}, N_{\mathcal{Y}}, N_{\mathcal{G}}, N_{\mathcal{R}})$ as in the half–filled checkerboard lattice. Configurations with maximal number of flippable hexagons correspond to 3D squiggle configurations. Consequently, the system has in the thermodynamic limit a crystalline ground state and a gap of μ to the first excited state. If a system with periodic boundary conditions is considered and the unit cell does not fit into the cluster, modified versions of the squiggle configurations will be formed to maximize N_{fl}.

$g = \mu$: This exactly solvable point is the above described RK point (see Chapter 4). The ground states are given by an equally weighted superposition of all configurations of certain subensembles. However, the fermionic sign does not allow to construct the RK wavefunction for all subensembles.

Exact diagonalization. Now that we know the ground states of some limiting cases, we want to explore the phases for a finite range of μ values. We performed calculations on finite pyrochlore lattices with different number of sites (60, 80, as well as 108 sites) and found qualitatively the same result for all considered cluster. Here, we present the result for the 80–site cluster.

First, we generate the allowed configurations that fulfill the tetrahedron rule. Then we sort the configurations according to the quantum numbers into subensembles and generate the block–diagonal matrix representation of the Hamiltonian (6.3). From the diagonalization of block–diagonal matrices, we can finally find the ground state of the system. The actual diagonalization is done using the Lanczos algorithm, which is described in Appendix B.1. The cluster with periodic boundary conditions is chosen in such a way that (i) squiggle configurations can be formed and (ii) transformation (6.2) can be applied, i.e., the sign of g is just a matter of convention.

The low–energy Hilbert space of the 80–site cluster has $64\,523\,448$ dimensions and can be decomposed into a few hundred subensembles, where the largest one has $5\,014\,616$ dimensions. The ground states for different parameters μ provide first indications about possible phases and allow for a comparison with the results from the diagonalization of the checkerboard lattice.

Figure 6.4 shows ground–state energies for $\mu \in [0, g]$ of all subensembles. In contrast to the checkerboard lattice, we observe level crossing in the ground–state energies. In particular, we find three regimes in which the ground state has different topological

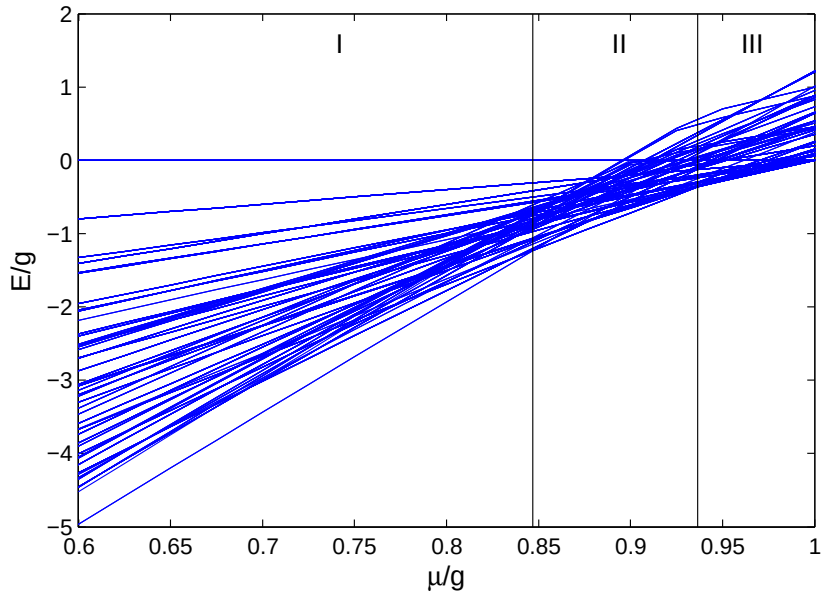

Figure 6.4: Energies of the ground states of all subensembles of the $g\mu$ Hamiltonian on the 80–site cluster for different μ–values. For $\mu < g$, we find three regimes in which different subensembles have the lowest energy (denoted by *I–III*).

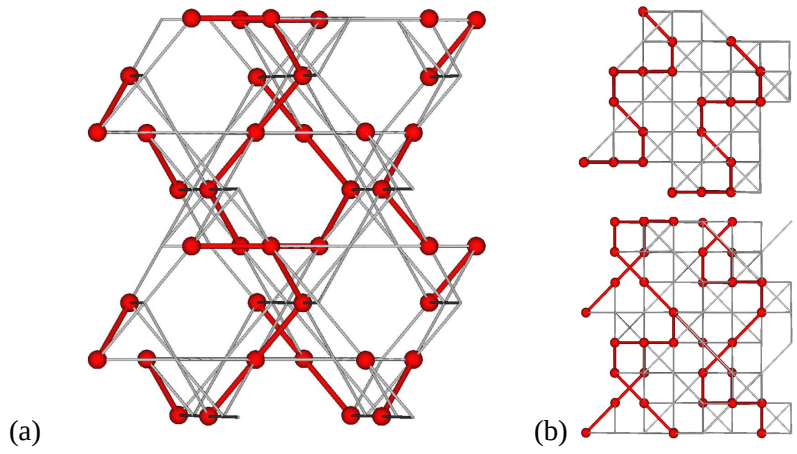

Figure 6.5: Configuration of a half–filled pyrochlore lattice with 80 sites maximizing the number of flippable hexagons, one is explicitely shown. The configuration is shown from three different perspectives. Neighboring occupied sites (dots) are connected by a solid line. Panel (a) shows a perspective view and panel (b) the projections onto two checkerboard planes.

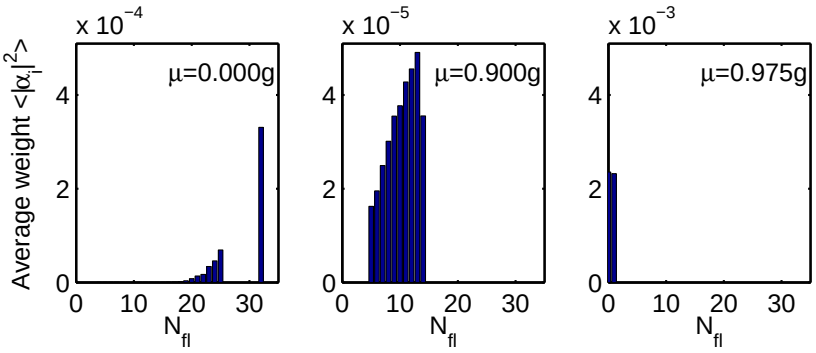

Figure 6.6: Average weight $\langle|\alpha_i|^2\rangle$ of a configuration $|c_i\rangle$ with $N_{\rm fl}$ flippable hexagons in the quantum mechanical ground states $|\psi_0^{(l)}\rangle = \sum_i \alpha_i|c_i\rangle$ of a 80 site pyrochlore cluster for different values of μ (one for each of the regimes *I*-*III*).

quantum numbers $(N_{\mathcal{B}}, N_{\mathcal{Y}}, N_{\mathcal{G}}, N_{\mathcal{R}})$. The ground states $|\psi_0^{(1)}\rangle$ and $|\psi_0^{(2)}\rangle$ in regime *I* are two–fold degenerate and have quantum numbers $(N_{\mathcal{B}}, N_{\mathcal{Y}}, N_{\mathcal{G}}, N_{\mathcal{R}}) = (8, 8, 12, 12)$ and $(N_{\mathcal{B}}, N_{\mathcal{Y}}, N_{\mathcal{G}}, N_{\mathcal{R}}) = (12, 12, 8, 8)$, respectively. The quantum numbers are the same as in the ground state in the limit $\mu \to \infty$. In fact, the subensembles with these quantum numbers contain squiggle configurations which maximize the number of flippable hexagons $N_{\rm fl}$. An example of a squiggle configuration on the pyrochlore cluster is shown in Figure 6.5. The average weight of configurations with maximal $N_{\rm fl}$ have a large weight in the ground state for small μ (see Figure 6.6). We know from the above considerations that the system for $\mu \to -\infty$ is in a crystalline state. Since the diagonalization of the finite clusters shows for $\mu < 0.85g$ no level crossings of ground states as indication for phase transitions, we expect the system in regime *I* to stay in a crystalline phase. The ground states in regime *II* and *III*, however, have a strongly reduced number of flippable hexagons (see Figure 6.6). In regime *II* ($0.85g < \mu < 0.93g$), the ground state is eight–fold degenerate with quantum numbers $(2, 14, 14, 10)$, $(10, 2, 14, 14)$, $(14, 10, 2, 14)$, $(14, 14, 10, 2)$, $(6, 6, 10, 18)$, $(6, 10, 18, 6)$, $(10, 18, 6, 6)$ and $(18, 06, 06, 10)$. Regime *III* ($0.85g < \mu < 0.93g$) has also an eight–fold degenerate ground state and contains only a few flippable hexagons. The quantum numbers are $(0, 16, 12, 12)$,$(12, 0, 16, 12)$, $(12, 12, 0, 16)$, $(16, 12, 12, 0)$, $(4, 8, 8, 20)$, $(8, 8, 20, 04)$, $(8, 20, 4, 8)$ and $(20, 4, 8, 8)$.

At $\mu = g$, we are at the RK point. The ground state is highly degenerate and formed by equally weighted superpositions of all configurations of certain subensembles. As a consequence of the fermionic signs, we observe that not all subensembles form a ground state with zero energy.

The presence of level crossing and phases with different quantum numbers might be seen as a first indication for the existence of a new phase. Various authors [Herm 04, Moes 03b] predicted a deconfined phase for a related dimer model on the pyrochlore lattice, which makes it promising to find deconfined fractional charges in 3D pyrochlore lattice.

Chapter 7

Summary and outlook

Summary. The goal of this thesis is to gain insight into a recently proposed class of models that exhibits fractionally charged excitations in 2D and 3D [Fuld 02]. In a systematic study, spinless fermions on different lattices with geometrical frustration were considered (pyrochlore, checkerboard, and kagomé lattice). The main interest is the limit in which the nearest–neighbor repulsion V is large compared with the hopping matrix element $|t|$. Here, string–like excitations with charges $\pm e/2$ attached to the ends of strings are supported for certain filling factors.

In Chapter 3, the classical limit, $t = 0$, was studied. Frustration leads in that case to a macroscopic ground–state degeneracy and all ground states can be expressed by fully–packed hard–core dimer or loop coverings. For example, the classical ground states of a half–filled checkerboard lattice were mapped on fully–packed loop coverings on a square lattice. The hard–core dimer and loop models were studied analytically and numerically. The defect–defect correlation functions for four different lattices were calculated: square, triangular, honeycomb and diamond lattices. For dimer models on 2D bipartite lattices, the correlation functions decay with increasing distance following a power law. They tend to zero for $x \to \infty$. For a non–bipartite triangular lattice, an exponential decay with increasing distance and a finite value for $x \to \infty$ was found. A 3D bipartite diamond lattice shows an exponential decay with inverse distance of defect–defect correlations and a finite value for $x \to \infty$. Analytical values for power–law exponents known in the literature, were reproduced. For the checkerboard lattice, the defect–defect correlations could be related to the solved two–color fully–packed loop model [Kond 96a, Kond 98] on a square lattice. It predicts $C(x) \sim x^{-1/3}$ which is in perfect agreement with the data from our Monte Carlo simulations. The different behavior of the defect–defect correlations leads to two different scenarios with respect to the separation of defects at finite temperatures. A separation of two defects to an infinite distance leads to an increase of the free energy. The increase is infinite for two defects on the square and honeycomb lattice (confinement) and remains finite for the triangular and diamond lattice (deconfinement).

As regards the ground state and lowest excitations for the checkerboard lattice at fixed filling (half– and quarter–filled) in the limit $|t| \ll V$, an effective Hamiltonian was studied in Chapter 4. To lowest non–vanishing order, it is given by the ring exchange

$\sim t^3/V^2$ around hexagons [Rung 04]. A non–local gauge transformation was derived for the half–filled checkerboard lattice which removes the fermionic sign problem. It was shown that the low–energy excitations of the system can equivalently be described by hard–core bosons. The possibility to avoid the fermionic sign problem allows for future application of quantum Monte Carlo simulations and the identification of exactly solvable points.

Following Rokshar and Kivelson [Rokh 88], an additional term in the Hamiltonian was introduced, which counts the number of flippable hexagons. That number is an essential parameter to understand the effect of the ring–exchange term. For some limiting cases, the ground state of the extended Hamiltonian could be obtained exactly. Starting from these exactly solvable points, we used numerical diagonalization of finite clusters, a mapping to a height model and the single–mode approximation to derive the phase diagram of the half–filled checkerboard lattice. We find a confining phase and a phase in which the ground states are given by static isolated configurations. The two phases are separated by a point with deconfined excitations, i.e., the Rokhsar–Kivelson (RK) point [Rokh 88]. The main finding is that the original effective Hamiltonian is in a confining phase with a long–range ordered ground state (squiggle phase). This phase maximizes the gain in kinetic energy and is stabilized by quantum fluctuations (order from disorder). The results of the exact diagonalization on small samples indicate that the symmetry remains broken all the way along the μ–axis up to the RK point. This observation is also strongly disfavoring a deconfining phase to the left of the RK point. Hence, the fermionic RK point is likely to be an isolated quantum critical point just as it is for the bosonic model [Shan 04]. The gapless modes identified in the height model and the single–mode approximation are in agreement with such a scenario. Numerical studies indicate that the quarter–filled checkerboard lattice has a similar phase diagram, i.e., a deconfined phase is absent.

The attractive constant force acting between two fractional charges in the confining phase results from a reduction of vacuum fluctuations and a polarization of the vacuum in the vicinity of the connecting strings. The findings suggest that a number of features known from QCD are also expected to occur in solid–state physics. Conversely, one would hope that by studying frustrated lattices or dimer models one might be able to obtain better insight into certain aspects of QCD.

Furthermore, dynamical properties of spinless fermions on checkerboard lattices were studied numerically. For the full Hamiltonian of spinless fermions, a broad low–energy continuum is found in the spectral function and no distinct quasiparticle peak is present. This confirms that an added particle decays into two fractionally charged excitations that separate over the whole finite lattice. Considering the ring–exchange constant g in the effective Hamiltonian as an independent parameter (not fixed to t^3/V^2) allowed to explore the regime where the fractionally–charged particle (fcp) separation is small compared to the system size. The spectral function for large g does not show a broad structure and develops instead a sharp peak. The existence of a "quasiparticle peak" shows that the added particle creates two bound fractionally–charged particles with a small diameter. These findings suggest that for parameters $V/t \approx 10$ quasiparticles with spatial extent over more than hundred lattice sites are formed. The large spatial extent of the bound

pairs can lead to interesting physical effects, e.g., for high doping concentrations we expect a phase transition from a confining "one electron" phase to a "fcp plasma" phase. Calculations of the optical conductivity of a single fcp showed that the bandwidth is reduced to about half of the bandwidth of two fcp's, which was expected for the picture of one free fcp.

In Chapter 5, it is shown that the considered effective Hamiltonian for the half– and quarter–filled checkerboard lattice has a local $U(1)$ gauge invariance. This invariance was used to derive a $U(1)$ lattice gauge theory and to relate the physics of fractional charges to the compact quantum electrodynamics (QED) in $2+1$ dimensions. Polyakov showed that the QED in 2+1 dimension is always confining [Poly 77]. Therefore we conclude that fractional charges on the checkerboard lattice are confined as a direct consequence of the mapping to a $U(1)$ lattice gauge theory. Furthermore, the gauge theoretic description serves as a starting point for further systematic investigations, e.g., Monte Carlo simulations.

As a step towards 3D systems, an effective Hamiltonian was derived in Chapter 6 for the half–filled pyrochlore lattice in the limit $|t| \ll V$. To lowest order the dynamics is given by ring exchange $\sim t^3/V^2$ around hexagons. The quantum–mechanical ground state of small pyrochlore clusters has been calculated by numerical diagonalization of the effective Hamiltonian. A ground state was found which shows long–range order similar to the one found for the checkerboard lattice, i.e., a 3D squiggle configuration. However, level crossing of ground–state energies from different subensembles is found when a control parameter which counts the number of flippable hexagons is varied. The presence of level crossing may indicate the existence of a deconfined phase in the vicinity of the RK point, which makes the pyrochlore lattice to a promising candite to find deconfined fractional charges in 3D.

Outlook. Based on results of this thesis, one can in the future address further questions concerning details of the physics of fractional charges on frustrated lattices. One interesting question that remains open is about the statistics of fcp's. It might be speculated that an exchange of two fcp's leads to a phase different from ± 1, i.e., bosons or fermions, respectively. However, this so–called anyonic statistics can only be realized in 2D systems. In 3D, an adiabatic exchange of particles is isomorphic to the symmetric group and thus it can lead only to bosons or fermions. Anyons have been observed for example in the fractional quantum–Hall effect. We suggest a numerical and an analytical method to determine the statistics of fcp's in our case. The suggested numerical method uses the concept of Berry phases, which can be calculated numerically, e.g., by exact diagonalization of finite clusters. The Berry phase is given by $\oint \psi_\lambda^* \, (d\psi_\lambda/d\lambda) \, d\lambda$, where λ parameterizes a closed loop and ψ_λ is the ground–state wavefunction [Berr 84]. The difficulty of this approach is the system size which needs to be considered. One needs to diagonalize very large clusters in order to obtain reliable results. An alternative analytical approach is based on an algebraic formula that relates the statistics of a lattice particle to the properties of its hopping operators [Livo 03]. There, this relation has been used to analyze emerging fermions in 3D. In particular, the statistics of the ends of string–like

excitations has been determined from the structure of the string operator. In our case, the fractional charges are placed at the ends of a string and the underlying string operators are here fermionic. Therefore, an extension of the existing analytical approach to fermionic operators would yield the statistics of fcp's on frustrated lattices.

A natural extension of the model considered in this thesis is to include spin. This would lead to a more realistic model and could provide a better link to experiments. In order to include spin, we have to enlarge the Hilbert space and to add spin interaction in addition to the nearest–neighbor repulsion. The interplay between spin and charge degrees of freedom on frustrated lattices may lead to elementary excitations with unexpected properties.

Acknowledgments

This work has been possible due to the support and assistance received by many people. It is a pleasure to express my gratefulness to them.

First of all I am sincerely grateful to my supervisors Prof. Dr. Peter Fulde and Prof. Dr. Erich Runge for introducing me to the interesting subject of my thesis, for their continuous support and for many invaluable discussions.

I also want to express my thanks to the collaborators in various projects which became part of this thesis. In particular, I owe gratitude to Dr. Joseph Betouras, Dr. Karlo Penc, Dr. Nic Shannon and Prof. Dr. Kirill Shtengel for many illuminating discussions and their contributions.

Stimulating discussions with several people helped me to gain insight into the interesting subject of frustrated systems. Special thanks are due to Prof. Dr. Claire Lhuillier, Prof. Dr. Bernoid Douçot, Dr. Grégoire Misguich and Prof. Dr. Röderich Moessner.

I have benefited from the hospitality of IDRIS (Orsay) during a stay made possible by a HPC Europe grant (RII3-CT-2003-506079). Furthermore, I am grateful for the hospitality and financial support of Université Pierre et Marie Curie (Paris) and the Instituut Lorentz (Leiden).

Last, but certainly not least, I want to express my thanks to my family and friends who supported me continously not only during the time I worked on this thesis.

Appendix A

Liouville theory

We use an effective field theory developed by Kondev to calculate the critical exponent of the defect–defect correlations. Here we present the mapping of a fully–packed loop (FPL) model to a coarse grained height field, summarize the basic ideas of the resulting field theory, and apply it to our model. For further reading, we refer to [Kond 96a, Kond 98] and citations therein.

Each configuration $\mathcal{G}$ in the fully–packed loop (FPL) model satisfies the constrain that all vertices of the lattice are visited by one loop of each flavor. A partition function involving loops with n_f different flavors and associated weights n_i is defined by

$$Z = \sum_{\mathcal{G}} \prod_{i}^{n_f} n_i^{N_i}.$$

The sum is over all configurations and N_i is the number of loops of flavor i. The classical ground states of the half–filled checkerboard lattice correspond to two–color FPL coverings on a square lattice ($n_f = 2$) with loop weights $n_1 = n_2 = n = 1$, see Figure A.1 (a). In order to obtain the Liouville theory and to calculate the critical exponents, we construct a random surface for which loops are contour lines.

The first step is to give randomly orientations to all loops. We assign the weights $\exp(\pm i\pi e)$ to the different orientations. Summing over the two possible orientations

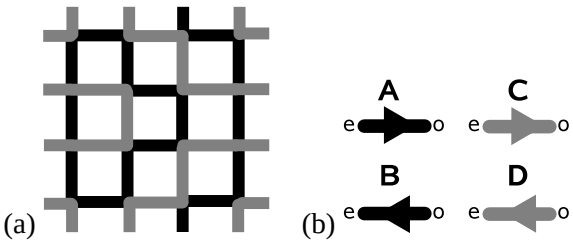

Figure A.1: Panel (a) shows one configuration of the two–color fully–packed loop model (FPL^2) on the square lattice. In (b) the mapping to the coloring model is shown where “e” and ”o” denote even and odd sites, respectively.

gives the correct loop weight $n = 2\cos(\pi e_0)$. In the considered case with $n = 1$ we find $e_0 = 1/3$. In the next step, we map the oriented loop configurations to configurations of microscopic heights $\mathbf{z} = (z_1, z_2, z_3)$ which are defined on the centers of the plaquettes. The difference between the heights on neighboring plaquettes depends on the flavor and directions of the link they share. Adopting the same convention as in [Kast 61] the differences are given by $\mathbf{A} = (-1, +1, +1)$, $\mathbf{B} = (+1, +1, -1)$, $\mathbf{C} = (-1, -1, -1)$, $\mathbf{D} = (+1, -1, +1)$, see Figure A.1 (b). The effective field theory for the coarse–grained heights is given by the action

$$\begin{aligned} S &= S_e + S_b + S_w \\ S_e &= \frac{K}{2}\int d^2\mathbf{x}\left[(\partial_1\mathbf{h})^2 + (\partial_2\mathbf{h})^2\right]\partial h^\alpha \partial h^\beta \\ S_b &= \frac{i}{4\pi}\int d^2\mathbf{x}(\mathbf{E}_0\cdot\mathbf{h})R \\ S_w &= \int d^2\mathbf{x} w(\mathbf{h}). \end{aligned}$$

Here, S_e is the elastic term (entropy of the oriented loops) with the stiffness constant K and $\mathbf{h}(\mathbf{x})$ is the height field (coarse grained field of the integer–valued height h). S_b is the boundary term with the scalar curvature $\mathcal{R}$, which vanishes everywhere except at the boundary. This term inserts the vertex operator at far ends and supplies winding loops. In the chosen normalization the electric background charge is given by $\mathbf{E}_0 = (-\pi e_0, 0, 0)$. Finally, S_w is the Liouville term. The operator $w(\mathbf{h}(\mathbf{x}))$ generates the vertex weights $\lambda(\mathbf{x})(\lambda(\mathbf{x}) = \exp(-w))$ and can be written as $w(\mathbf{h}(\mathbf{x})) = \frac{i}{16}\mathbf{E}_0\cdot\mathbf{Q}(\mathbf{x})$. The operator $\mathbf{Q}(\mathbf{x})$ is a vector–valued function of the colors around a site $\mathbf{x}$. It can be expanded in a Fourier series of vertex operators $\exp[i\mathbf{E}\cdot\mathbf{h}(\mathbf{x})]$. The vectors $\mathbf{E}$ lie in the lattice which is reciprocal to the lattice of height periods and can be seen as electrical charges. The magnetic charges form the lattice of height periods are associated with vortex configurations of the height with topological charge $\mathbf{b}$.

In the long–wavelength limit, we keep only operators with the smallest scaling dimension. The scaling dimension of a general operator with electromagnetic charge $[\mathbf{E}, \mathbf{b}]$ is given by

$$x(\mathbf{E}, \mathbf{b}) = \frac{1}{4\pi K}\mathbf{E}\cdot(\mathbf{E} - 2\mathbf{E}_0) + \frac{K}{4\pi}\mathbf{b}^2. \tag{A.0.1}$$

The topological charge $(\pm\mathbf{b})$ is $\mathbf{b} = \mathbf{C} - \mathbf{A} = (0, -2, -2)$ and $2x_{1,1}$ is the dimension of an operator with total charge $(\mathbf{E}_0, \mathbf{b})$. The stiffness constant K follows from the conformal ansatz (assumption that $w(\mathbf{h})$ is exactly marginal) and the exact value is

$$K = \frac{\pi}{4}(1 - e_0).$$

Therefore, the critical exponent of interest is simply

$$2x_{1,1} = \frac{1}{2\pi}\left(\frac{-2\pi}{3} + \frac{4\pi}{3}\right) = \frac{1}{3}. \tag{A.0.2}$$

Appendix B

Computational details

In this appendix, the numerical algorithms that have been used in this thesis are summarized. First, we discuss the Lanczos algorithm, which iteratively generates a basis in which a given Hamiltonian is tridiagonal. From the tridiagonal form, we can directly obtain the ground state and the lowest excited states. The tridiagonal form of the Hamiltonian is also used in the Lanczos recurrence method to calculate the spectral function and optical conductivity. Next, we discuss the kernel polynomial method as an alternative method to calculate the dynamical properties.

B.1 Lanczos method

The Lanczos method provides iteratively a basis in which the Hamilton operator H has a tridiagonal matrix representation. We can then obtain the eigenstates and eigenenergies from the matrix representation. Further details on the algorithm can be found in, e.g., [Golu 96].

As long as we do not have informations about the exact ground state, we choose an arbitrary initial state $|\phi_0\rangle$ to begin the iteration. Then we apply the Hamilton operator H on the state $|\phi_0\rangle$ and subtract the projection of $H|\phi_0\rangle$ onto the initial state itself. We obtain a new state

$$|\phi_1\rangle = H|\phi_0\rangle - \frac{\langle\phi_0|H|\phi_0\rangle}{\langle\phi_0|\phi_0\rangle}|\phi_0\rangle. \tag{B.1.1}$$

The new state $|\phi_1\rangle$ is orthogonal to the initial state $|\phi_0\rangle$, as can easily be seen. In the next iteration step, we construct a state that is orthogonal to $|\phi_0\rangle$ and $|\phi_1\rangle$:

$$|\phi_2\rangle = H|\phi_1\rangle - \frac{\langle\phi_1|H|\phi_1\rangle}{\langle\phi_1|\phi_1\rangle}|\phi_1\rangle - \frac{\langle\phi_1|\phi_1\rangle}{\langle\phi_0|\phi_0\rangle}|\phi_0\rangle. \tag{B.1.2}$$

Continuing this method defines recursively an orthogonal basis by

$$|\phi_{n+1}\rangle = H|\phi_n > -a_n|\phi_n\rangle - b_n^2|\phi_{n-1}\rangle, \tag{B.1.3}$$

where $n = 1, 2, \ldots$ and the coefficient are given by

$$a_n = \frac{\langle \phi_n | H | \phi_n \rangle}{\langle \phi_n | \phi_n \rangle}, \quad b_n^2 = \frac{\langle \phi_n | \phi_n \rangle}{\langle \phi_{n-1} | \phi_{n-1} \rangle}. \tag{B.1.4}$$

To begin the iteration, we choose an initial state $|\phi_0\rangle$ as well as $b_0 = 0$ and $|\phi_{-1}\rangle = 0$. During the iteration, we have to store three states, which implies a small memory requirement compared to a full diagonalization. In the basis $|\phi_n\rangle$ the operator H has the desired tridiagonal form

$$\hat{H} = \begin{bmatrix} a_0 & b_1 & 0 & 0 & \ldots \\ b_1 & a_1 & b_2 & 0 & \ldots \\ 0 & b_2 & a_2 & b_3 & \ldots \\ 0 & 0 & b_3 & a_3 & \ldots \\ \vdots & \vdots & \vdots & \vdots & \end{bmatrix}. \tag{B.1.5}$$

For a complete tridiagonalization of the matrix, the number of necessary iterations is equal to the dimension of the Hilbert space. The advantage of the Lanczos method is that we can get accurate results for the ground state and lowest excited states already after a few hundred iterations.

B.2 Lanczos recursion method

We are interested in the calculation of matrix elements of the form $\langle \phi_0 | (z \pm H)^{-1} | \phi_0 \rangle$. The inversion of large matrices, needed to calculate the matrix elements directly, is very demanding in computational time and memory consumption. Here we consider an alternative approach which uses a tridiagonal representation of the Hamiltonian to calculate the designated matrix elements [Dago 94, Fuld 95, Pett 85]. From the tridiagonal form $\hat{H}$ of the Hamilton operator H, we can obtain the matrix element by solving an inhomogeneous linear equation system. Therefore, the tridiagonal matrix $(z \pm \hat{H})$ and the identity

$$\sum_n (z \pm H)_{mn} (z \pm H)^{-1}_{np} = \delta_{mp}$$

are introduced. The vector $x_n = (z \pm H)^{-1}_{n1}$ fulfills the equation

$$\sum_n (z \pm H)_{mn} x_n = \delta_{1m} = e_m, \tag{B.2.6}$$

where e_m denotes the m'th unit vector. With this definition the first component x_1 of the vector corresponds to the expectation value $\langle \phi_0 | \frac{1}{z \pm H} | \phi_0 \rangle$. The equation system (B.2.6) can now be solved with Cramer's rule.

Define the matrix $\hat{A}$ with the matrix elements

$$A_{mn} = (z \pm H)_{mn} (1 - \delta_{n1}) + e_m \delta_{n1}.$$

Following Cramer's rule, the solution of (B.2.6) for x_1 is given by

$$x_1 = \frac{\det \hat{A}}{\det (z \pm \hat{H})}. \tag{B.2.7}$$

The matrix representations of the two matrices in the Lanczos basis $\{|\phi_n\rangle\}$ of $\hat{H}$ have the following form

$$z \pm \hat{H} = \begin{bmatrix} z \pm a_0 & \pm b_1 & 0 & 0 & \dots \\ \pm b_1 & z \pm a_1 & \pm b_2 & 0 & \dots \\ 0 & \pm b_2 & z \pm a_2 & \pm b_3 & \dots \\ 0 & 0 & \pm b_3 & z \pm a_3 & \dots \\ \vdots & \vdots & \vdots & \vdots & \end{bmatrix} \tag{B.2.8}$$

and

$$\hat{A} = \begin{bmatrix} 1 & \pm b_1 & 0 & 0 & \dots \\ 0 & z \pm a_1 & \pm b_2 & 0 & \dots \\ 0 & \pm b_2 & z \pm a_2 & \pm b_3 & \dots \\ 0 & 0 & \pm b_3 & z \pm a_3 & \dots \\ \vdots & \vdots & \vdots & \vdots & \end{bmatrix}. \tag{B.2.9}$$

The determinants in (B.2.7) can be expanded using the tridiagonality of the matrices (B.2.8) and (B.2.9), such that $\det(z \pm \hat{H}) = (z \pm a_0)\, \hat{D}_1 - b_1^2\, \hat{D}_2$ and $\det(A) = \hat{D}_1$. This leads to

$$x_1 = \frac{1}{z \pm a_0 - b_1^2 \frac{\det \hat{D}_2}{\det \hat{D}_1}}.$$

The matrices $\hat{D}_n$ are obtained by removing the first n rows and columns of the matrix $z - \hat{H}$. Decomposition of $\det \hat{D}_1$ and $\det \hat{D}_2$ gives

$$\frac{\det \hat{D}_2}{\det \hat{D}_1} = \frac{1}{z \pm a_1 - b_2^2 \frac{\det \hat{D}_3}{\det \hat{D}_4}}.$$

This decomposition can be continued until the matrices are completely decomposed. One gets a continued fraction as solution of the equation system

$$x_1 = \frac{1}{z \pm a_0 - b_1^2 \frac{1}{z - a_1 - b_2^2 \frac{1}{z - a_{2 \dots}}}}. \tag{B.2.10}$$

This expression is used to calculate matrix elements of the form $\langle \phi_0 | (z \pm H)^{-1} | \phi_0 \rangle$ as a continued fraction in terms of the Lanczos tridiagonal–matrix elements.

Green's functions and spectral functions. The Green's function $G_{k,e}(\omega)$ of a cluster is given by

$$G_{k,e}(\omega) = \langle\psi_0|c_k \frac{1}{z-H} c_k^\dagger|\psi_0\rangle,\ z = (\omega + i\eta + E_0).$$

Rewriting the expectation value as

$$G_{k,e}(\omega) = \langle\psi_0|c_k c_k^\dagger|\psi_0\rangle\langle\phi_0|\frac{1}{z-H}|\phi_0\rangle,$$

in terms of

$$|\phi_0\rangle = \frac{c_k^\dagger|\psi_0\rangle}{\sqrt{\langle\psi_0|c_k c_k^\dagger|\psi_0\rangle}}.$$

reads with (B.2.10)

$$G_{k,e}(\omega) = \frac{\langle\psi_0|c_k c_k^\dagger|\psi_0\rangle}{z - a_0 - b_1^2 \frac{1}{z-a_1-b_2^2\frac{1}{z-a_{2\cdots}}}},\ z = (\omega + i\eta + E_0).$$

Using this method with the initial state $|\phi_0\rangle = c_k|\psi_0\rangle/\langle\psi_0|c_k^\dagger c_k|\psi_0\rangle$ and the operator $\frac{1}{z+H}$, one gets the Green's function for the hole propagation as

$$G_{k,h}(\omega) = \frac{\langle\psi_0|c_k^\dagger c_k|\psi_0\rangle}{z + a_0 - b_1^2 \frac{1}{z+a_1-b_2^2\frac{1}{z+a_{2\cdots}}}},\ z = \omega + i\eta - E_0.$$

The Green's function can then be used to calculate the spectral density

$$A_k(\omega) = -\frac{1}{\pi}\lim_{\eta\to 0^+} \mathrm{Im}\left(G_{k,e}(\omega) + G_{k,h}(\omega)\right).$$

Optical conductivity. The optical conductivity σ is defined by

$$\sigma_{\mathbf{x}}(\omega) = -\frac{1}{\omega\pi}\mathrm{Im}\langle\psi_0|j_{\mathbf{x}} \frac{1}{z-H} j_{\mathbf{x}}|\psi_0\rangle, \quad z = (\omega + i\eta + E_0),$$

where

$$j_{\mathbf{x}} = it\sum_{\mathbf{r}}\left(c_{\mathbf{r}}^\dagger c_{\mathbf{r}+\mathbf{x}} - c_{\mathbf{r}+\mathbf{x}}^\dagger c_{\mathbf{r}}\right).$$

The expectation value is rewritten

$$\sigma_x(\omega) = -\frac{1}{\omega\pi}\mathrm{Im}\left(\langle\psi_0|j_{\mathbf{x}} j_{\mathbf{x}}|\psi_0\rangle\langle\phi_0|\frac{1}{z-H}|\phi_0\rangle\right),$$

with

$$|\phi_0\rangle = \frac{j_{\mathbf{x}}|\psi_0\rangle}{\sqrt{\langle\psi_0|j_{\mathbf{x}} j_{\mathbf{x}}|\psi_0\rangle}}.$$

It follows with (B.2.10) that

$$\sigma_x(\omega) = -\frac{1}{\omega\pi}\mathrm{Im}\left(\frac{\langle\psi_0|j_{\mathbf{x}} j_{\mathbf{x}}|\psi_0\rangle}{z - a_0 - b_1^2 \frac{1}{z-a_1-b_2^2\frac{1}{z-a_{2\cdots}}}}\right).$$

B.3 Kernel Polynomial Approximation

An alternative numerical method to calculate spectral functions and optical conductivity is the Kernel Polynomial Approximation (KPA), which uses a Chebyshev expansion [Silv 94, Silv 96, Silv 97, Weis 04]. We want to calculate the spectral function of an operator O:

$$\begin{aligned} A^O(\omega) &= -\frac{1}{\pi}\lim_{\eta\to 0^+}\mathrm{Im}\left(\langle\psi_0|O^\dagger\frac{1}{\omega+i\eta+E_0-H}O|\psi_0\rangle\right) \\ &= \sum_{n=1}^{N}|\langle\psi_0|O|\psi_n\rangle|^2\delta(\omega-\omega_n). \end{aligned} \tag{B.3.11}$$

First, the Hamiltonian and energies are rescaled $H \to X$ and $\omega \to x$, such that the energies x lie in $[-1,1]$. The δ-function in (B.3.11) can then be approximated by a kernel polynomial

$$\begin{aligned} A_K^O(x) &\approx \langle\psi_0|O^\dagger K(x,X)O|\psi_0\rangle \\ &= \frac{1}{\pi\sqrt{1-x^2}}\left(g_o\mu_0^O + 2\sum_{m=1}^{M} g_m T_m(x)\mu_m^O\right), \end{aligned} \tag{B.3.12}$$

with Chebyshev moments for the operator O

$$\mu_m^O = \langle\psi_0|O^\dagger T_m(X)O|\psi_0\rangle. \tag{B.3.13}$$

The calculated function corresponds to the convolution of the real spectral function and the kernel polynomial g_m. With increasing number of moments M the KPM spectral function $A_K^O(x)$ converges in a controlled manner to the desired spectral function $A^O(x)$.

The expression (B.3.12) is evaluated as follows. First $O|\psi_0\rangle$ is calculated and then the vectors $T_m(X)O|\psi_0\rangle$ are obtained from the Chebyshev recurrence relations

$$\begin{aligned} T_0(X)O|\psi_0\rangle &= 1 \\ T_1(X)O|\psi_0\rangle &= O|\psi_0\rangle \\ T_{m\geq 2}(X)O|\psi_0\rangle &= 2XT_{m-1}(X)O|\psi_0\rangle - T_{m-2}(X)O|\psi_0\rangle. \end{aligned}$$

The moments are constructed using

$$\begin{aligned} \mu_{2m} &= 2\langle\psi_0|O^\dagger T_m(X)T_m(X)O|\psi_0\rangle - 1 \\ \mu_{2m-1} &= 2\langle\psi_0|O^\dagger T_m(X)T_{m-1}(X)O|\psi_0\rangle - \langle\psi_0|O^\dagger T_1(X)O|\psi_0\rangle. \end{aligned}$$

We use the so–called Jackson kernel g_m to avoid Gibbs oscillations due to the cut off [Silv 96].

The spectral function $A_{k,e}(\omega)$ of a cluster can be obtained from the rescaled spectral function $A_{k,e}(x)$. It can be evaluated via expressions (B.3.12) and (B.3.13) with $O = c_k^\dagger$. Equivalentely, the optical conductivity $\sigma_{\mathrm{reg}}(\omega)$ of a cluster can be obtained from the rescaled optical conductivity $\sigma_{\mathrm{reg}}(x)$ using expressions (B.3.12) and (B.3.13) with $O = j_{\mathbf{x}}$.

Bibliography

[Ande 56] P. W. Anderson. “Ordering and Antiferromagnetism in Ferrites”. *Phys. Rev.*, Vol. 102, p. 1008, May 1956. 10, 71

[Ande 73] P. W. Anderson. “Resonating valence bonds: a new kind of insulator?”. *Mater. Res. Bull.*, Vol. 8, p. 173, 1973. 33

[Ardo 04] E. Ardonne, P. Fendley, and E. Fradkin. “Topological Order and Conformal Quantum Critical Points”. *Ann. Phys*, Vol. 310, pp. 493–551, 2004. 40

[Bark 98] G. Barkema and M. Newman. “Monte Carlo simulation of ice models”. *Phys. Rev. E*, Vol. 57, p. 115, 1998. 16, 31

[Baxt 82] R. Baxter. *Exactly Solved Models in Statistical Mechanics*. Academic, San Diego, 1982. 10

[Berr 84] M. V. Berry. “Quantal Phase Factors Accompanying Adiabatic Changes”. *Proc. Roy. Soc. London*, Vol. 392, p. 45, 1984. 81

[Bone 02] N. E. Bonesteel and L. P. Gor’kov. *Selected Papers of J. Robert Schrieffer*. Vol. 30 of *World scientific series in 20th century physics*, World Scientific, Singapur, 2002. 5

[Chak 02] S. Chakravarty. “Theory of the d-density wave from a vertex model and its implications”. *Phys. Rev. B*, Vol. 66, p. 224505, 2002. 40

[Dago 94] E. Dagotto. “Correlated electrons in high-temperature superconductors”. *Rev. Mod. Phys.*, Vol. 66, p. 763, 1994. 88

[Diep 05] H. T. Diep, Ed. *Frustrated Spin Systems*. World Scientific, Singapore, 2005. 2, 16

[Fend 02] P. Fendley, R. Moessner, and S. Sondhi. “Classical dimers on the triangular lattice”. *Phys. Rev. B*, Vol. 66, p. 214513, 2002. 18, 40

[Fish 61] M. E. Fisher. “Statistical Mechanics of Dimers on a Plane Lattice”. *Phys. Rev.*, Vol. 124, p. 1664, August 1961. 15

[Fowl 37] R. H. Fowler and G. S. Rushbrooke. “Statistical theory of perfect solutions”. *Trans. Faraday Soc.*, Vol. 33, p. 1272, 1937. 15

[Frad 03] E. Fradkin, D. A. Huse, R. Moessner, V. Oganesyan, and S. L. Sondhi. "Bipartite Rokhsar-Kivelson points and Cantor deconfinement". *Phys. Rev. B*, Vol. 69, p. 224415, 2003. 40

[Frad 90] E. Fradkin and S. Kivelson. "Short range resonating valence bond theories and superconductivity". *Mod. Phys. Lett. B*, Vol. 4, p. 225, 1990. 40, 60, 70

[Frad 91] E. Fradkin. *Field Theories Of Condenses Matter Systems*. *Frontiers In Physics*, Westview Press, 1991. 2, 60, 70

[Fuld 01] P. Fulde, A. N. Yaresko, A. A. Zvyagin, and Y. Grin. "On the origin of heavy quasiparticles in LiV_2O_4". *Europhys. Lett.*, Vol. 54, p. 779, 2001. 2

[Fuld 02] P. Fulde, K. Penc, and N. Shannon. "Fractional charges in pyrochlore lattices". *Ann. Phys.*, Vol. 11, p. 892, 2002. iii, v, 1, 9, 79

[Fuld 95] P. Fulde. *Electron correlations in molecules and solids*. Vol. 100, Springer Verlag, Berlin and Heidelberg, 3rd Ed., 1995. 88

[Gagl 87] E. R. Gagliano and C. A. Balseiro. "Dynamical Properties of Quantum Many-Body Systems at Zero Temperature". *Phys. Rev. Lett.*, Vol. 59, p. 2999, 1987. 47

[Girv 99] S. M. Girvin. "The Quantum Hall Effect: Novel Excitations and Broken Symmetries". *cond-mat/9907002*, 1999. 5

[Gold 95] V. Goldman and B. Su. "Resonant tunneling in the quantum Hall regime: measurement of fractional charge". *Science*, Vol. 267, p. 1010, 1995. 8

[Golu 96] G. H. Golub. *Matrix Computations*. Johns Hopkins University Press, Baltimore, Maryland, 1996. 87

[Hart 66] R. E. Hartwig. "Monomer Pair Correlations". *J. Math. Phys.*, Vol. 7, p. 286, 1966. 15

[Henl 04] C. L. Henley. "From classical to quantum dynamics at Rokhsar-Kivelson points". *J. Phys.: Condens. Matter*, Vol. 16, p. 891, 2004. 2

[Henl 97] C. L. Henley. "Relaxation time for a dimer covering with height representation". *J. Stat. Phys.*, Vol. 89, p. 483, 1997. 2, 40, 63, 65

[Herm 04] M. Hermele, M. P. A. Fisher, and L. Balents. "Pyrochlore photons: The $U(1)$ spin liquid in a $S = 1/2$ three-dimensional frustrated magnet". *Phys. Rev. B*, Vol. 69, p. 064404, 2004. 2, 9, 19, 40, 60, 71, 77

[Hofs 02] W. Hofstetter, J. I. Chirac, P. Zoller, E. Demler, and M. D. Lukin. "High-Temperature Superfluidity of Fermionic Atoms in Optical Lattices". *Phys. Rev. Lett.*, Vol. 89, p. 220407, 2002. 2

[Huse 03] D. A. Huse, W. Krauth, R. Moessner, and S. L. Sondhi. "Coulomb and Liquid Dimer Models in Three Dimensions". *Phys. Rev. Lett.*, Vol. 91, p. 167004, 2003. 19

[Isak 04] S. V. Isakov. "Dipolar Spin Correlations in Classical Pyrochlore Magnets". *Phys. Rev. Lett.*, Vol. 93, p. 167204, 2004. 17, 65

[Jack 75] R. Jackiw and C. Rebbi. "Solitons with fermion Number 1/2". *Phys. Rev. D*, Vol. 13, p. 3398, 1975. 6

[Kast 61] P. W. Kasteleyn. "The statistics of dimers on a lattice". *Physica*, Vol. 27, p. 1209, 1961. 15, 86

[Kita 03] A. Y. Kitaev. "Fault-tolerant quantum computation by anyons". *Ann. Phys.*, Vol. 303, p. 2, 2003. 40

[Kive 01] S. A. Kivelson. "Electron Fractionalization". *cond-mat/0106126*, 2001. 5

[Kogu 79] J. B. Kogut. "An introduction to lattice gauge theory and spin systems". *Rev. Mod. Phys.*, Vol. 51, p. 659, October 1979. 2

[Kond 96a] J. Kondev. "Liouville Field Theory of Fluctuating Loops". *Phys. Rev. Lett.*, Vol. 78, p. 4320, 1996. 15, 79, 85

[Kond 96b] J. Kondev and C. L. Henley. "Kac-Moody symmetries of critical ground states". *Nuc. Phys. B*, Vol. 464, p. 540, 1996. 63

[Kond 97] S. Kondo, D. C. Johnston, C. A. Swenson, F. Borsa, A. V. Mahajan, L. L. Miller, T. Gu, A. I. Goldman, M. B. Maple, D. A. Gajewski, E. J. Freeman, N. R. Dilley, R. P. Dickey, J. Merrin, K. Kojima, G. M. Luke, Y. J. Uemura, O. Chmaissem, and J. D. Jorgensen. "LiV_2O_4: A Heavy Fermion Transition Metal Oxide". *Phys. Rev. Lett.*, Vol. 78, p. 3729, May 1997. 2

[Kond 98] J. Kondev and J. L. Jacobsen. "Conformational Entropy of Compact Polymers". *Phys. Rev. Lett.*, Vol. 81, p. 2922, 1998. 15, 79, 85

[Krau 03] W. Krauth and R. Moessner. "Pocket Monte Carlo for classical doped dimer models". *Phys. Rev. B*, Vol. 67, p. 064503, 2003. 17

[Lauc 04] A. Läuchli and D. Poilblanc. "Spin-charge separation in two-dimensional frustrated quantum magnets". *Phys. Rev. Letters*, Vol. 92, p. 236404, 2004. 2, 9

[Laug 83] R. B. Laughlin. "Anomalous Quantum Hall Effect: An Incompressible Quantum Fluid with Fractionally Charged Excitations". *Phys. Rev. Lett.*, Vol. 50, p. 1395, 1983. 1, 5, 7

[Laug 99] R. Laughlin. "Fractional quantization". *Rev. Mod. Phys.*, Vol. 71, p. 863, 1999. 5

[Lieb 67] E. H. Lieb. “Exact Solution of the problem of the entropy of two-dimensional ice”. *Phys. Rev. Lett.*, Vol. 18, p. 692, 1967. 10

[Livo 03] M. Livon and X.-G. Wen. “Fermions, strings, and gauge fields in lattice spin models”. *Phys. Rev. B*, Vol. 67, p. 245316, 2003. 81

[Miel 91] A. Mielke. “Ferromagnetism in the Hubbard model on line graphs and further considerations”. *J. Phys. A*, Vol. 24, p. 3311, 1991. 23

[Misg 02] G. Misguich, D. Serban, and V. Pasquier. “Quantum Dimer Model on the Kagomé Lattice: Solvable Dimer-Liquid and Ising Gauge Theory”. *Phys. Rev. Lett.*, Vol. 89, p. 137202, 2002. 40

[Misg 03] G. Misguich and C. Lhuillier. “Two-dimensional quantum antiferromagnets”. *cond-mat/0310405*, October 2003. In [Diep 05], p 229ff. 2, 9

[Moes 01] R. Moessner and S. L. Sondhi. “Resonating Valence Bond Phase in the Triangular Lattice Quantum Dimer Model”. *Phys. Rev. Lett.*, Vol. 86, p. 1881, 2001. 18, 40

[Moes 02] R. Moessner, S. L. Sondhi, and E. Fradkin. “Short-ranged resonating valence bond physics, quantum dimer models, and Ising gauge theories”. *Phys. Rev. B*, Vol. 65, p. 024504, 2002. 40

[Moes 03a] R. Moessner and S. L. Sondhi. “Theory of the [111] magnetization plateau in spin ice”. *Phys. Rev. B*, Vol. 68, p. 064411, May 2003. 40, 42

[Moes 03b] R. Moessner and S. L. Sondhi. “Three-dimensional resonating-valence-bond liquids and their excitations”. *Phys. Rev. B*, Vol. 68, p. 184512, 2003. 40, 71, 77

[Moes 04] R. Moessner, O. Tchernyshyov, and S. L. Sondhi. “Planar Pyrochlore, Quantum Ice and Sliding Ice”. *J. Stat. Phys.*, Vol. 116, p. 755, 2004. 9, 17, 40, 42

[Naya 01] C. Nayak and K. Shtengel. “Microscopic models of two-dimensional magnets with fractionalized excitations”. *Phys. Rev. B*, Vol. 64, p. 64422, 2001. 40

[Nien 87] B. Nienhuis. *Phase transitions and Critical Phenomena*. Vol. 11, Academic, London, 1987. 19

[Penc 06] K. Penc and N. Shannon. “private communication and to be published”. 2006. 31, 75

[Pett 85] D. G. Pettifor and D. L. Weaire. *The Recursion Method and Its Applications*. Vol. 58 of *Springer Ser. Solid-State Science*, Springer, Berlin, Heidelberg, 1985. 88

[Picc 97] R. de Picciotto, M. Reznikov, M. Heiblum, V. Umansky, G. Bunin, and D. Mahalu. "Direct observation of a fractional charge". *Nature*, Vol. 389, p. 162, 1997. 8

[Poll 06a] F. Pollmann, J. Betouras, K. Shtengel, and P. Fulde. "Correlated fermions on a checkerboard lattice". Vol. 97, p. 170407, 2006. 3

[Poll 06b] F. Pollmann, J. J. Betouras, and E. Runge. "Classical correlations of defects in lattices with geometrical frustration in the motion of a particle". *Phys. Rev. B*, Vol. 73, p. 174417, 2006. 3

[Poll 06c] F. Pollmann, J. J. Betouras, E. Runge, and P. Fulde. "Charge degrees in the quarter-filled checkerboad lattice". *Proceedings of ICM2006 (in print)*, 2006. 3

[Poll 06d] F. Pollmann and P. Fulde. "On confined fractional charges: a simple model". *Europhys. Lett.*, Vol. 75, p. 133138, 2006. 3

[Poll 06e] F. Pollmann, E. Runge, and P. Fulde. "Spectral functions and optical conductivity of spinless fermions on a checkerboard lattice". *Phys. Rev. B*, Vol. 73, p. 125121, 2006. 3

[Poly 77] A. M. Polyakov. "Quark confinement and topology of gauge theories". *Nucl. Phys. B*, Vol. 120, p. 429, 1977. 2, 63, 81

[Rokh 88] D. S. Rokhsar and A. A. Kivelson. "Superconductivity and the Quantum Hard-Core Dimer Gas". *Phys. Rev. Lett.*, Vol. 61, p. 2376, 1988. iv, v, 2, 14, 29, 32, 40, 41, 42, 74, 80

[Rung 04] E. Runge and P. Fulde. "Charge degrees of freedom in frustrated lattice structures". *Phys. Rev. B*, Vol. 70, p. 245113, 2004. iii, v, 21, 23, 27, 38, 80

[Shan 04] N. Shannon, G. Misguich, and K. Penc. "Cyclic exchange, isolated states and spinon deconfinement in an XXZ Heisenberg model on the checkerboard lattice". *Phys. Rev. B*, Vol. 69, p. 220403(R), 2004. 2, 9, 40, 42, 80

[Silv 94] R. N. Silver and H. Roeder. "Densities of states of mega-dimensional Hamiltonian matrices". *Int. J. Mod. Phys.*, Vol. 5, p. 735, 1994. 91

[Silv 96] R. N. Silver, H. Roeder, A. F. Voter, and J. D. Kress. "Kernel Polynomial Appoximation for Densities of States and Spectral Functions". *J. Comp. Phys.*, Vol. 124, p. 115, 1996. 47, 91

[Silv 97] R. N. Silver and H. Roeder. "Calculation of densities of states and spectral functions by Chebyshev recursion and maximum entropy". *Phys. Rev. E*, Vol. 56, p. 4822, 1997. 91

[Su 79] W. P. Su, J. R. Schrieffer, and A. J. Heeger. "Solitons in Polyacetylene". *Phys. Rev. Lett.*, Vol. 42, p. 1698, 1979. 1, 5

[Su 81] W. P. Su and J. R. Schrieffer. “Fractionally Charged Excitations in Charge-Density-Wave Systems with Commensurability 3”. *Phys. Rev. Lett.*, Vol. 46, p. 738, March 1981. 1, 6

[Sylj 02] O. F. Syljuasen and A. W. Sandvik. “Quantum Monte Carlo with directed loops”. *Phys. Rev. E*, Vol. 66, p. 046701, 2002. 16, 42

[Tsui 82] D. C. Tsui, H. L. Stormer, and A. C. Gossard. “Two-Dimensional Magnetotransport in the Extreme Quantum Limit”. *Phys. Rev. Lett.*, Vol. 48, p. 1559, 1982. 5, 7

[Weis 04] A. Weisse. “Chebyshev expansion approach to the AC conductivity of the Anderson model”. *Euro. Phys. J. B*, Vol. 40, p. 125, 2004. 91

[Wilc 02] F. Wilczek. “Some Basic Aspects of Fractional Quantum Numbers”. *cond-mat/020612*, 2002. In [Bark 98]. 5

[Yana 78] A. Yanagawa and J. F. Nagle. “Calculations of correlation functions for two-dimensional square ice”. *Chem. Phys.*, Vol. 43, p. 329, 1978. 16

[Zhit 03] M. E. Zhitomirsky. “Enhanced magnetocaloric effect in frustrated magnets”. *Phys. Rev. B*, Vol. 67, p. 104421, 2003. 10